SEISMOGENIC ZONES AND ATTENUATION LAWS FOR PROBABILISTIC SEISMIC HAZARD ASSESSMENT IN LOW DEFORMATION AREA

ZONAS SISMOGÉNICAS E LEIS DE ATENUAÇÃO PARA A ANÁLISE PROBABILÍSTICA DA PERIGOSIDADE SÍSMICA EM REGIÕES DE BAIXA DEFORMAÇÃO

Boris LE GOFF

Tese apresentada à Universidade de Évora
para obtenção do Grau de Doutor em Ciências da Terra e do Espaço
Especialidade: Geofísica

ORIENTADORES: *Mourad BEZZEGHOUD*
José Fernando BORGES

ÉVORA, DEZEMBRO 2013

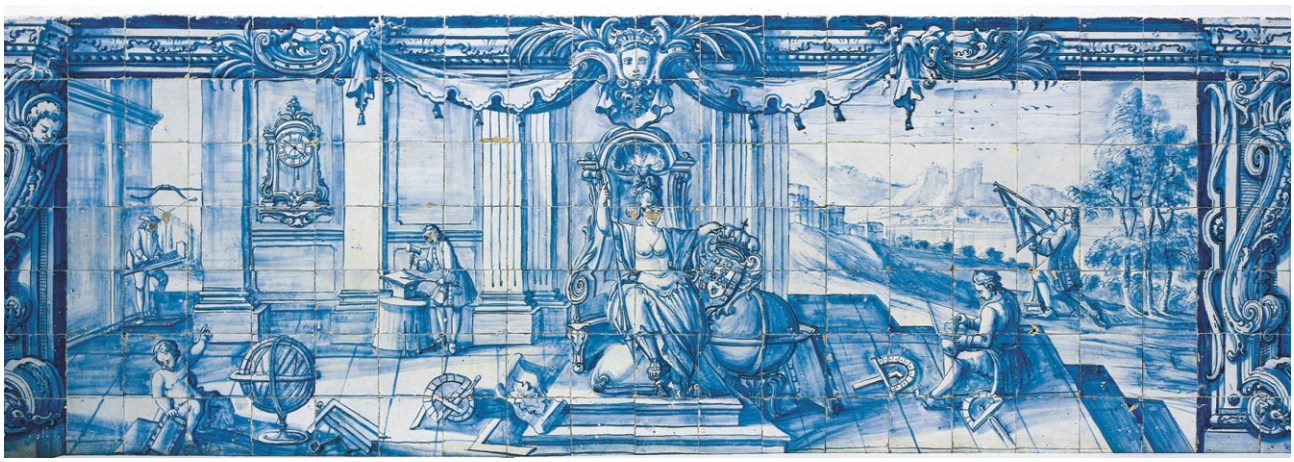

INSTITUTO DE INVESTIGAÇÃO E FORMAÇÃO AVANÇADA

SEISMIC SOURCES AND ATTENUATION LAW FOR PSHA IN LOW DEFORMATION AREA

Boris LE GOFF

Tese de doutoramento
na Universidade de Évora, Évora

submetida por
Boris Le Goff

Évora, 4 de Dezembro 2013

Orientador: Mourad Bezzeghoud
Co-orientador: José Fernando Borges

Contents

Seismogenic zones and attenuation laws for Probabilistic Seismic Hazard Assessment in low deformation area

Abstract

The objective of this thesis is to introduce reproducible methodologies into the Probabilistic Seismic Hazard Analysis (PSHA), rather than the subjective methodologies that are currently used. This study focuses particularly in the definition of the seismic sources, through the seismotectonic zoning, and the determination of historical earthquake location.

An important step in the Probabilistic Seismic Hazard Analysis consists in defining the seismic source model. Such a model expresses the association of the seismicity characteristics with the tectonically-active geological structures evidenced by seismotectonic studies. Given that most of the faults, in low seismic regions, are not characterized well enough, the source models are generally defined as areal zones, delimited with finite boundary polygons, within which the seismicity and the geological features are deemed homogeneous (e.g., focal depth, seismicity rate). Besides the lack of data (short period of instrumental seismicity), such a method generates different problems for regions with low seismic activity: 1) a large sensitivity of resulting hazard maps to the location of zone boundaries, while these boundaries are set by expert decisions; 2) the zoning cannot represent any variability or structural complexity in seismic parameters; 3) the seismicity rate is distributed throughout the zone and the location of the determinant information used for its calculation is lost.
We investigate an alternative approach to model the seismotectonic zoning, with three main objectives: 1) obtaining a reproducible method that 2) preserves the information on the sources and extent of the uncertainties, so as to allow to propagate them (through Ground Motion Prediction Equations on to the hazard maps), and that 3) redefines the seismic source concept to debrief our knowledge on the seismogenic structures and the clustering.
To do so, the Bayesian methods are favored. First, a generative model with two zones, differentiated by two different surface activity rates, was developed, creating synthetic catalogs drawn from a Poisson distribution as occurrence model, a truncated Gutenberg-Richter law as magnitude-frequency relationship and a uniform spatial distribution. The inference of this model permits to assess the minimum number of data, n_{min}, required in an earthquake catalog to recover the activity rates of both zones and the limit between them, with some level of accuracy.

In this Bayesian model, the earthquake locations are essential. Consequently, these data have to be obtained with the best accuracy possible. The main difficulty is to reduce the location uncertainty of historical earthquakes. We propose to use the method of Bakun and Wentworth (1997) to re-estimate the epicentral region of these events. This method uses directly the intensity data points rather than the isoseismal lines, set up by experts. The significant advantage in directly using individual intensity observations is that the procedures are explicit and hence the results are reproducible. The results of such a method provide an estimation of the epicentral region with levels of confidence appropriated for the number of intensity data points used.

As example, we applied this methodology to the 1909 Benavente event, because of its controversial location and the particularly shape of its isoseismal lines. A new location of the 1909 Benavente event is presented in this study and the epicentral region of this event is expressed with confidence levels related to the number of intensity data points. This epicentral region is improved by the development of a new intensity-distance attenuation law, appropriate for the Portugal mainland. This law is the first one in Portugal mainland developed as a function of the magnitude (M) rather than the subjective epicentral intensity (Muñoz, 1974, Martin 1984; Lopez Casado et al. 1992; Sousa and Oliveira, 1997; Lopez Casado et al., 2000).
From the logarithmic regression of each event, we define the equation form of the attenuation law. We obtained the following attenuation law:

$$I = -1.9438\ \ln(D) + 4.1\,Mw - 9.5763 \quad \text{for } 4.4 \leq \text{Mw} \leq 6.2$$

Using these attenuation laws, we reached to a magnitude estimation of the 1909 Benavente event that is in good agreement with the instrumental one. The epicentral region estimation was also improved with a tightening of the confidence level contours and a minimum of rms[M_I] coming closer to the epicenter estimation of Kárník (1969).

Finally, this two zone model will be a reference in the comparison with other models, which will incorporate other available data. Nevertheless, future improvements are needed to obtain a seismotectonic zoning.
We emphasize that such an approach is reproducible once priors and data sets are chosen. Indeed, the objective is to incorporate expert opinions as priors, and avoid using expert decisions. Instead, the products will be directly the result of the inference, when only one model is considered, or the result of a combination of models in the Bayesian sense.

Zonas sismogénicas e leis de atenuação para a análise probabilística da perigosidade sísmica em regiões de baixa deformação

Resumo

O objetivo desta tese é de apresentar metodologias reprodutíveis na estimação probabilística da perigosidade símica (PSHA), em vez das metodologias subjetivas que são usadas atualmente. Este estudo concentra-se particularmente na definição das fontes sísmicas, através do zonamento sismotectónico, e a localização de sismos históricos.

Uma etapa importante na estimação do PSHA é a de definir o modelo de fonte sísmica. Este modelo reflete a associação das características de sismicidade com as estruturas tectónicas ativas, evidenciada pelos estudos sismotectónicos. Dado que a maioria das falhas em regiões de baixa sismicidade não estão suficientemente bem caracterizadas, os modelos de fonte são geralmente definidos como zonas de fonte polígonais delineadas por limites finitos, dentro dos quais a actividade sísmica e as características geológicas são consideradas homogéneas (por exemplo, a profundidade focal e a taxa de sismicidade). Para além da falta de dados (curto período de sismicidade instrumental), este método cria diferentes problemas para as zonas de baixa sismicidade: 1) uma elevada sensibilidade dos mapas de perigosidade nos limites das áreas, sendo que estes limites são feitos por decisão de peritos; 2) o zonamento não representa a variabilidade ou a complexidade estrutural dos parâmetros sísmicos; 3) a taxa de atividade sísmica é distribuída para toda a área e perde-se a localização da informação crítica utilizada para o seu cálculo .

Propomos um método alternativo para o modelo de zonamento sismotectónico, com três objetivos principais: 1) obter um método reprodutível que 2) preserve as fontes de informação e incerteza, de maneira a propagá-los (através das equações de predição do movimento do solo e dos mapas de perigosidade) e que 3) redefine o conceito de fonte sísmica para questionar o nosso conhecimento acerca das estruturas sismogénicas.

Neste sentido, os métodos Bayesianos são previlegiados. Foi desenvolvido um modelo generativo com duas zonas, diferenciadas por duas taxas de atividade sísmica, criando catálogos sintéticos derivados de uma distribuição de Poisson (modelo de ocorrência), de uma lei de Gutenberg-Richter truncada (relação magnitude-frequência) e de uma distribuição espacial uniforme de epicentros. A inferência deste modelo permite-nos estimar o número mínimo de dados, n_{min}, exigido num catálogo de sismicidade para estimar com um certo nível de precisão a taxa de atividade sísmica de cada zona e a respectiva fronteira.

Neste modelo Bayesiano a localização dos sismos é crucial. É, por isso, fundamental obter estes

dados com a maior precisão possível. A principal dificuldade reside na redução da incerteza na localização dos sismos históricos. Propomos a utilização do método de Bakun e Wentworth (1997) para re-estimar a região epicentral destes eventos. Este método usa diretamente dados pontuais da intensidade em vez das isossistas desenhadas por peritos. A vantagem significativa da utilização directa dos dados pontuais de intensidade é a clareza do processo e a reprodutibilidade dos resultados. Os resultados deste método produzem uma estimativa do epicentro associado a níveis de confiança apropriadas para o número de dados utilizados.
Como exemplo, aplicámos esta metodologia ao terramoto de Benavente (1909) devido à sua controversa localização e à forma particular das suas isossistas. Deste estudo resultou uma nova localização do sismo de Benavente em que o epicentro deste evento é expresso com níveis de confiança que estão relacionados com o número de dados de intensidade. A localização epicentral foi melhorado pelo desenvolvimento de uma nova lei de atenuação, adequado para Portugal continental. Esta lei é a primeira desenvolvida em termos de magnitude, em vez da subjetiva intensidade epicentral proposta por outros autores (Muñoz, 1974, Martin 1984; Lopez Casado et al. 1992; Sousa and Oliveira, 1997; Lopez Casado et al., 2000).
A partir da regressão logarítmica de cada evento, obtivemos a lei de atenuação seguinte:

$$I = -1.9438\ \ln(D) + 4.1\,Mw - 9.5763 \quad \text{para } 4.4 \leq \text{Mw} \leq 6.2$$

Usando estas leis de atenuação, chegamos a uma estimativa da magnitude do sismo ocorrido em Benavente em 1909, que é semelhante à que foi obtida por via instrumental (Mw = 6.0). A estimativa da zona epicentral foi também melhorada com um aperto dos contornos de nível de confiança e um mínimo de rms [M_I] que aproximando-se da estimativa epicentral obtida por Karnik (1969) à partir de dados instrumentais.

Finalmente, este modelo de duas zonas será uma referência na comparação com outros modelos, que irão incorporar outros dados disponíveis no sentido de obter um melhor zonamento sismotectónico.
Insistimos que esta abordagem é reprodutível, a partir do momento que a informação *a priori* e os dados são selecionados. Com efeito, foi feito um esforço para incorporar as opiniões de peritos como informação *a priori*, evitando, deste modo, o uso de decisões dos mesmos. Os resultados finais são directamente uma consequência de uma inferência, quer quando se considera um único modelo, quer quando se considera uma combinação dos modelos no sentido Bayesiano.

Zones sismogéniques et lois d'atténuation pour l'évaluation de l'aléa sismique probabiliste dans les régions à déformation lente

Résumé

L'objectif de cette thèse est d'introduire des méthodologies reproductibles dans le calcul d'aléa sismique probabiliste (PSHA), plutôt que les méthodologies subjectives qui sont actuellement utilisées. Cette étude se concentre particulièrement sur la définition des sources sismiques, à travers le zonage sismotectonique, et la détermination de la localisation des séismes historiques.

Une étape importante de l'estimation probabiliste du l'aléa sismique (PSHA) consiste à définir le modèle de source sismique. Un tel modèle reflète l'association des caractéristiques de sismicité avec les structures de tectonique active, mise en évidence par les études sismotectoniques. Étant donné que la plupart des failles, dans les régions peu sismiques, ne sont pas assez bien caractérisées, les modèles de source sont généralement définies comme des zones-sources, délimitées avec des polygones à limites finies, à l'intérieur desquels la sismicité et les caractéristiques géologiques sont considérées homogènes (ex: profondeur focale, taux de sismicité). En plus du manque de données (courte période de sismicité instrumentale), une telle méthode génère différents problèmes pour des régions à faible sismicité: 1) une grande sensitivité des cartes d'aléa au niveau des limites de zones, alors que ces limites sont réalisés par des décisions d'experts; 2) le zonage ne permet pas de représenter la variabilité ou la complexité structurelle dans les paramètres sismiques; 3) le taux de sismicité est distribué à travers la zone et on perd la localisation de l'information déterminante qui a été utilisé pour son calcul.
Nous proposons une méthode alternative pour modéliser le zonage sismotectonique, avec trois principaux objectifs: 1) obtenir une méthode reproductible qui 2) préserve l'information sur les sources et ses incertitudes, de façon à les propager (à travers les équations de prédiction du mouvement du sol, puis dans les cartes d'aléa) et qui 3) redéfini le concept de source sismique pour questionner nos connaissances sur les structures sismogènes.
Dans ce but, les méthodes bayésiennes sont privilégiées. Un modèle génératif avec deux zones, différenciées par deux taux d'activité sismique surfacique différents, a été développé, créant des catalogues synthétiques tirés d'une distribution de Poisson comme modèle d'occurrence, d'une loi de Gutenberg-Richter tronquée comme relation magnitude-fréquence et une distribution spatiale uniforme. L'inférence de ce modèle nous permet d'estimer le nombre minimum de données, n_{min}, requis dans un catalogue de sismicité pour retrouver le taux d'activité de chacune des zones et la limite entre elles, avec un certain niveau de précision.

Dans ce modèle bayésien, la localisation des séismes est primordiale. Par conséquent, nous devons obtenir ces données avec la meilleure précision possible. La difficulté principale réside dans la

réduction de l'incertitude liée à la localisation des séismes historiques. Nous proposons d'utiliser la méthode de Bakun and Wentworth (1997) pour ré-estimer la région épicentrale de ces évènements. Cette méthode utilise directement les points de données d'intensité plutôt que les isoséismes, réalisés par des experts. L'avantage significatif de l'utilisation directe des points de données d'intensité est que la démarche est explicite et que les résultats sont reproductibles. Les résultats d'une telle méthode donnent une estimation de la région épicentrale avec des niveaux de confiance qui sont appropriés pour le nombre de points d'intensité utilisés.
Comme exemple, nous avons appliqué cette méthodologie au séisme de Benavente (1909), en raison de sa localisation controversée et de la forme particulière de ses isoséimes. Une nouvelle localisation du séisme de Benavente a été présentée dans cette étude. La région épicentrale de cette évènement est exprimée avec des niveaux de confiance qui sont reliés au nombre de points de données d'intensité. Cette région épicentrale a été améliorée par le développement d'une nouvelle loi d'atténution, appropriée pour le Portugal continental. Cette loi est la première développée en fonction de la magnitude plutôt qu'en fonction de l'intensité épicentrale (Muñoz, 1974, Martin 1984; Lopez Casado et al. 1992; Sousa and Oliveira, 1997; Lopez Casado et al., 2000).
À partir de la régression logarithmique de chaque évènement, nous avons obtenu la loi d'atténuation suivante:

$$I = -1.9438\ \ln(D) + 4.1\,Mw - 9.5763 \quad \text{pour } 4.4 \leq \text{M w} \leq 6.2$$

En utilisant ces lois d'atténuation, nous atteignons une estimation de magnitude pour le séisme de Benavente (1909) qui est en accord avec la magnitude instrumentale. L'estimation de la région épicentrale a aussi été amélioré, avec un resserrement des contours de niveau de confiance et un minimum de rms[M_I] se rapprochant de l'estimation d'épicentre de Kárník (1969).

Finallement, ce modèle deux zones sera une référence dans la comparaison avec d'autres modèles, qui incorporerons d'autres données disponibles. Cependant, des améliorations futures sont nécessaires pour obtenir un zonage sismotectonique.
Nous insistons sur le fait qu'une telle approche est reproductible, à partir du moment où les informations *a priori* et les données sont choisis. En effet, nous nous efforcerons d'incorporer les opinions d'experts comme information *a priori*, en évitant d'utiliser les décisions d'experts. Les résultats finaux seront directement le résultat de l'inférence, quand un seul modèle est considéré, ou le résultat d'une combinaison de modèles, au sens bayésien.

List of figures

List of tables

CHAPTER *1*

Introduction

The Portugal mainland presents a moderate seismicity, where destructive earthquakes are rare but not impossible. Some large destructive earthquakes occurred in the last four centuries. Among them, the 1755 Lisbon earthquake was one of the most destructive, causing more than several thousand deaths, due to the combined effect of the earthquake itself, the generated fire and the propagation of a tsunami. The estimation of the seismic risk is, therefore, imperative. Seismic risk is determined by the combination of vulnerability, exposure and hazard.
The consequences of an earthquake also depend on the resistance of buildings to the effects of a seismic tremor. A building's potential for damage is called vulnerability. The more vulnerable a building is (due to its type, inadequate design, poor quality materials and construction methods, lack of maintenance), the greater the consequences will be. One of the main causes of death during an earthquake is building collapse. To reduce the loss of human lives, buildings must be made safe. Laws governing construction in seismic zones today state that buildings must not be damaged by low-intensity earthquakes, must not be structurally damaged by medium-intensity earthquakes and must not collapse in the event of severe earthquakes despite suffering serious damage.
The number of assets exposed to risk, the possibility in other words of damage in economic terms or the loss of human lives, is called exposure. It can generally be estimated, with a certain margin for error and especially for more severe earthquakes, how many people were involved, using calculations based on the number of collapsed or damaged buildings. Several considerations are needed to be able to make these estimates as the number of people living in the buildings, the time of the earthquake, the possibilities of escape and/or protection, how people were affected (dead or injured) and the possibility of dying even after aid has been given.
Finally, estimating the seismic hazard in a site, consists in determining the ground motion against which we have to protect. Hazard studies can be used for urban planing but also in site analysis, to locate critical buildings from a point of view of safety, risk or strategic importance (power stations, military installations, hospitals). Hazard assessment in this case means calculating the probability of an earthquake of a magnitude (or PGA) that exceeds the threshold value established by political/decisional bodies, leading to the choice of different areas if necessary. Hazard assessment may be deterministic or probabilistic. This thesis focuses only on the Probabilistic Seismic Hazard Assessment (PSHA).

The Probabilistic Seismic Hazard Assessment was created in the late 60's in the United-States. Cornell (1968) proposes to calculate annual rates of exceedance of ground motion levels and to introduce them into a temporal process of poissonian occurrence: the probabilistic seismic hazard is a ground motion level which has a certain probability to be exceeded in a given time period. This calculation requires a zoning of the study area into seismic source zones, a description of the seismicity of the source zones and a model of ground motion attenuation. In 1976, the United State of Geological Survey (USGS) published the first maps of seismic hazard for the USA (Algermissen and Perkins, 1976). The same year, McGuire (1976) introduced the dispersion of the seismic motion into the calculations. Then, these probabilistic methods were used to estimate the seismic hazard of the nuclear power plans (EPRI, 1986, Bernreuter et al., 1989). Currently, the modifications of this method concern essentially the models of the source zones and the earthquake recurrences (Zöller 2007, Kuehn 2008, Fitzenz et al. 2010).

The estimation of the seismic hazard is indivisible of the notion of uncertainty. In each step of the seismic hazard assessment, choices have to be done. The uncertainties are related to the database but also to the choice of the models and their parameterization. So far, these uncertainties are considered in PSHA through logic trees.

Several studies have shown the determinant impact of seismotectonic zoning in PSHA (Bender, 1986; Woo, 1996; Beauval, 2003; Beauval and Scotti, 2004; Le Goff et al., 2009). The

seismotectonic zoning allows linking the seismicity with the tectonically-active geological structures, in order to define the seismic sources. Usually, and because faults are often not characterized well-enough, source zones are defined as surfaces and modeled as polygons. In that case, they are delimited with fixed, infinitely thin boundaries. In each zone, the geological expression of active tectonics and the seismicity are deemed homogeneous (e.g., focal depths and mechanisms, seismicity rate, and maximum magnitude), and each point of a zone is considered an equally likely source of earthquake.

Besides the lack of data (e.g., short period of instrumental observation of small events, short catalog of large events, blind faults), the establishment of a traditional seismotectonic zoning generates different shortcomings. The finite boundaries of the different zones are set by expert decisions, leading to different problems: 1) the superposition of a resulting hazard map with areal source zoning model underlines the large sensitivity of the results to this method (Beauval, 2003); 2) the seismotectonic zoning is not reproducible: different experts come up with different zonings using the same input data; 3) the final seismotectonic zoning is not provided with error maps reflecting the original density of information used for both the assessment of the common characteristics and the calculation of seismicity rates of each zone and 4) the zoning does not account for any variation in faulting mechanisms with depth or for conjugate sets of faults.
Some approaches, such as statistical region partitioning (Weatherhill and Burton, 2009) or the smoothing at the source zone boundaries (Bender 1986), strive to resolve these shortcomings but are still not satisfying.

This PhD thesis is an exploratory study for alternative procedures in area source modeling that aims to obtain a method which will be robust and reproducible. In this way, we strive to combine different data using Bayesian methods.
We developed a generative model with two zones, characterized by two different surface activity rates, creating synthetic catalogs drawn from a Poisson distribution as occurrence model, a truncated Gutenberg-Richter law as magnitude-frequency relationship and a uniform spatial distribution. We proposed a Bayesian model to recover the limit between these two zones with levels of confidence.

In our model, the earthquake locations are essential as they are directly implied in the estimation of the limit between the two zones but also to the definition of the seismicity parameters of each zone (e.g., seismicity activity rates, parameters of the magnitude-frequency relationship, definition of the Maximum Credible Earthquake that represents the largest magnitude expected into the zone). These data need therefore to be obtained with the best accuracy possible. First, we need to differentiate the data provided by the instrumental catalogs and the data provided by the historical catalogs. In the first case, the uncertainty on earthquake location is related to the occurrence date of the event. The improvement of calculation methods, the development of the seismic network and the improvement of the velocity models allowed obtaining more accurate instrumental location. Nevertheless, this uncertainty can be reduced using the method of the double-difference (Waldhauser and L.Ellsworth, 2000). The location uncertainty of the historical earthquakes is related to the number of intensity data points available and the method used to achieve this location. In most cases, the estimation of an historical earthquake location is done using isoseismal lines delimited by experts, introducing a subjective part. In order to prevent such subjectivity, here we favoured the method of Bakun and Wentworth (1997) that allows estimating the epicentral region and the moment magnitude of an historical earthquake, directly from its intensity data points. The results of such a method provide an estimation of the epicentral region with levels of confidence appropriated for the number of intensity data points used.

We chose to apply this methodology to the 1909 Benavente event (moment magnitude, M_w=6.0) because it is one of the most documented (Bensaude, 1910; Teves-Costa and Batlló, 2010). This event is also the only one, in Portugal mainland, that has intensity data points with small epicentral distances. The other reason to investigate this event is its controversial location, estimated from its isoseismal lines that present particular shapes (Mezcua, 1982; Senos et al., 1994; Teves-Costa and Batlló, 2010). First, the methodology of Bakun and Wentworth (1997) will be applied using the attenuation law of Atkinston and Boore (1997), that was already used in the calculation of the PSHA in Portugal (Vilanova and Fonseca, 2007). However, the use of this attenuation law may not be appropriated for our study area, because of the difference of seismotectonic context or seismicity. We developed a new intensity-distance attenuation law for the Portugal mainland, using the macroseismic reports of events that provide intensity data points and instrumental magnitudes. This law is directly derived from the intensity data points and expressed as a function of magnitude and epicentral distances.

The attenuation law may also be called Ground Motion Prediction equations (GMPEs). Both terms refer to a mathematical equation or engineering model that relates a strong-motion parameter to one or more parameters of the earthquake source, wave propagation path, and local site condition. In this study, and to avoid confusions, the term "attenuation law" will be used to talk about the mathematical equation that links the macroseismic intensity to the magnitude and the epicentral distance. The term "GMPE" will be used to represent the mathematical equation that links a ground-motion parameter (Peak Ground Acceleration, Peak Ground Velocity or Peak Ground Displacement) to the magnitude and the distances. In this study, the "GMPEs" are considered directly linked with a use into the PSHA.

The chapter 2 of this thesis presents the different steps of PSHA approach: the definition of the seismic sources, the determination of the magnitude-frequency distribution, the definition of the temporal probabilistic models, the definition of the Ground Motion Prediction Equations (GMPEs), the assessment of the uncertainties and the representation of the seismic hazard. The chapter 3 describes the geodynamic and seismotectonic context of the Portugal mainland, its seismicity and its focal mechanisms. The chapter 4 explains the Bayesian methodology and its use in our seismotectonic zoning model. The chapter 5 presents the Bakun and Wentworth methodology and its use to relocate historical earthquakes (example of the 1909 Benavente event). This chapter also explains the development of a new intensity-distance attenuation law, that improves the relocation and the magnitude estimation of the 1909 Benavente event.

CHAPTER 2

Probabilistic Seismic Hazard Analysis

2.1. Introduction

Different approaches exist to assess the seismic hazard. The deterministic approach (DSHA) is done for a particular earthquake, either assumed or realistic. The DSHA approach uses the known seismic sources sufficiently near the site and the available historical seismic and geological data to generate discrete, single-valued events or models of ground motion at the site. Typically one or more earthquakes are specified by magnitude and location with respect to the site. The site ground motions are estimated deterministically, given the magnitude, source-to-site distance, and site condition. The Probabilistic seismic hazard analysis (PSHA) is the most widely used approach for the determination of seismic design loads for engineering structures. The use of probabilistic concept has allowed uncertainties in size, location, and rate of recurrence of earthquakes and in the variation of ground motion characteristics with earthquake size and location to be explicitly considered for the evaluation of seismic hazard. In addition, PSHA provides a frame work in which these uncertainties can be identified, quantified and combined in a rational manner to provide a more complete picture of the seismic hazard.
This chapter focuses exclusively on the PSHA approach.

The PSHA consists in calculating the annual rate of occurrence of a ground-motion parameter exceeding a target level of acceleration at a site. Usually, this target level is described by the Peak Ground Acceleration (PGA). It is common to refer to the return periods (inverse of the annual rate) instead of the annual rates. According to application domain these return periods are ranged from 100 to 10^7 years. There is several approaches to assess the probabilistic seismic hazard and the most used is the Cornell-McGuire approach (Cornell, 1968; McGuire, 1976).

The PSHA is composed by eight successive steps:

1) The achievement of a zoning, based on the seismotectonic analysis of the study area. This analysis aims to highlight the links between the seismicity and the active geological structures. This zoning is, then, composed by seismotectonic units that are deemed geologically and geophysically homogeneous.

2) The constitution of a uniform and complete seismicity catalog. Indeed, seismicity data are provided by different sources and may present different kind of magnitude or different intensity scales. The seismicity catalogs also aim to be exhaustive in all the observation period.

3) The digitizing of the seismotectonic zoning into geometrical source zones, which would be directly introduced into the PSHA computation.

4) The characterization of the seismic activity of the different source zones, usually computed through the Gutenberg-Richter distribution, which gives the number of earthquakes as a function of the magnitude. This law shall represent the seismicity of each source zone by incorporating the whole available historical and instrumental seismicity data.

5) The choice of the probabilistic distribution model of future earthquakes. Even if the use of the Poisson model is controversial, it is the most widely used into the PSHA calculations, meaning an earthquake occurrence time independent and a stationary seismic activity. Other models, incorporating an “earthquake history memory”, are developed and tend to be preferentially used into the more recent PSHA calculations.

6) The quantification, in a target study site, of the induced effects of the different source zones,

through ground motion parameters (displacement, velocity, acceleration), or of the intensity. This effects are calculated from the Ground Motion Prediction Equations (GMPEs), adapted to the regional seismotectonic context, which depend on the epicentral or hypocentral distance and on the magnitude.

7) The computation of the seismic hazard itself. The different parameters are provided to PSHA code (EQRISK developed by McGuire, 1976; CRISIS developed by Ordaz et al., 2003).

8) The graphical representation of the obtained results. Usually these results are represented through hazard maps, hazard curves or uniform hazard spectra.

The whole steps are resumed in figure 2.1 and will be described in details in the following chapters.

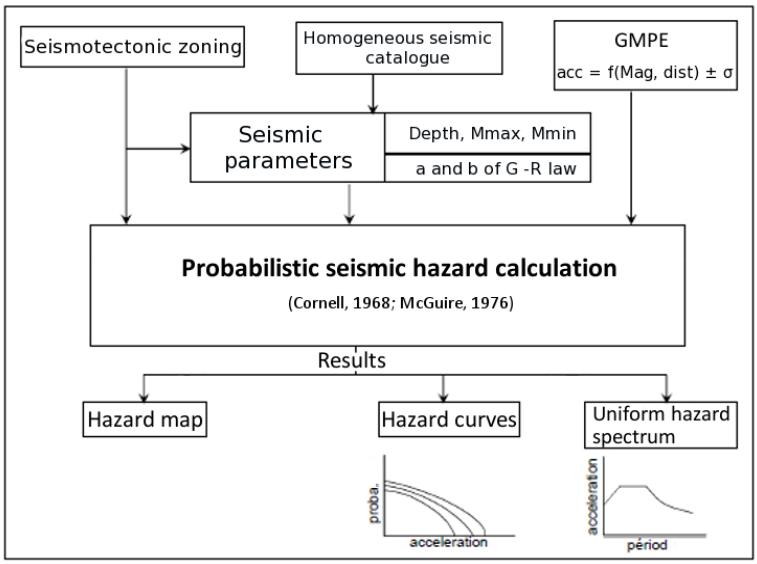

Figure 2.1: Main steps of PSHA. a and b represent the parameters of the Gutenberg-Richter law (G-R law). Mmax is the maximum magnitude expected into the zone source. The Ground Motion Prediction Equation (GMPE) is described by the acceleration (acc) that is function of the magnitude (Mag), the distance (dist) and expressed with the standard deviation (σ).

2.2. Earthquake location: definition of the seismic sources

2.2.1. Conception and geometry of the seismic sources

2.2.1.1. Source zone concept

PSHA studies require a zoning. Usually, a seismotectonic zoning is achieved, including different seismotectonic units: seismotectonic domains, seismogenic structure systems or seismogenic systems. This seismotectonic analysis uses the structural data, the neotectonical data and the seismological data, in order to establish the links between the seismic activity and the recent deformation mechanisms. This seismotectonic zoning needs to be modified into geometric source zones for their computational treatment.
In regions of low to moderate seismicity, where the seismotectonic data are poor, source zones are set up according to the single parameter of seismicity.

2.2.1.2. The different kinds of seismic sources

The concept of seismic sources, to represent the seismicity in a probabilistic way, was introduced by Cornell (1969). Three kinds of sources were differentiated: the point sources, the line sources (or fault sources) and zone sources (figure 2.2).

The point sources are used when the potential earthquake source is geographically concentrated relating to the epicentral distance to the site. Source zones are defined by seismotectonic criteria, whether it be for seismogenic structure systems, that are seismically active, or for seismotectonic domains with low and sparse seismicity. Source faults are linked to high seismicity concentrated on fault lines. Usually, they are used when active faults are well known. It is important to notice that the seismic hazard may be highly underestimated, due to the existence of blind faults (unknown part of seismic faults), that may lead to important disasters (e.g., the 1995 Mw=6.9 Kobe earthquake, Japan).

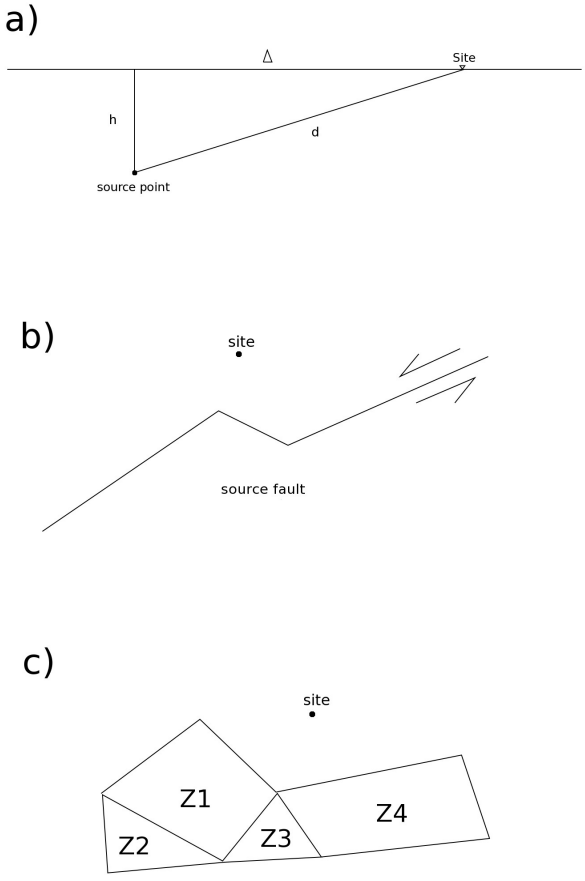

Figure 2.2: Different kinds of seismic sources. a) point source, b) source fault and c) source zone

Most of these seismic source models suppose a uniform surface seismicity repartition, meaning that the seismicity rate is constant per surface unit. This assumption may be questionable. Musson (2004) compares the spatial repartition of events from a synthetic catalog, using a uniform distribution, and from the real seismicity catalog. The results show a significant difference between the random spatial distribution of the synthetic catalog and the clustered real seismicity.

2.3. Earthquake size and frequency: determination of the magnitude distribution law

2.3.1 Magnitude and Epicentral intensity

The probabilistic approach needs a complete seismicity catalog that is composed by several seismicity catalogs having different kind of data and that is exhaustive and homogeneous. We differentiate the historical seismicity catalogs providing data until 1000 years ago, to the instrumental catalogs including data since the early XX^{th} century with a large development from the 60's on.
The collect of earthquake information (effects on the population and observed damages on structures or on the environment) allowed qualifying the observed effects in the earth surface. The discrete scale of intensity has been establish to give a value to the testimonies, historical writings, etc. It is the only available information to consider these ancient earthquakes, prior to the first seismometers.
The notion of magnitude to quantify the released energy of earthquakes, from instrumental records, only appeared around 1935. This physical size is now admitted as a reference to express the released energy and the size of a seismic source.
According to the large return period of largest earthquakes (about 10 000 years), it is important to consider all available information, including the sparse and heterogeneous intensity data.

2.3.2. Conversions

Most of the hazard analysis results are expressed with a ground motion parameter: displacement, velocity or acceleration. These parameters present a particularly interest for the civil engineer, because of their frequency contains (response spectra). These parameters are calculated with the Ground Motion Prediction Equations (GMPEs), expressed as a function of the source-to-site distance and the magnitude. This shows the interest of working with a complete seismicity catalog expressed in magnitude. This statement implies to convert the intensity data into magnitudes, that we can name “equivalent magnitudes” or “macroseismic magnitudes”, to differentiate them from the instrumental ones. The main difficulty is the large number of scales of both intensity and magnitude. The use of a magnitude that does not saturate for large earthquakes, as the moment magnitude Mw, is recommended. So, all data need to be converted into a reference magnitude, which has to be the same as the one used in the GMPE.
It is also important to reduce the number of conversions, each one adding supplementary uncertainties into the resulting hazard.

2.3.3. Distribution models

2.3.3.1. Determination of complete samples

The objective is to determinate the initial thresholds of magnitude and of date, from which the catalog can be estimated as complete, meaning both exhaustive (all data are presented) and homogeneous (all data expressed by the same variables).
This statistical work can be achieved by the χ^2 and more exactly, by the exceeding probability of the χ^2 distribution. Then, the results may be improved with a simple visual control of the seismic activity over time, by magnitude threshold and for different magnitude ranges. These methods may

also be improved by the knowledge of the history that influences the quality or the lack of data (wars, epidemic, etc), their source, the accurate knowledge of the implantation dates of the seismic networks, etc.

Other methods, based on the maximum likelihood methods, are used to obtain a complete catalog (Weichert, 1980).

2.3.3.2. Calculation of the distribution law parameters

Traditionally, the repartition model of the earthquake number as a function of the magnitude is given by the law of Gutenberg-Richter (1944):

$$\log_{10}(N(M)) = a - bM \tag{2.1}$$

N(M) expresses the annual number of earthquake of magnitude high or equal to the magnitude M. *a* and *b* represent the parameters of the regression curve. This equation may also be written:

$$N(M) = \lambda e^{-\beta(M - M_{min})} \tag{2.2}$$

where λ is the mean annual rate of earthquake of magnitude higher or equal to Mmin (magnitude threshold) and β has the same signification than the b-value, expressing the proportion of large earthquakes compared to small ones.

A significant minimum magnitude has to be chosen, related to the study region, to the seismotectonic context, to the available data sample and to the influence it may have in the hazard results. A threshold too low may diminish the statistic representativeness related to the earthquake detection threshold and does not provide anything in terms of hazard for earthquake engineering. Essential information on the determination of the seismic activity rate may be lost by using a threshold too high and may not provide the hazard levels for low return period. Generally, the minimum magnitude is taken between 3.0 and 5.0, according to the available catalog and to the period that is used.

2.3.3.2.1. Regression method

The most widely used is the least square method, by minimization of the root mean square. This method may be applied to the samples respecting both threshold and date criteria, described in the previous paragraph. Nevertheless, this method does not consider the introduction of a magnitude into the distribution model.

2.3.3.2.2. Adjustment of the truncated Gutenberg-Richter law

Another method consists in adjusting the truncated Gutenberg-Richter law. This truncation is given by the maximum magnitude, for example defined by the paleoseismology.

The equation is expressed as follow:

$$\log_{10}(N(M)) = a - b M_{min} + \log_{10}\left(1 - \frac{1-10^{-b(M-M_{min})}}{1-10^{-b(M_{max}-M_{min})}}\right) \quad (2.3)$$

or

$$N(M) = N(M_{min})\left(e^{-\beta(M-M_{min})} - e^{-\beta(M_{max}-M_{min})}\right)/\left(1-e^{-\beta(M_{max}-M_{min})}\right) \quad (2.4)$$

They may also be written as:

$$a = \log_{10}(\lambda t) + b M_{min} \quad (2.5)$$

and

$$b = \frac{\beta}{\ln(10)} \quad (2.6)$$

As described before, the minimum magnitude, M_{min}, is defined with the χ^2 test. M_{max} corresponds to the largest magnitude expected in this source zone, described as the Maximum Credible Earthquake (MCE).

2.3.3.2.3 Methodology of maximum likelihood

Another method is the "maximum likelihood", developed by Kijko and Sellevoll (1992). Different parts of the seismicity catalog are considered:

- The extreme part, corresponding to historical earthquakes, where statistical analysis is poorly constrained. Extreme values are considered in the historical period.

- Complete parts, corresponding to the different periods that do not have to overlap themselves and for which the magnitude threshold decreases with the contemporaneity of these periods. This decrease is explained by the improvement of data organization (databases) and the recent development and/or improvement of seismic networks.

Besides, this method allows integrating periods without information (e.g., revolutions, wars), and uncertainties on the magnitude values and with a maximum magnitude value corresponding to the MCE.

2.3.3.2.4 Characteristic earthquake model

For regions where faults are extended, the observed return periods of large earthquakes, deduced from the paleoseismology, are found lower than the ones given by the historical seismology. Several models of recurrence have suggested to integrate this particularity, among which the characteristic earthquake model that was developed by Schwartz and Coppersmith (1984). The parameters of seismic activity (or seismic rate) can be deduced from the slip rates, obtained from geodesic data.

The calculation of the activity rates depends on the fault size and on the maximum magnitude.

2.3.3.2.5 Gutenberg-Richter law or Characteristic earthquake model?

Parsons et al. (2009) proposed a model to weigh the evidence that supports characteristic earthquake against a simpler model made from the extrapolation of Gutenberg-Richter law to an individual fault zone. They showed that giving a preference to either model in calculating future earthquake rates is not justifiable. Nevertheless, an important influence on using a linear Gutenberg-Richter model is how a fault zone is defined in terms of which small earthquakes can be associated with it. However rate uncertainties, related to catalog selection, are quantifiable and transferable to forecast uncertainty, which is in contrast with the often unwieldy and sometimes unquantifiable uncertainties associated with characteristic earthquake model (Parsons, 2009).

2.3.3.3 Maximum Credible Earthquake: determination of the maximum magnitude

The objective is to define the maximum magnitude in order to truncate the earthquake magnitude distribution into the adjustment models of the Gutenberg-Richter law, of the maximum likelihood or of the characteristic earthquake model. This determination of the maximum magnitude may be achieved by different adjustments: by reference to the historical seismicity (minimum limit), by tectonic considerations (structures and dynamic), by the determination of the parameters of the magnitude distribution law using the maximum likelihood.

2.3.3.3.1. Exploitation of the historical seismicity catalog

The maximum magnitude of a historical seismicity catalog, most of the time poorly constrained, is a weak indicator of the Maximum Credible Earthquake (MCE). It is, at the most, an inferior limit of the maximum magnitude. The exploitation of the historical seismicity data by methods of physical limit investigation may contribute to estimate the maximum magnitude. In region where the seismic sources are well defined faults, the relative sizes of earthquakes may be expressed with geometrical parameters, as the slip rate or the fault area implied in the rupture process. The seismic moment is the parameter that uses these quantities and was defined by Aki (1966) as:

$$M_0^{Max} = \mu A D \tag{2.7}$$

where μ is the shear modulus of the rock involved in the earthquake. D is the average displacement on the area A of the rupture along the geologic fault where the earthquake occurred. The assumption of this method is that the quantity of cumulated co-seismic deformation along the time is uniform and proportional to the sum of the square roots of the released energy for each event: $D=\Sigma E^{1/2}$. Assuming that the deformation is uniform along the time, it is possible to limit the cumulated deformation quantity between two parallel lines, one passing by the cumulated deformation minima and the other by the cumulated deformation maxima. These lines correspond to physical limits of the deformation, at least for the observational time. The distance between the two lines gives the maximum released energy, allowing estimating the maximum magnitude of an earthquake.

In area of low to moderate seismicity, where geological faults are not characterized well enough, the maximum magnitude of a historical seismicity catalog may be directly used, increased with an

arbitrary coefficient, to estimate the MCE.

2.3.3.3.2. Exploitation of the geometric characteristics of the active structures

For the source faults, the maximum magnitude is often determined with their geometric characteristics (most of the time with the length) and is deduced from empirical laws (Wells and Coppersmith, 1994). According to the fault system structure, the main challenge is to define the length of the fault that may be involved into the rupture process. Indeed, it is crucial to determinate if a segmented fault may break in its whole length or if only few segments will be implied into the rupture process. The maximum magnitude, defined for the PSHA calculation of the Fukushima power plant, was 7.5 considering a rupture of this fault in different segments with several moderate earthquakes. Unfortunately, the rupture of the 2011 Tohoku earthquake implied different segments of the geological fault, generating a M_w = 9.0 earthquake, leading to one of the most dramatic disaster made by a natural process.

2.4. Temporal probabilistic models

2.4.1. Poisson model

This standard model of future earthquake occurrence is the Poisson model. It is the simplest model, because no more data, than the ones required to describe the magnitude distribution model, supposed independent in time, are required to the recurrence model. The main property of this model is the absence of memory on the past events. The probability distribution in time of the next earthquake is independent of the date of occurrence of the previous one. This leads to:

- an exponential distribution of the inter event times with a coefficient of variation equal to 1. The coefficient of variation is equal to the square root of the standard deviation divided by the expected value:

$$V(\tau)=[Var(\tau)]^{1/2}/E(\tau) \tag{2.8}$$

- the hazard function h(t) is defined as:

$$h(t)=\frac{\lambda e^{-\lambda t}}{e^{-\lambda t}}=\lambda \tag{2.9}$$

  This function is constant in time. It is typically the case for a function without temporal memory.

- the magnitude and location of the next earthquake are supposed independent of the magnitude and location of the previous earthquake.

Most of these assumptions do not correspond to our conception of the tectonic processes on individual faults, but lead to reasonable results for time intervals and risk levels that interest the conventional structures and the risk infrastructures.

For a stationary Poisson model, the cumulative distribution function (cdf) is equal to:

$$F(t)=1-e^{-\lambda t} \tag{2.10}$$

The probability distribution function (pdf) of the inter event time is expressed as follow:

$$f(t)=\lambda e^{-\lambda t} \tag{2.11}$$

2.4.2. Renewal models

The use of the Poisson model may overestimate the hazard, when the elapsed time since the last event is short, or, on the contrary, may underestimate it when the elapsed time since the last event is long. This observation is important, especially for region of low to moderate seismicity, where the return period of significant events may be several centuries. So it is suitable to introduce a temporal dependency into the earthquake occurrence processes for PSHA calculations (Kagan and Jackson, 1996; Console, 2001; Luen and Stark, 2008; Mosca et al., 2012).

2.4.2.1. Definition

The renewal model of the seismicity links the magnitude distribution of events to the inter event time distribution. The first event occurred after a random time τ_1, since the initial time (t=0) of the process. Then, the process generates itself until the occurrence of the second event, after a random time τ_2. The intervals between the occurrence dates are, then, independent and identically distributed. The occurrence dates of the events, or renewal, $t_1 = \tau_1$, $t_2 = \tau_1 + \tau_2$, …, $t_n = \tau_1 + ... + \tau_n$, constitute a renewal process.

The occurrence rate of events evolves in time and return to the initial value after the occurrence of a significant event.
Obviously, these temporal models are chosen in such a way that their hazard function h(t) increases, meaning that the occurrence probability of an event increase in time. The Gamma or Weibull renewal models include this characteristic.

2.4.2.2. Gamma renewal model

In mathematics, the gamma function (represented by the capital Greek letter Γ) is an extension of the factorial function, with its argument shifted down by 1, to real and complex numbers.
The cumulative density function of a Gamma renewal model is described by:

$$F(t)=\frac{1}{\Gamma(p)}\int_0^t \lambda^p x^{p-1} e^{-\lambda x}\,dx\,;\forall\, t\geqslant 0\,;(p,\lambda)>0 \tag{2.12}$$

p corresponds to the shape parameter.
The corresponding probability density function is expressed as follow:

$$f(t)=\frac{1}{\Gamma(p)}\lambda^p t^{p-1} e^{-\lambda t} \tag{2.13}$$

The equation of the hazard function is:

$$h(t)=\frac{\lambda^{p} t^{p-1} e^{-\lambda t}}{\Gamma(p)-\lambda^{p}\int_{0}^{t} x^{p-1} e^{-\lambda x}\,dx} \tag{2.14}$$

If p>1, the hazard function is increasing, meaning that the temporal dependency is positive. It is the "normal" case of temporal dependency, in a process of stress accumulation and their release, with an increase of the annual probability (λ) or of the hazard function with the time, after the last significant event.
If p=1, we get back to the poissonian formulation, h(t)=λ with Γ(1)=1.

2.4.2.3. Weibull renewal model

In probability theory and statistics, the Weibull distribution is a continuous probability distribution. It is named after Waloddi Weibull who described it in detail in 1951, although it was first identified by Fréchet (1927) and first applied by Rosin & Rammler (1933) to describe a particle size distribution.
The cumulative density function of the Weibull function is described by:

$$F(t)=1-\exp(-\lambda t^{\nu});\forall\, t\geqslant 0\,;(\lambda,\nu)>0 \tag{2.15}$$

where v corresponds to the shape parameter.

The corresponding probability density function is:

$$f(t)=\lambda\,\nu\, t^{\nu-1}\exp(-\lambda t^{\nu}) \tag{2.16}$$

and the hazard function:

$$h(t)=\lambda\,\nu\, t^{\nu-1} \tag{2.17}$$

If *v* >1, the hazard function is increasing and the temporal dependency is positive. It is the "normal" case of temporal dependency, in a process of stress accumulation and their release, with an increase of the annual probability (λ) or of the hazard function with the time, after the last significant event.

2.4.2.4. Log-normal model

The probability density function of the log-normal distribution model is expressed as follow:

$$f(t)=\frac{1}{t\,\sigma\sqrt{2\pi}}\exp\left[\frac{-(\ln(t)-m)^{2}}{2\sigma^{2}}\right];\forall\, t\geqslant 0 \tag{2.18}$$

The log-normal model has the particularity to decrease after 166 years, for a mean inter event time of 100 years. The random variable ln(t) follows a normal distribution of expected value m and of standard deviation σ.

2.4.2.5 Brownian Passage-Time model

This model was originally introduced by Ellsworth et al (1999) and Matthews et al (2002) to provide a physically-motivated renewal model for earthquake recurrence. It is based on the properties of the Brownian relaxation oscillator (BRO). A Brownian passage-time model considers an event as a realization of a point process in which a new earthquake will occur when a state variable (or a set of them) reaches a critical failure threshold (χ_f) and at which time the state variable returns to a base ground level (χ_0). Adding Brownian perturbations to steady loading of the state variable produces a stochastic load-state process. An earthquake relaxes the load state to the characteristic ground level and begins a new cycle.
In the conceptual Model of Matthews et al (2002) the loading of the system has two components: (1) a constant-rate loading component λt, and (2) a random component, σW(t), that is defined as a Brownian motion (where W is a standard Brownian motion and σ is a nonnegative scale parameter). Standard Brownian motion is simply integrated stationary increments where the distribution of the increments is Gaussian, with zero mean and constant variance. The Brownian perturbation process for the state variable χ_t is defined as:

$$X(t) = \lambda t + \sigma W(t) \tag{2.19}$$

An event will occur when $\chi(t) \geq \chi_f$. The BRO are a family of stochastic renewal processes defined by four parameters: the drift or mean loading (λ), the perturbation rate (σ^2), the initial stress state (χ_0), and the failure state (χ_f). On the other hand, the recurrence properties of the BRO (repose times) are described by a Brownian passage-time distribution which is characterized by two parameters: (1) the *mean time* or period between events, (μ), and (2) the *aperiodicity* of the mean time, α, which is equivalent to the familiar coefficient of variation. The probability density for the Brownian passage-time model is given by:

$$f(t) = \left(\frac{m}{2\pi\alpha^2 t^3}\right)^{1/2} \exp\left[\frac{-(t-m)^2}{2m\alpha^2 t}\right] \tag{2.20}$$

This distribution has the following noteworthy properties: (1) the probability of immediate re-rupture is zero; (2) the hazard rate increases steadily from zero at $t = 0$ to a finite maximum near the mean recurrence time and then decreases asymptotically to a quasi-stationary level, in which the conditional probability of an event becomes time independent; and (3) the quasi-stationary failure rate is greater than, equal to, or less than the mean failure rate because the coefficient of variation is less than, equal to, or greater than $1/\sqrt{2} \approx 0.707$.

2.5. Ground Motion Prediction Equations (GMPEs)

2.5.1. Classic formulation

GMPEs calculate the amplitude of ground motion on a specific site of an earthquake, characterized by its magnitude and its source-to-site distance. Because strong motion data are, generally, sparse, the uncertainties are integrated into the GMPE. Most of the time, the general form of a GMPE is as follow:

$$\ln(amplitude) = f(M, R) + \varepsilon \tag{2.21}$$

M represents the magnitude, R the source to site distance and ε describes the dispersion. The amplitude may be the maximum acceleration (PGA: Peak Ground acceleration), the maximum velocity (PGV: Peak Ground velocity), the maximum displacement (PGD: Peak Ground Displacement) or the response spectrum for different discrete frequencies and a specific damping ratio (usually equal to 5%).
The distance R may be hypocentral, epicentral or the closest horizontal distance. ε is a random variable, obeying to a normal distribution of null mean and of standard deviation σ_ε. Generally, it is observed that this standard deviation is higher for the sites composed by rocks than the ones composed by soils.

The function *f(M,R)* is usually expressed as:

$$f(M, R) = \alpha + \beta M + \gamma \ln(R + g(M)) + \delta R \tag{2.22}$$

α, β, γ and δ are constants. According to the earthquake magnitude and to the source-to-site distance, the response spectrum may vary, particularly for low frequencies. In this way, a long bridge will be more sensible to the motion generated by large earthquakes several hundred kilometers away while a nuclear power plant will be more sensible to earthquakes, even of low magnitudes, located within a hundred kilometers. That is why, it is essential to do not restrict a PSHA survey to the determination of the PGA, but to calculate spectrum accelerations or pseudo-velocities for several frequencies that correspond to the frequency domains of the structures of interest.

The Imperial College London report of Douglas (2004a) provided a summary of all GMPEs from 1964 until the end of 2003. The BRGM report of Douglas (2006), which summarized all GMPEs from 2004 to 2006 (plus some earlier models)The report of Douglas (2008), concerning GMPEs published in 2007 and 2008 (plus some earlier models).

2.5.2. Modification of the seismic signal

It is import to use the GMPEs that are appropriated to the seismotectonic context of the study area. Distinctions are done between the GMPES computed for stable intraplate zones, for interplate zones and for subduction zones. It is better to use regional GMPEs, obtained from accelerometric records of the study area. These records contain at the same time, the information related to the seismic

source, the information related to the propagation and, sometimes, the site effect, whatever it is geologic or topographic. Other effects may modify the seismic motion, as basin edges, directivity phenomenon or site effects (Atkinston et al., 2013).

2.6. The different kinds of uncertainty

Many PSHA studies incorporate systematically the sensitivity study of different parameters or of different models. For some of these studies, it is common to distinguish two kinds of uncertainty: the aleatoric uncertainty and the epistemic uncertainty.

2.6.1. Aleatoric uncertainty

This aleatoric uncertainty is inherent to the nature of future earthquakes and to their effects. It is associated with variations of the stress and deformation along geological faults, with variable dynamic processes of the source and propagation through a heterogeneous crust. It is simply linked to the unpredictable and aleatory aspect of a physical phenomenon. The addition of complementary data allows to better estimate this uncertainty, but it cannot be totally reduced.
For example, the date, location and size of an earthquake are related to the aleatoric uncertainty.

2.6.2. Epistemic uncertainty

The epistemic uncertainty is due to the incomplete knowledge and to the lack of data concerning the seismic process (e.g., Kulkarni et al., 1985; Coppersmith and Youngs, 1986; Stepp et al., 2001; Abrahamson et al., 2001). This is expressed by simplified models of the seismic process, but also by the uncertainty related to the parameters of the model. This uncertainty may be reduced by the addition of new data.
The non-quantified deviations between the model and the reality (e.g., non-uniform seismic activity rate, deviations related to the Poisson process) and the quantified uncertainties of the model parameters (e.g., fault geometry, parameters characterizing the seismic activity, GMPEs coefficients) are related to the epistemic uncertainty.

2.6.3. Including uncertainties into PSHA calculations

Any hazard calculation has to be associated with its related uncertainty. The uncertainties are found in different steps of PSHA: seismotectonic zoning, seismic sources (surfaces, faults, points), earthquake characterization (conversions), homogenization and completness of the seismicity catalogs, determination of the parameters characterizing the seismic activity (Gutenberg-Richter law parameters, M_{min}, M_{max}), temporal probabilistic model, GMPEs, etc.
To include these uncertainties into PSHA calculations, two methods are mainly used.
The first one consists in defining the standard deviations. According to the target degree of confidence (from the obtained results), an increase of one or two standard deviations may be taken. According to a normal distribution, the first case ($m+\sigma$) correspond to the probability of 84% that the obtained value is lower than its increase. In the second case ($m+2\sigma$), this probability is equal to 97.5%.
The second method consists in the use of logic trees. Kulkarni, Youngs and Coppersmith (1984),

first introduced the logic tree in PSHA as a tool to capture and quantify the uncertainties related to PSHA. This conceptual tool is useful for the presentation of the main parameters of the model, particularly when they are not independent. The figure 2.3 presents an example of such a logic tree. A hazard curve (or hazard map or uniform hazard spectrum) may be associated to each ending branch of the logic tree. To process these uncertainties, a Monte Carlo simulation is achieved. This approach allows using continue and discrete distributions of quantities affected by uncertainties. Several simulations are required to obtain reliable results.

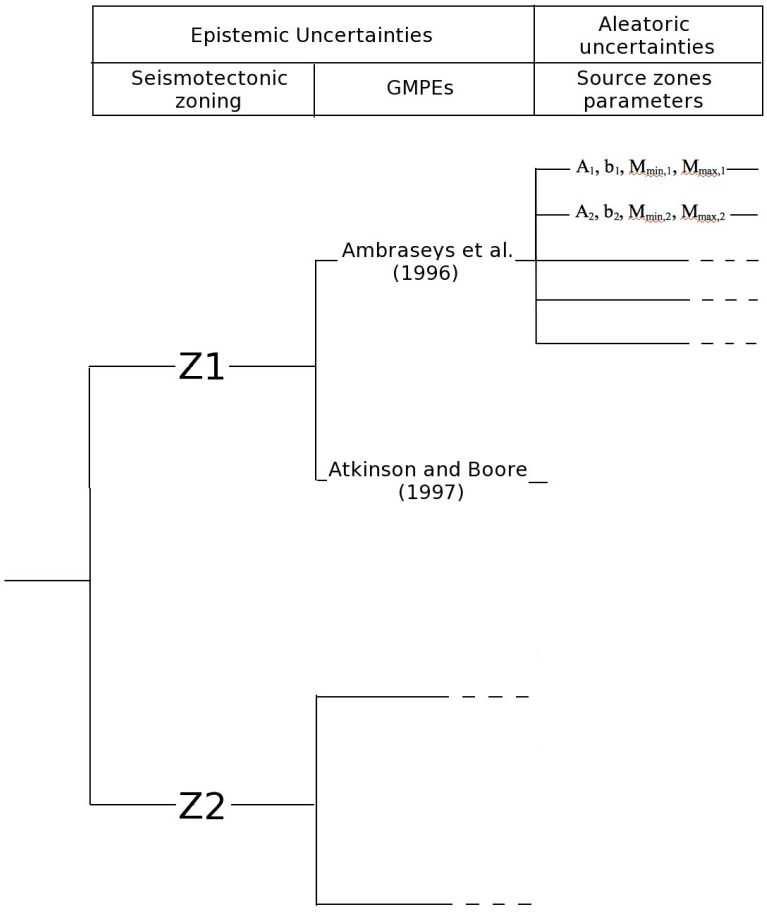

Figure 2.3: Logic tree representation for different parameters affected by an uncertainty. a_1 and b_1 are the parameters of the magnitude-frequency relationship of the first model. $M_{min,1}$ and $M_{max,1}$ are, respectively the minimum and maximum magnitude considered in the first model. a_2 and b_2 are the parameters of the magnitude-frequency relationship of the second model. $M_{min,2}$ and $M_{max,2}$ are, respectively the minimum and maximum magnitude considered in the second model. Z_1 and Z_2 represent two different seismotectonic zonings.

2.7. Seismic hazard representation

2.7.1. Hazard curves

Usually, the hazard curves are calculated and represented for the PGA, or for spectral accelerations or pseudo-velocity corresponding to different frequencies of the structures. These curves,

logarithmically decreasing, give the annual rate of exceeding one of the previously described parameters.
Because this result is calculated from laws and adjustments (e.g., conversions, magnitude distribution, GMPEs), an uncertainty is associated to these curves. So, it is suitable to represent the mean curve, the 84th percentile curve and the 16th percentile curve (figure 2.4). The 84th percentile curve corresponds to the addition of one standard deviation of the mean value. This means that, for a normal distribution, the probability to have a value lower than the mean value increased by one standard deviation, is equal to 84%. The 16th percentile curve corresponds to the decrease of one standard deviation of the mean value. This means that, for a normal distribution, the probability to have a value lower than the mean value decreased by one standard deviation is equal to 16%. The distance between the 16th and 84th percentile curves gives an indication of the uncertainty associated to the result.

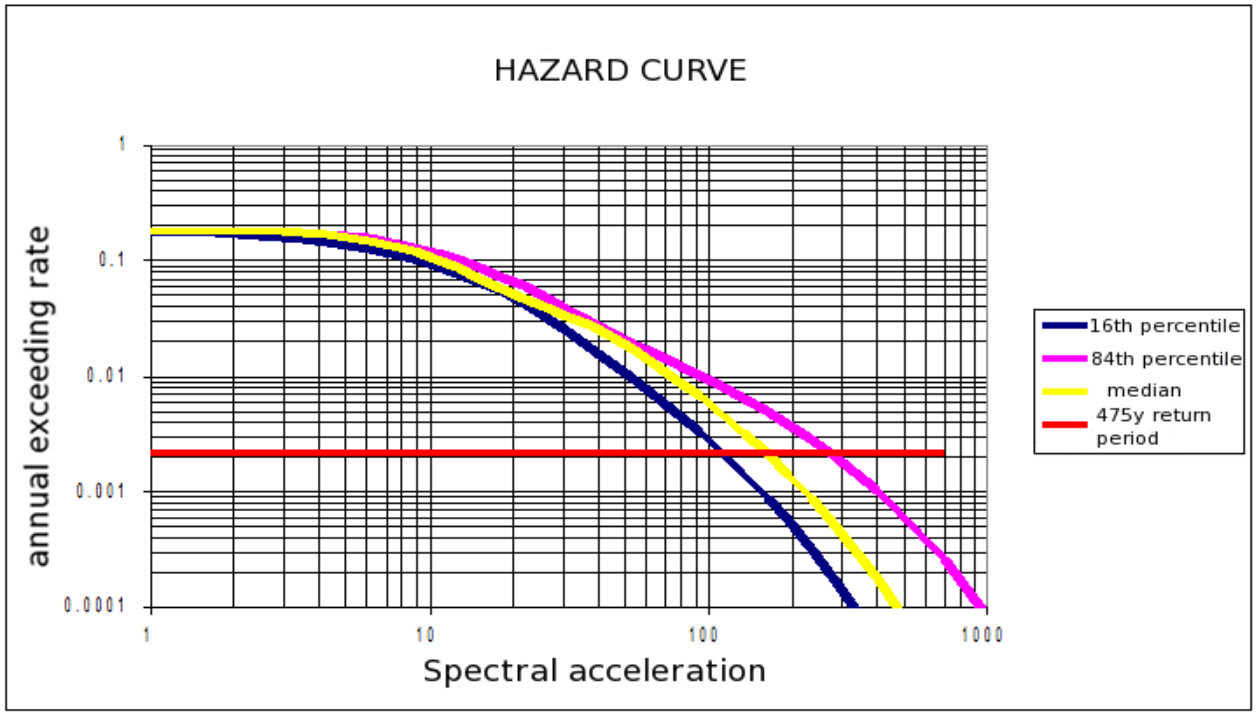

Figure 2.4: Hazard Curve. Representation of the annual exceeding rate of a ground motion parameter (displacement, acceleration, velocity) in function of the spectral acceleration

2.7.2. Uniform hazard spectrum

The Uniform Hazard Spectra (UHS) are obtained from the study of the spectral amplitudes, associated to some probability values of non-exceeding and this, for different frequencies (figure 2.5). The values of non-exceeding probability (P) of a parameter depend on the target structure and correspond to return periods (T). The usual return periods correspond to T= 200, 475, 5000, 10 000 years. The 475 years return period corresponds to a hazard with a 10% chance of exceedance in 50 years. This return period is used for the normal structures.
For each calculation, done for different frequencies, an Uniform Hazard Spectrum is achieved. The

shape of the response spectrum depends on the target annual exceeding probability. Lower this probability, higher the seismic impact levels and lower predominant frequencies (<5 Hz). Usually, the acceleration levels decreases with towards low frequencies (high spectral periods).
It is important to remind that a Uniform Hazard Spectrum does not represent a real seismic motion, but rather a probabilistic motion that may occur in a site for a target return period.

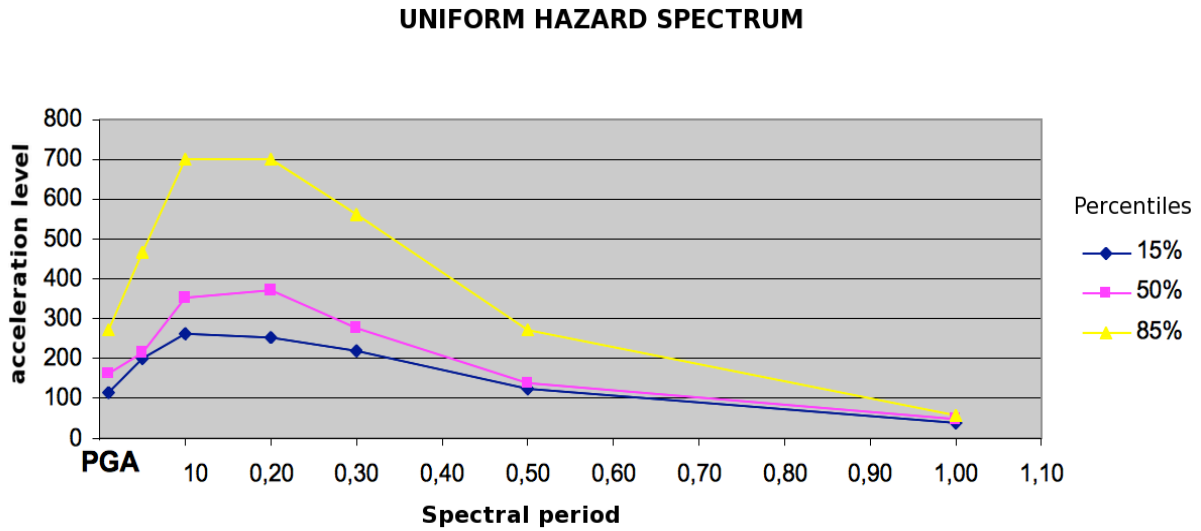

Figure 2.5: Uniform Hazard Spectrum, represented for a return period of 475 years. The acceleration level is given in cm/s² and the spectral period in seconds

2.7.3. Hazard maps

It is the representation mode the most widely used. Usually, a parameter of the ground motion is represented, associated to a hazard value (annual exceeding probability) (figure 2.6).

2.7.4. De-aggregation of the seismic hazard

The de-aggregation of seismic hazard indicates which are the magnitudes and the distances that most contribute to the calculated seismic hazard. The results of de-aggregation are obtained by calculating, one at a time, the contribution to the mean hazard from each magnitude-distance pair. The figure 2.7 shows a graphical representation of a hazard de-aggregation. This hazard calculation by spectral frequency, allows identifying which seismic sources most contribute to the hazard on a site by a de-aggregation of the hazard as a function of the magnitude and distance and, then, to proceed to a deterministic response spectra calculation, as a function of the most penalizing hypothesis. To individualize the dominating seismic sources of the hazard, it is important to achieve such a de-aggregation on the PGA (≈ 25 to 33 Hz) and for frequencies equal to 1 or 10 Hz.

This de-aggregation allows identifying the mean magnitude-distance pairs, useful for the computation of more realistic ground motion (pseudo-deterministic). In this way, we know the characteristics of the reference earthquakes, directly from the results of the probabilistic analysis, corresponding to a certain exceeding probability and, therefore, coherent with the target protection

level. These seismic characteristics may allow to simulate synthetic accelerograms or to select real ones of similar characteristics.

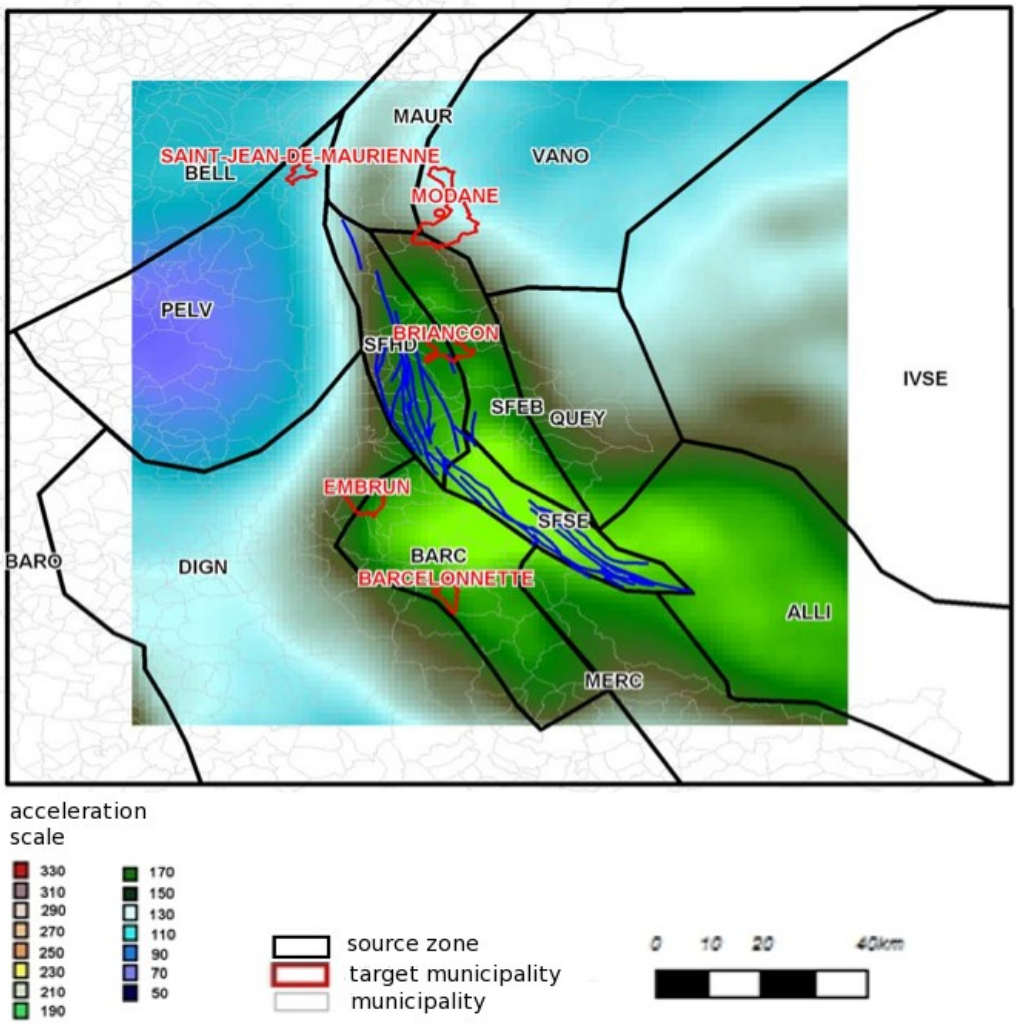

Figure 2.6: Hazard map of PACA region, France (Le Goff et al., 2009). The hazard is represented for a return period of 475 years. Acceleration scale in cm/s²

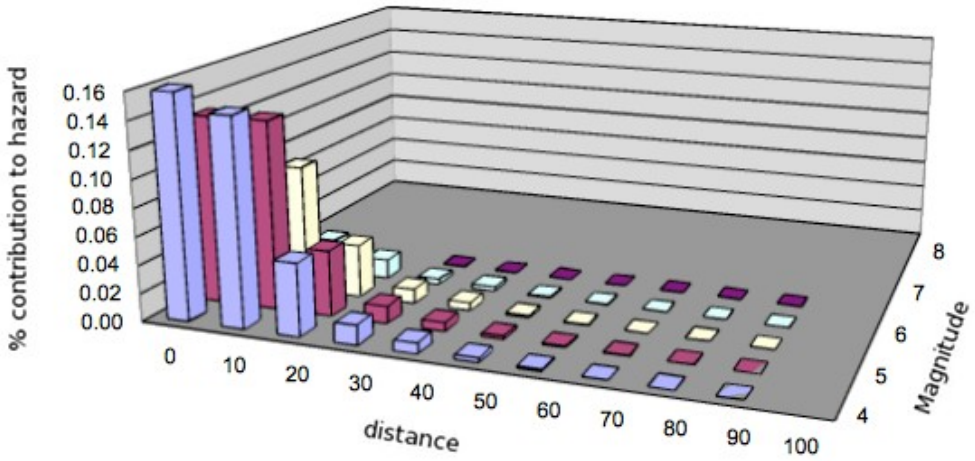

Figure 2.7: de-aggregation of the seismic hazard for a spectral period of 1s and a return period of 475 years (Le Goff et al., 2009)

2.8. Conclusion

The term Probabilistic Seismic Hazard Analysis is used for all seismic hazard analysis methods which attempt to define the frequency of exceedance of specified ground motion level. The PSHA may be decomposed in different steps: 1) the definition of earthquake sources, 2) the definition of seismicity recurrence characteristics for each source, 3) the development of Ground Motion Prediction Equations (GMPEs), 4) the development of uniform hazard spectra for different probabilities of exceedance and development of hazard curves, 5) the de-aggregation of the hazard to develop scenario events defined by magnitude distance pairs.

A special application of PSHA methods is the earthquake resistant design of critical infrastructures. Critical infrastructures include nuclear power plants, radioactive waste repositories, chemical plants, bridges, military plants, liquefied gas pipelines and dams as well as emergency infrastructures. Another application is related to risk analysis, which may be separated between the risk insurance problem and the technical risk. The first one corresponds to the estimation of capital and life losses caused by earthquakes whereas the second one is the evaluation of the risk associated with the operation of a critical infrastructure with respect to a possible environmental impact.

According to Klügel (2008), the traditional probabilistic seismic hazard analysis methods have significant deficiencies, limiting their applications. These deficiencies have their roots in the use of inadequate probabilistic models and insufficient understanding of modern concepts of risk analysis. The seismic hazard results, made from an unrealistic model, are not robust (Musson, 2004). One of the requirements of seismic hazard analysis results must reflect the specific site conditions with respect to seismic activity. Some decisions, like the magnitude recurrence and occurrence model, can make the model unrealistic. The attempt to compensate these problems by a systematic use of expert decisions has not resulted in any improvement of the situation. In the traditional PSHA calculation, the source model is developed from seismological, geological, tectonical and geophysical data. The definition of seismic sources uses a model with zones, for regions where the seismicity is relatively low. This source model is composed by a spatial distribution model of the events, a magnitude-frequency relationship and an earthquake occurrence model, in order to define the characteristics of the sources.

The expert decisions used to achieve the seismotectonic zoning are not traceable back to the data that dominated the decision-making. Moreover, no information on the uncertainties are provided. Some other approaches, as statistical region classification (Weatherhill and Burton, 2009), are still not satisfying, because of their lack of robustness and the fact that, at best, only the seismic catalogs and the focal mechanisms are used.

The spatial distribution model of the events describes the location of the potential future earthquakes. In current PSHA practice, the spatial distribution of the seismicity is considered as uniform in a seismic source zone. Musson (2004) compares the spatial repartition of events from a synthetic catalog, using a uniform distribution, and from the real seismicity catalog. The results show a significant difference between the random spatial distribution of the synthetic catalog and the clustered real seismicity.
In each zone of the source model, activity parameters are calculated using a magnitude-frequency relationship. Generally, two models are used: the Gutenberg-Richter law or the characteristic earthquake model. The first one describes the magnitude-frequency as a linear power law. The events are extracted from the historical and instrumental catalogue and activity parameters are extrapolated. Then these parameters may be used to draw a synthetic catalog and one can observe that more synthetic data are produced than real ones (Musson, 2004). The second one follows a

linear power law, as the Gutenberg-Richter law, with a bump where characteristic large-magnitude earthquake happen with a higher rate than predicted extrapolation from the small to moderate magnitudes. This model is derived from paleoseismic observations and considers that characteristic earthquakes repeatedly rupture the same fault segments with the same magnitude and slip distribution. Parsons et al. (2009) proposed a model to weigh the evidence that supports characteristic earthquake against a simpler model made from the extrapolation of Gutenberg-Richter law to individual fault zone. They showed that giving a preference to either model in calculating future earthquake rates is not justifiable. Nevertheless, an important influence on using a linear Gutenberg-Richter model is how a fault zone is defined in terms of which small earthquakes can be associated with it. However rate uncertainties related to catalog selection are quantifiable and transferable to forecast uncertainty, which is in contrast with the often unwieldy and sometimes unquantifiable uncertainties associated with characteristic earthquake model (Parsons, 2009).

Another important characteristic of the source model is the earthquake occurrence. In most of seismic hazard estimations, the simplistic assumption of the Poisson model is made. This model is based on the fact that seismicity, in a specific time interval, is independent of the previous seismicity. Kuehn (2008) showed, using a (coupled) stress release model, that the inter-event distribution presents a better fit with a gamma distribution. He also exposed that the small earthquakes occur clustered (in time) and large earthquakes quasi-periodically. The stress drop model of Zöller (2007) presents the same gamma distribution approximation for the inter-event time. He underlines the importance of the number of observed data and the possibility to associate them to the model through Bayesian method. Incorporating paleoseismic markers into Bayesian methods, Fitzenz et al. (2010) showed that the inter-event time model can be expressed by a combination of other distributions (e.g., Weibull, BPT, lognormal), whose weighs are computed taking into account both priors and all available data.

The estimation of the Maximum Credible Earthquake is another controversial point. Indeed, the definition of this parameter required a large knowledge on the fault geometry (blind fault?) and on its rupture process (does an event stop to a segment boundary? Does it break all the fault length?). An uncertain definition of this parameter may lead to dramatic consequences (April 2011 Tohoku earthquake, $M_w = 9.0$; Aochi and Ide, 2011; Amon et al., 2011).

Finally, PSHA calculations are done to estimate the frequency of exceedance of specified ground motion level and not to predict an earthquake occurrence. So far, an earthquake is an unpredictable natural phenomenon. As remind by an INGV open letter, the best approach to protect population and buildings from collapsing is not through earthquake prediction but through the application of appropriate safety measures. The development of seismic hazard maps provides the specifications required by building codes to avoid collapse of buildings and the resulting fatalities, and the information to convey to the population the basic concepts of earthquake hazard, awareness, preparedness and response. The sentence announced against Italian scientists (INGV, DPC), related to the April 2009, M_w =6.3, Aquila earthquake, sets a precedent that could affect dramatically the relationship between scientists and decision makers. Scientists will become prudent to provide an opinion knowing that they can be incarcerate.

CHAPTER 3

Seismotectonic context of Portugal

3.1 Introduction

The Portugal mainland is located in the extreme south-west of the European continent and more specifically in occidental side of the Iberian Peninsula. The Portugal mainland has frontiers with Spain in the north and east part of the country and is delimitated in the west and south by the Atlantic Ocean. In terms of latitude and longitude, the Portugal mainland is included between the 37th and the 42th parallels north and between the 6˚ W and 9.5˚ W meridians (figures 3.1 and 3.2).
Portugal is also composed by two archipelagos. The archipelago of Azores is located in the northeastern part of the Atlantic ocean between the 36th and the 43th parallels north and, between the 25˚ W and the 31˚ W meridians. The archipelago of Madeira is situated between the 30th and the 33th parallels north and, between the 13˚ W and the 18˚ W meridians (figures 3.1 and 3.2).

In this chapter, the seismotectonic and the seismicity of Portugal will be presented. The seismotectonic structures of Portugal can be divided into 3 different parts: the oriental part (composed by the Portugal mainland and its continental margins), the central part (related to the archipelago of Madeira and the oceanic part) and the occidental part (corresponding to the archipelago of Azores) (figure 3.1).

3.2. Geodynamic and Seismotectonic context of the Portugal mainland

Portugal mainland is located on the occidental border of the Iberian Peninsula, in a junction of a continental margin, influenced by the North Atlantic opening, with a zone of plate boundaries. The Portugal mainland presents a seismicity considered as low to moderate (Borges et al., 2001), due to its geographic proximity to an active region, which stretches from Gibraltar to the Azores and constitutes the boundary of two plates: the Eurasian plate and the Nubian plate. The relative movement of these plates is responsible of the Portuguese tectonic structures and the significant neotectonic activity (Cabral, 1993). This zone is commonly named “Azores-Gibraltar fault”, even if it is not a well-defined fault but rather a region of influence that results of the interaction between two tectonic blocs. The regional geodynamic evolution is controlled by a slow convergence, of around 4 millimeters per year (Argus et al., 1989; Buforn et al., 2004), relatively to the Eurasian plate and the Nubian plate with a NNW-SSE to NW-SE direction.
In the occidental region of the Mediterranean sea, the relatively slow movement of the plates and the low deformation rates are related with the large inter-event interval of large earthquakes, leading to difficulties to interpret the seismicity and the few geomorphologic markers (Nocquet and Calais 2004).

The Azores-Gibraltar fault is characterized by different tectonic behaviors: the zone of the Gorringe Bank (GB) and of the Cadiz Gulf (CG) is dominated by a compressive regime, while a strike-slip fault with right-lateral motion (Buforn et al., 1988) is observed in the central segment, defined as the Gloria fault (GF). This Gloria fault presents an E-W direction. The Gorringe Bank zone is characterized by a large anomaly of gravity. Lonergan et al. (1997) and Gutscher et al. (2002) showed the existence of a subduction zone (from West to East) below the strait of Gibraltar. The Atlantic margins of Portugal are characterized by a complex bathymetry, constituted by large submarine mountains, lined up in the E-W and ENE-WSW directions, which included the Gorringe Bank, one of the principal seismic sources of the Iberian Peninsula and of the North Africa (Moreira, 1985; Buforn et al., 1988; Buforn et al., 2004), and the Ampere Bank (Bezzeghoud and Borges 2003). According to data of seismic reflection and of seismic refraction, the Gorringe Bank is considered as a high bloc, composed by material of the oceanic crust and of the upper mantle

(Carrilho 2005). This structure is surrounded by deep abyssal plains, in particularly the Tagus Plain (TG) and the Ferradura Plain (FD). In this region, between the Gorringe Bank and the West coast of Portugal, a large structure was evidenced as the "Marquês de Pombal fault" (FMP) (Zitellini et al. 1999). This fault presents a scarp of 50 kilometers long, with a difference of elevation of 1 kilometer and is not detectable in its both north and south ends. The elevation of about 1100 meters (Zitellini et al 2001), shows that this fault is active. In this region, the seismicity is sparse and makes the plate boundary delimitation difficult to be established. This sparse seismicity may be explained by: 1) a natural sparse seismicity or 2) the uncertainty related to earthquake location. The second hypothesis is more likely due to the unfavorable seismic network distribution (lack of submarine seismic seismometers) (Bezzeghoud et al., 2012).

In the Portugal mainland, several faults are identified and are responsible of the intra-plate seismicity: the Nazaré fault (NF), the fault system of the Low Tagus Valley (LTV), the Messejana fault (MF) and the Cádiz-Alicante fault (CAF).

The zone of the archipelago of Azores is located on the boundaries of 3 tectonic plates, the North American plate, the Eurasian plate and the Nubian plate. These three boundaries are connected in a point called the Azores triple junction. This interaction between the three plate boundaries leads to a significant seismic activity.

The study of the seismicity of Portugal may be divided into three different zones, according to the seismicity features, the morphologic and tectonic structures and the geodynamic behavior (Bezzeghoud et al., 2012). The occidental part corresponds to the archipelago of Azores and extends to the mid-Atlantic ridge. The central part is related to the Glória fault, incorporating the archipelago of Madeira. The oriental part includes the Portugal mainland and its margins.
The study of Duarte et al. (2013), on the process of passive margin reactivation, proposes that a new subduction zone is forming at the Southwest Iberian Margin (SIM), as a result of both propagation of compressive stress from the Gibraltar Arc and stresses related to the large-scale Nubian-Eurasia convergence.

3.3. Seismicity and focal mechanisms

Our study area is focused on the Portugal mainland and its adjacent margins. So, the description of the seismicity will be restricted to the oriental part.

3.3.1. Seismicity

The seismic activity of the Portugal mainland, and especially the south, may be considered as a region of special attention in the study of the seismicity. The instrumental seismicity reveals a heterogeneous distribution of epicenters, with a main concentration in the south and in the adjacente oceanic margin, the zone of Évora and in a large band in the north of Lisbon, between the Low Tagus Valley and the coast. It is a seismic activity characterized by moderate events ($M < 5$) with some larger events ($5 \leq M \leq 7.8$), which mainly occurred in the south coast and the SW. The figure 3.2 presents the earthquake epicenters covering the period from 1961-2013 (provided by the IPMA). The seismic activity of the different regions presented above is described separately.

North

The inner north of Portugal and the Galicia region are mainly described by the seismic sets of November 1995 and May 1997. The last one initiated with an earthquake of magnitude 5.4, but was not responsible of any damages in Portugal (Senos and Carrilho 2003).

Tagus Valley and west margin

This area corresponds to a band, along the west margin of Portugal, from Lisbon to the latitude 40˚N and limited in east by the Low Tagus Valley. The largest instrumental earthquake recorded in this zone occurred in April 1999, with a magnitude of 4.6, and is associated to the Nazaré fault (Senos and Carrilho 2003). In spite of the low magnitudes recently recorded, it is the zone where occurred the earthquakes with the largest impact on the population. Among these events, the historical earthquakes of 1344 and 1531 (Sousa et al. 1992) generated large destruction in Lisbon, with a maximum intensity of IX in Benavente, Vila Franca de Xira and Lisbon. In this same zone occurred the 23th of April 1909 Benavente earthquake, with a magnitude of 6.0 (Teves-Costa et al 1999, 2005; Dineva et al., 2002, Stich et al. 2005; Teves-Costa and Battló, 2010; Cabral et al., 2012). The epicenter is located in the south part of the Low Tagus Valley fault system. The most affected places were the locality of Samora, Correia and Benavente where 46 people died. The seismicity of the Tagus Valley is presented in the figure 3.3.

Évora region

This region is characterized by a band, with around 40 kilometers in the north of Évora, with a sparse seismicity where four earthquakes of M > 4 occurred in the last four decades (4th of July 1987, M = 4.3; 31th of July 1998, M = 4.1; 29th of December 2005, M = 4.5; 27th of March 2010, M=4.1). No tectonic structure can be associated with a reasonable level of confidence to these events.

Algarve

The distribution of the earthquakes shows a concentration of small events in the area of Monchique. The analysis of the events located with a mobile seismic network (Instituto Português do Mar e da Atmosfera), in activity in Algarve between 1999 and 2003, shows that from 544 located events, with magnitudes comprised between 1 and 3.5, 53% occurred in the region of Monchique. A relocation of the 288 best located events allowed defining two alignments of epicenters; one obvious in the region of Monchique orientated ENE-WSW (azimuth of 256˚) and another one NNE-SSW that extends from this same region until the coast. This seismicity is concentrated in depth between 5 and 15 kilometers, without any observation in the first 5 kilometers (Caldeira et al. 2007). More recent studies, achieved from data of a mobile seismic network (project “tomografia sísmica da crusta Algarvia”) and distributed in the lower Alentejo and Algarve, allow identifying local events of very low magnitude, not cataloged, that lines up with a NE-SW direction in the area of Almodôvar, in the lower Alentejo (Rocha et al. 2009).

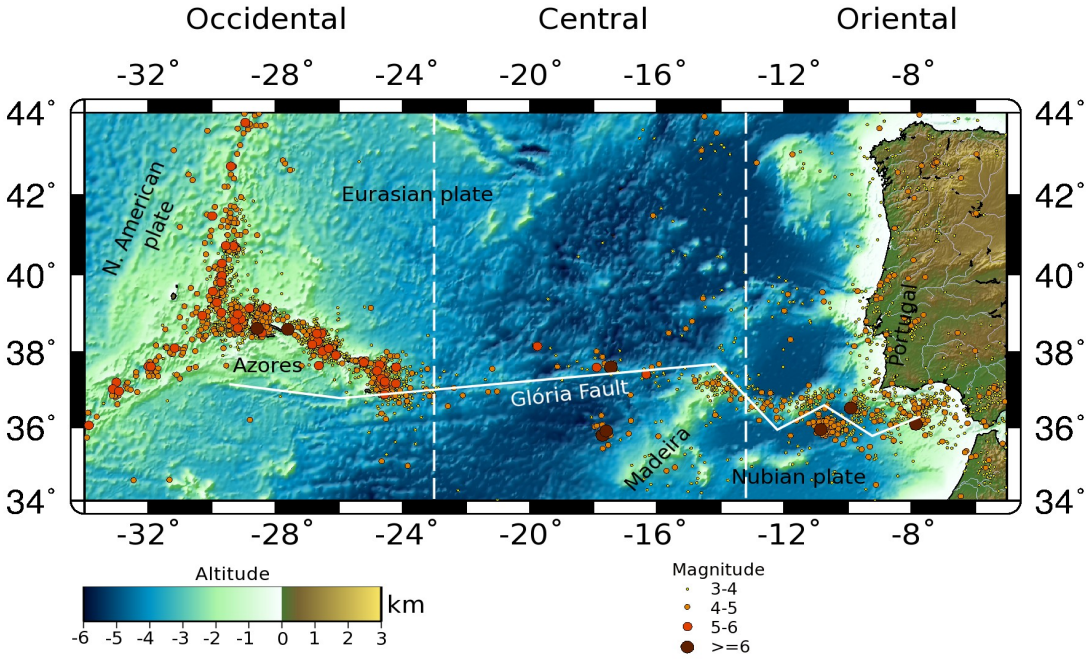

Figure 3.1: Geodynamic divisions of the Portugal mainland and the archipelagos of Azores and Madeira, with a boundary between the Eurasian, Nubian and North American plates. (From Bezzeghoud et al., 2012)

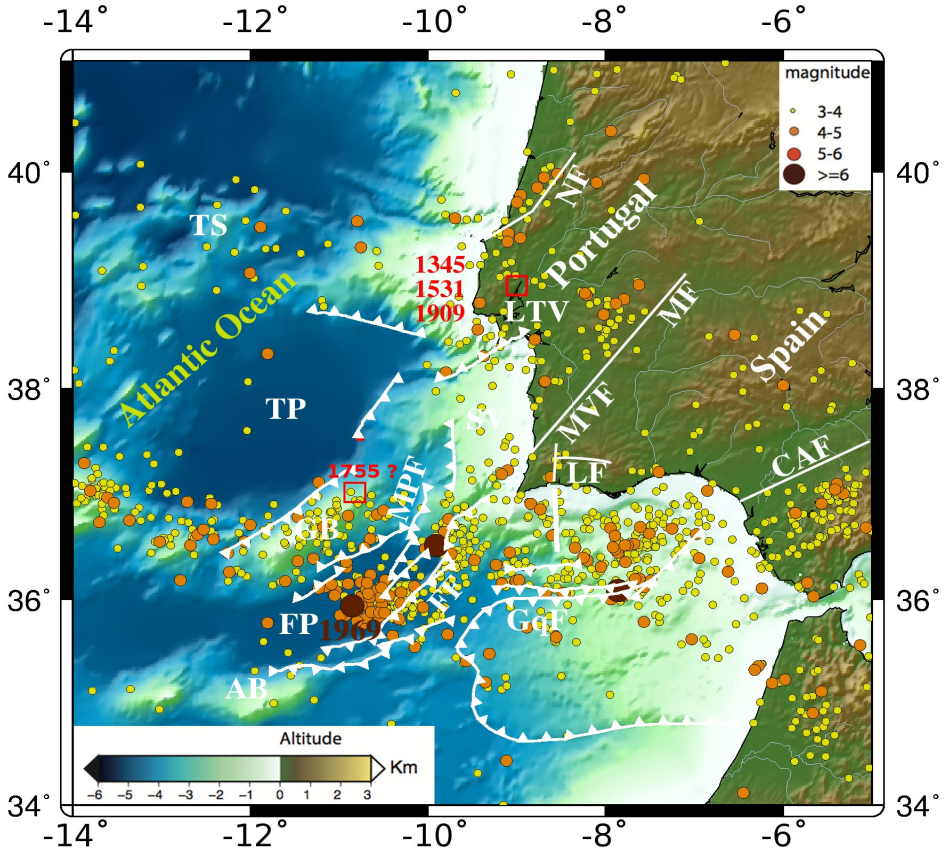

Figure 3.2: Instrumental seismicity (1961-2013, from IPMA) and location of the main historical earthquakes of the Portugal mainland and its adjacent margins. GB: Gorringe Bank; TP: Tagus Plain; TS: Tore Seamount; FP: Ferradura Plain; AB: Ampere Bank; FF: Ferradura Fault; GqF: Guadalquivir Fault; LTV: Low Tagus Valley; SV: Sado Valley; MPF: Marquês de Pombal Fault; NF: Nazaré Fault; MF: Messejana Fault; MVF: Moura-Vidigueira Fault; LF: Loulé Fault; CAF: Cadiz-Alicante Fault. (From Perreira et al., 2013)

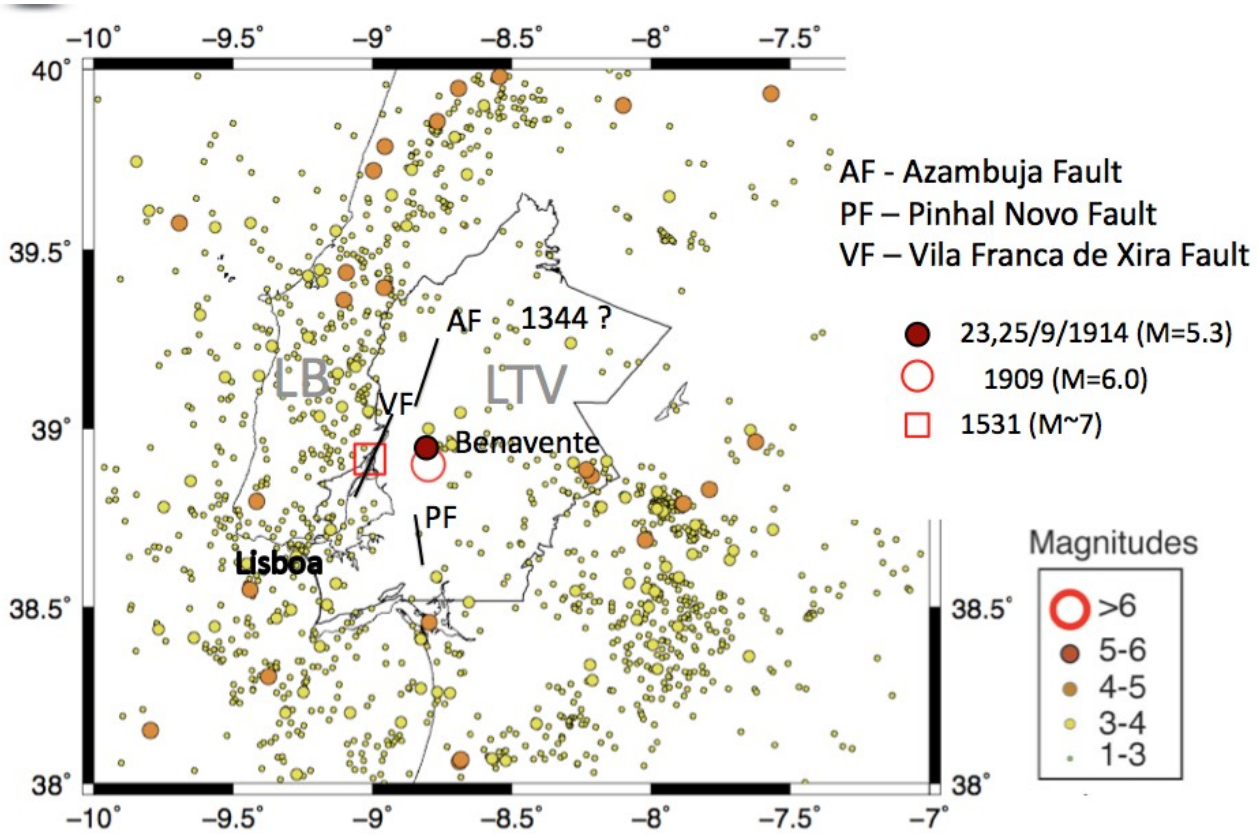

Figure 3.3: Instrumental seismicity (1961-2013) of the Low Tagus Valley. LB: Lusitanian basin; LTV: Low Tagus Valley

South-west of the Cape Saint Vincent

The region in the south-west of the Cape St. Vincent, between the Gorringe Bank and the Portuguese west coast, is one of the most active seismogenic zone. The events occuring in this zone are, usually, superficial (depth < 40 kilometers) and present moderate magnitudes (M < 5.0). Nevertheless some rare large earthquakes already occurred. It is in this region that the big 1755 Lisbon earthquake (M ~ 8.5) is located, as well as the 28th of February 1969 earthquake (Ms = 8.1), the 21th of December 1972 event (Ms = 5.8), the 12th of February 2007 event (Mw = 6.0) and the 17th of December 2009 earthquake (Mw = 6.0).

The 1755 earthquake, called Lisbon earthquake, was one of the most destructive earthquake. It occurred the 1th of November 1755, at 9:30 a.m., and was felt in the whole Europe and North Africa. This earthquake generated a huge fire, followed by a tsunami that overcame Lisbon and all the coastal region of Portugal, especially the region of Algarve, and that also reached the gulf of Cádiz, the north of Morocco, the Azores and Madeira. The maximum amplitude of the wave reached 10 to 15 meters in the south-west of Algarve and 6 meters in Lisbon. The combined effect of the earthquake, the fire and the tsunami caused large ravages in the city of Lisbon and an uncertain number of dead that exceeds several thousands. Its epicenter location is still uncertain, although 3 possible scenarios exist: 1) source in the Gorringe Bank (Johnston, 1996); 2) model of Marquês de Pombal fault (Zitellini et al. 1999, 2001, Terrinha et al. 2003); 3) model of subduction of the Cádiz gulf (Gutscher et al. 2002). According to the methodology of Grandin et al. (2007a), the most probable model is the one that corresponds to a source located in the Gorringe Bank (Grandin et al. 2007b).
The other large earthquake of this zone is the 28th of February 1969, at 02:42 a.m., felt in all the

Iberian Peninsula, in the Canary islands and in a large part of Morocco. Its epicenter, determined by the USGS (United States Geological Survey), is located about 180 kilometers in the south-west of the Cape St. Vincent, in the Ferradura plain, with a magnitude of 8.0. This earthquake generated a tsunami that reached a maximum amplitude of around 1 meter (Carrilho 2005) and was recorded in the tide gauges of the Portugal mainland, Azores, Spain and Morocco. Calculations of seismic intensities, achieved by Grandin et al. (2007b), using several source models, show that the best source model corresponds to a rupture that propagates unilaterally from the SW to the NE, with a velocity of 2.5 km/s on the fault plane of 82.5 kilometers long, 35 kilometers wide, with a top at a depth of 8 kilometers and angle of dip of 49.5˚. The seismic moment, calculated for this event, is $M_0 = 6.0 \times 10^2$ N.m (Mw = 7.8).
The 12th of February 2007 earthquake occurred at 10:35 a.m., in the Ferradura plain. The magnitude calculated for this event is Mw = 6.1 and was felt in the Portugal mainland, in particularly in Algarve, in the south of Spain and the east of Morocco. The 17th of December 2009, at 01:28 a.m., occurred another event (Mw = 5.5) in this same zone, but with an epicenter closer to the Portuguese coast, around 100 kilometers in the south-west of the Cape St. Vincent. In these two events, no damages were recorded and the maximum intensity of V was reported in some region of Algarve.
Another important earthquake is the 29th of July 2003 earthquake that occurred at 05:31 a.m. The instrumental magnitude of this event is Mw=5..3 (Pro et al., 2012).

South margin of Portugal

In the band that extends from the SE of the Cape St. Vincent until the area of the strait of Gibraltar, a large concentration of events that highlights several alignments. From these events, two have a larger magnitude: the 15th of March 1964 earthquake (M = 6.2) and the 14th of July 1972 event (M = 5.2).

3.3.2. Focal mechanisms

According to the importance that the knowledge of the seismic sources plays in the characterization of the movement of the seismogenic faults and their relevance in the elaboration of a seismotectonic model, allowing understanding the geodynamic of the region, we attended to increase of the number of studies of this domain in this region. This work was made difficult by the low to moderate seismicity and the poor distribution of the seismic network. The local seismic network allows the record of a larger number of data and decreases the minimum magnitude threshold from which the calculation of a focal mechanism is possible. From these local networks, the “transfrontier” (Instituto Português do Mar e da Atmosfera, ex IM) is composed by 7 stations with short period sensors, which were used in the Algarve region between 1996 and 2003. The network of the University of Évora is constituted by 4 stations with short period seismometers, in activity in the region of Évora between 1998 and 2000. The network of the project “Tomografia sísmica da Litosfera Continental Algarvia” was composed by 30 short period stations and was deployed in Algarve and in the lower Alentejo during all the year of 2006. Some examples of studies using the data provided by such seismic network are presented in the publications of Bezzeghoud et al. (2000) and of Carrilho et al. (2004) (“transfrontier” network); Borges (2003) (Évora network).

Many authors have studied the focal mechanisms in this region (Moreira 1985, 1991; Fonseca and Long 1991, Borges 1991, 1996, 2003; Borges et al. (2001); Stich et al. 2003; Buforn et al. 2004; Carrilho 2005; Stich et al. 2005; Grandin et al. 2007B; Bezzeghoud and Caldeira, 2012; Pro et al., 2012). According to the mechanisms calculated in these studies, together with other stress markers,

a more accurate estimation of the stress and strain fields was achieved for the Portugal mainland and its adjacent regions.

Globally, the distribution of the focal mechanisms, calculated from earthquakes that occurred in the Portugal mainland and the adjacent Atlantic margin, shows a large heterogeneity. In the figures 3.4 and 3.5, 45 focal mechanisms are represented, corresponding to earthquakes ($1.9 \leq M \leq 8.0$) that occurred during the period 1960-2009. The focal mechanism solutions present here are compiled from the different publications (Bezzeghoud et al., 2012). This compilation allows us to analyze the set of focal mechanisms and to give a standard focal mechanism for the entire examined area. A general look on figure 3.4 and 3.5 shows that predominant type of focal mechanisms are strike-slip, reverse or oblique. A detailed analysis allows us to distinguish and characterize five sub-regions (figure 3.4): the west Portuguese margin - A1; Lisbon and Tagus Valley – A2; Évora and adjacent regions - A3; Algarve band – A4; inter-plate zone – A5.

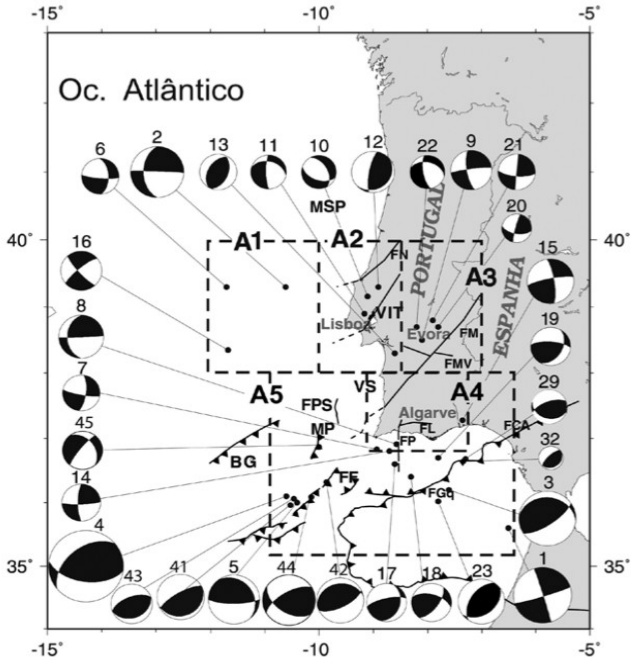

Figure 3.4: focal mechanisms of the Portugal mainland and its adjacent margins. From Bezzeghoud et al. (2012) (see text for more details).

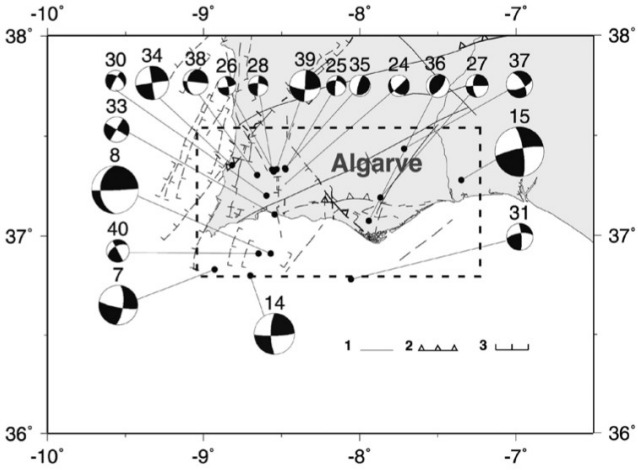

Figure 3.5: Details of the Algarve band, represented in the figure 2.4 (A4). 1 – geological lineament, 2 – Normal faults, 3 – Reverse faults. Figure from Bezzeghoud et al. (2012). Active faults from Cabral and Ribeiro (1988).

The west Portuguese margin - A1

The west Portuguese margin presents small number of focal mechanisms but all of them are strike-slip (figure 2.4, A1); the events 2 and 6 present a fault plane oriented N-S and E-W and the event 16 presents planes in the directions NW-SE and NE-SW. The first ones may be associated to the extension of the Nazaré fault and the event 16 may be related to the extension of the fault system of the Low Tagus Valley. According to this assumption, for the events 2 and 6 the movement may be toward the direction E-W and the mechanism 16 may result of the unequal dextral movement, but in the direction NE-SW. According to Roque et al. (2009), the morphology of the submerged area presented by "Tore Seamount" and the Egas Moniz crests, which connect with the Promontory of Extremadura, is controlled by reverse faults and backthrusts in the E-W direction, showing evidences of activity during the late Pliocene-Pleistocene.

Lisbon and Tagus Valley - A2

In the north of Lisbon and of the Tagus River, near the coast, there are two events (10 and 11) with normal fault mechanisms; in south (event 13, near the Sado Valley) and in north of these events (event 12) were calculated mechanisms of reverse fault with planes oriented towards the NNE-SSW direction (figure 2.4, A2). These recent events seem to be associated with faults mapped and marked in the neotectonic map (Cabral & Ribeiro, 1988). The event 11 may be associated with a set of faults oriented NNE-SSW and the event 13 with the extension to the north of the Deixa-o-Resto fault (Ribeiro et al., 1996). This relation should not be viewed categorically due to imprecision in the locations.

Évora region and adjacent regions - A3

The earthquakes 9, 20 and 21 are located near the city of Évora and all of them present a strike-slip movement with planes oriented in NS and EW direction (figure 2.4, A3). Despite the alignment of epicenters in the N-S direction, in agreement with the planes of the mechanisms (Borges et al., 2001), no faults are known with the orientation of the mechanism planes. The event (22), was generated in oblique normal fault oriented NW-SE, parallel to the maximum horizontal compression, unlike the mechanisms of the region that are strike-slip. One possible explanation may be the proximity of the event to the Lower Tagus-Sado basin. The adjustments of the crust, in depth, related to the phenomena of subsidence of this basin may be the origin of this earthquake.

The Algarve band - A4

The southern region of Portugal and its immediate coastal margin is dominated by mechanisms of strike-slipe type (events 7, 8, 14, 15, 24-28, 30, 31, 33, 34, 37-40) with planes oriented in directions NS and EW. Exceptions are events 35 and 36, which are of reverse type (figure 2.4 and 2.5 - A4). Despite the weak magnitude of most events ($1.9 \leq M \leq 3.7$), its mechanisms can be considered representative of the general tendency of the regional direction of maximum compression (NW-SE) in the Algarve because, 1) a number of events (17) which have the same tendency is significant; 2) these events of low magnitude have a tendency similar to the events 7, 8, 14 and 15 of larger magnitude ($4.3 \leq M \leq 5.0$) which are located in the vicinity and 3) the spatial distribution of these events covers almost all Algarve (figure 2.5). This result confirms the tectonic model for the Algarve basin proposed by Terrinha (1998) and confirmed by Borges et al. (2001), with the focal

mechanisms of this zone.
In this model, composed by four strike-slip faults with an orientation between N-S to NNW-SSE, is included the hypothetical Guadiana fault, which, according to Terrinha (1998), should be associated with the Huelva event (event 15) of the 20th of December 1989 and not with the extension of the Loulé fault as proposed by Mezcua and Rueda (1997). The event 1 may also be related to the oceanic extension of this fault. The remaining events (7, 8, and 14) would also be explained by the model described above. This interpretation may be further enhanced by the fact that the faults of the Algarve margin are oriented approximately N-S. In this context, we can consider that the mechanisms of the Algarve band and its adjacent margin are the result of sinistral strike-slip movement developed by faults oriented approximately N-S.

The inter-plate zone -A5

Further to the south, closer to the boundary of the Eurasian and the Nubian plates, a set of earthquakes (3, 4, 5, 17, 18, 19, 23, 29, 32, 41, 43 and 44) present a notable homogeneity in terms of focal mechanisms (figure 2.4, A5). All of them are reverse mechanisms with a weak strike-slip component. These events may be associated to a fault system of average orientation E-W, resulting from the collision between the Eurasian and Nubian plates.

3.4 Conclusion

The seismicity of Portugal is considered as moderate, due to its geographic proximity to an active region, which stretches from Gibraltar to the Azores and constitutes the boundary of two plates: the Eurasian plate and the Nubian plate.
The study of the seismicity of Portugal may be divided into three different zones, according to the seismicity features, the morphologic and tectonic structures and the geodynamic behavior (Bezzeghoud et al., 2012). The occidental part corresponds to the archipelago of Azores and extends to the mid-Atlantic ridge. The central part is related to the Glória fault, incorporating the archipelago of Madeira. The oriental part includes the Portugal mainland and its margins.
Concerning the Portugal mainland, the largest magnitudes occurred in the Tagus Valley in 1344, 1531 and 1909 (Benavente events) and in the south-west of the Cape Saint Vincent in 1755 (Lisbon earthquake) and 1969.
The distribution of the focal mechanisms shows a large heterogeneity in the Portugal mainland. A detailed analysis allows distinguishing five sub-regions (figure 3.4 and 3.5): 1) the west Portuguese margin, dominated by strike-slip mechanisms; 2) the Lisbon and Tagus valley, that present mechanisms of normal and reverse faults; 3) the Évora region with strike-slip movement; 4) the Algarve band, dominated by strike-slip mechanisms; and 5) the inter-plate zone with reverse mechanisms.

CHAPTER 4

Towards a Bayesian seismotectonic zoning

4.1. Introduction

Several studies have shown the determinant impact of seismotectonic zoning in Probabilistic Seismic Hazard Assessment (PSHA) (Beauval, 2003; Beauval and Scotti, 2004; Bender, 1986; Le Goff et al., 2009; Woo, 1996). The seismotectonic zoning allows linking the seismicity with the tectonically-active geological structures, in order to define sources for use in PSHA computation. Usually, and because faults are often not characterized well-enough, source zones are defined as surfaces and modeled as polygons. In that case, they are delimited with fixed, infinitely thin boundaries. In each zone, the geological expression of active tectonics and the seismicity are deemed homogeneous (e.g., focal depths and mechanisms, seismicity rate, and maximum magnitude), and each point of a zone is considered an equally likely source of earthquake.

Besides the lack of data (e.g., short period of instrumental observation of small events, short catalog of large events, blind faults), the establishment of a traditional seismotectonic zoning generates different shortcomings. The finite boundaries of the different zones are set by expert decisions, leading to different problems : 1) the superposition of a resulting hazard map with areal source zoning model underlines the large sensitivity of the results to this method (Beauval, 2003); 2) the seismotectonic zoning is not reproducible: different experts come up with different zonings using the same input data. 3) the final seismotectonic zoning is not provided with error maps reflecting the original density of information used for both the assessment of the common characteristics and the calculation of seismicity rates of each zone and 4) the zoning does not account for any variation in faulting mechanisms with depth or for conjugate sets of faults.

Some approaches, such as statistical region partitioning (Weatherhill and Burton, 2009), strive to resolve these shortcomings but are still not satisfying, because of their lack of robustness and the fact that, at best, only the seismic catalogs and the focal mechanisms are used. They proposed an approach of partitioning with K-means algorithms. It consists in partitioning regions from the location of observed seismicity. This method is reproducible, considering that the initial cluster centroids are the same, and they underline the problems of the seismotectonic zoning. However, the K-means method has problems determining the optimal number of clusters and the initial cluster centers, and may lead to a local optimum instead of a global optimum partition. Moreover, this approach does not use geologic and seismotectonic data. This practice is not consistent with a seismotectonic zoning. Indeed, two hypocenters may be close to the mean cluster position and possess completely opposite geologic and seismotectonic features. The location of seismic event hypocenters is not an exclusive factor for seismotectonic zoning assessment.

In order to avoid the abrupt change in the seismicity rate at source zone boundaries, observable in the resulting hazard map, Bender (1986) proposes to use a standard "hard" seismotectonic zoning but to provide a smoothing using the epicenter location uncertainty, considered normally distributed. A point source will contribute to the seismicity rate calculation of several zones, according to its epicentral location uncertainty. The assumption on the location uncertainty characterization, arbitrary defined by 0, 10, 25 and 50 kilometers, is questionable. The actual location uncertainty is related to each seismic event. The value of 50 km is considered for historical earthquake and cannot reflect the uncertainty of an instrumental seismic event. Instrumental seismic event uncertainty depends on its location (compared to the seismic network) and its date (improvement of seismic station accuracy and network density). Each event has different uncertainties, according to their position relatively to the seismic stations, the number of instrumental records or the number of felt intensity points.

Wesson and al. (2003) propose a methodology, based on Bayesian inference, to associate

earthquakes and faults. This method may be interesting as far as the seismicity rate calculation is concerned. A restricting factor is the requirement of exhaustive data (e.g., slip rates of recognized faults), limiting this application to regions where the velocity of plate tectonics is high.

This study aims to propose an exploratory study for alternative procedures in area source modeling. We search to obtain a method which will be robust and reproducible. In this way, we strive to combine different data using Bayesian methods.
We start to develop a generative model with two zones, characterized by two different surface activity rates, creating synthetic catalogs drawn from a Poisson distribution as occurrence model, a truncated Gutenberg-Richter law as magnitude-frequency relationship and a uniform spatial distribution.

4.2. Input data

Different data sets are traditionally used in order to establish a seismotectonic zoning. These data are of different kinds and are characterized by different dimensions. The structural geology map contains much information about faults (e.g., fault orientations, fault geometry, fault type, tectonic ensembles) and has an important role in the development of seismotectonic zoning.

Two different seismicity catalogs are used in seismotectonic zoning computations: historical and instrumental. The idea is 1) to locate the hypocenters and 2) to compute the focal mechanisms and magnitudes to try and image active faults and characterize the type of faulting (strike-slip, or dip-slip faulting). The historical catalog is built by collecting stories/reports of subjective experiences (was the shaking enough to wake people up, did the building sway, questionnaires can be found in online forms from seismological surveys around the world, e.g., Did you feel it?, U.S. Geological Survey, or BCSF), observations of damages to buildings and perturbations to the landscape (liquefaction, stream offsets, etc) observed after an earthquake.

These observations allow assessing an intensity of the seismic event in a predefined scale (e.g., MMI, EMS-98). Intensities are subjective measures by definition. The data points (density and location) depend namely on the distribution of the population at the time of the earthquake. They are used to assess the size and depth of the events and to try and allocate the event to known active faults. Small or deep events are not likely to be represented in historical catalogs. Depending on the history of a region, it may cover 200 years (since the Gold Rush in California for example) or 2000 years (in the Middle East). The instrumental catalog is obtained from seismic signals, recorded by seismic networks. The density of the network will affect directly the quality of the localization of the source and size of the events. Different magnitude scales exist to quantify the energy released by an earthquake. These catalogs contain uncertainties, notably in hypocenter locations and magnitude calculations, and the systematic errors (round-off). Because the evolution of seismic networks is recent (the first dense networks in Europe were dedicated to "listening" to nuclear tests by other countries, e.g., the LDG in France, since 1960), the period of instrumental observation of small events is short.

Other data are useful in the conception of seismotectonic zoning in order to have a better constrained model. Indirectly, geological maps, expressing the age of the formations, trenches, geophysical data and digital elevation model (DEM) allow improving the location of faults. An example of such composite data sets is shown in figure 4.1.
In conclusion, we have 2D maps with features such as 1D fault lines, or dip angles; 3D points (hypocenters resulting from the inversion of seismograms), points on a surface with intensity data;

borehole or seismic transects intersecting faults.

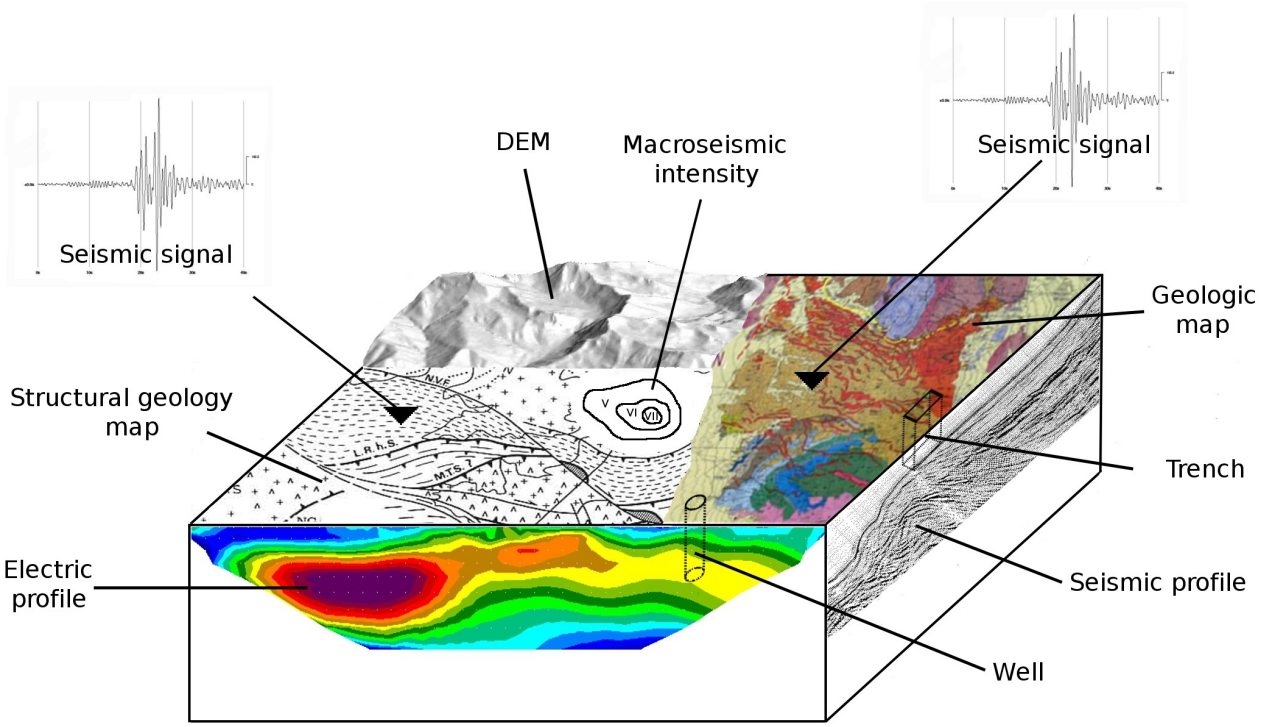

Figure 4.1: 3D diagram representing the useful data for using in PSHA. In this figure, the segmentation is done to show the kinds of data and do not express a seismotectonic zoning (from Le Goff et al., 2010)

4.3. Bayesian methodology reminders

4.3.1. Bayesian methods

The Bayesian method consists in calculating the plausibility of a hypothesis. This model allows linking the data to the parameters, according to predefined priors. Its computation is derived from the Bayes' theorem. This step is a key feature of Bayesian statistics, in which Bayes' theorem synthesizes the two separate sources of information (priors and data). The result of combining the prior information and the data is the posterior distribution. This resulting posterior distribution is, then, used to derive inferences about the parameters. In a Bayesian sense, a probability may be interpreted as a numerical translation of a degree of belief.
The Bayesian interpretation of probabilities provides a consistent framework for the quantification of uncertainty (Bishop, 2007). Uncertainties are present into the observed variables but also into the unknown values of latent variables and model parameters. Using Bayesian methods allow dealing with all sources of uncertainty. Usually, it involves no more than the systematic application of the sum rule (3.1) and the product rule (3.2) of probability.

$$p(X)=\sum_{Y} p(X,Y) \tag{4.1}$$

$$p(X,Y)=p(Y|X)\,p(X) \tag{4.2}$$

Here X and Y are random variables, p(X,Y) is the joint probability and is verbalized as “the

probability of X and Y". Similarly, the quantity p(Y|X) is a conditional probability and is verbalized as "the probability of Y given X", whereas the quantity p(X) is a marginal probability and is simply "the probability of X".
If we consider a model developed with a set of parameters, grouped into a vector w, and we denote the training data set by D, then a central quantity is the conditional probability distribution p(D|w). When viewed as a function of w this is known as the likelihood function, and it plays a central role both in conventional (frequentist) and Bayesian approaches. In a frequentist setting the goal is to find an estimator w^* for the parameter vector by optimizing some criterion, for example by maximizing the likelihood. A significant problem with such approaches is over-fitting whereby the parameters are tuned to the noise on the data, thereby degrading the generalization performance.
In a Bayesian setting, we express the uncertainty in the value of w through a probability distribution p(w). This captures everything that is known about the value of w, aside from the information provided by the training data, and is usually known as the prior distribution. The contribution from the training data is expressed through the likelihood function, and this can be combined with the prior using Bayes' theorem to give the posterior distribution. From the product rule, together with the symmetry property p(X,Y)=p(Y,X), we obtain the Bayes' theorem:

$$p(w|D)=\frac{p(D|w)\,p(w)}{p(D)} \tag{4.3}$$

Here the denominator is given (using the sum rule) by

$$p(D)=\int p(D|w)\,p(w)\,dw \tag{4.4}$$

and can be viewed as the normalization factor which ensures that the posterior distribution p(w|D) in (Y) integrates to one. It also plays a central role in model selection.

One other important advantage of using Bayesian methods is the possibility of updating the posterior probability when new data are available.

4.3.2. Graphical models

The use of Bayesian methods amounts to a consistent application of the sum and product rules of probability. We can therefore proceed to formulate and solve complicated probabilistic models purely by algebraic manipulation. However, it is highly advantageous to augment the analysis using diagrammatic representations of probability distributions, called probabilistic graphical models. These offer several useful properties:

1. They provide a simple way to visualize the structure of a probabilistic model and can be used to design and motivate new models.

2. Insights into the properties of the model can be obtained by inspection of the graph.

3. Complex computations, required to perform inference and learning in sophisticated models, can be expressed in terms of graphical manipulations, in which underlying mathematical expressions are carried along implicitly.

A graph comprises nodes connected by links. In a probabilistic graphical model, each node represents a random variable (or group of random variables), and the links express probabilistic

relationships between these variables.
There are two main types of graphical model in widespread use, corresponding to directed graphs (in which the links have a directionality indicated by arrows) and undirected graphs (in which the links are symmetrical). In both cases the graph expresses the way in which the joint distribution, over all of the random variables, can be decomposed into a product of factors each depending only on a subset of the variables, but the relationship between the graph and the factorization is different for the two types of graph.
Consider first the case of directed graphs, also known as Bayesian networks or belief networks. An example is shown in figure 3.2. If there is a link going from a node A to a node B, then we say that the node A is the parent of the node B. The nodes without incoming links are prior probability density functions (pdfs). They represent what we assume to be known before starting the Bayesian inference process. The graph specifies that the joint distribution factorizes into a product over all nodes of a conditional distribution for the variables at that node conditioned on the states of its parents:

$$p(x)=\prod_{k=1}^{K} p(x_k|pa_k) \tag{4.5}$$

where pa_k denotes the set of parents of x_k, and $x=\{x_1,...,x_K\}$. For the specific case shown in figure 4.2, the factorization takes the form:

$$p(x_1)\,p(x_2)\,p(x_3)\,p(x_4|x_1,x_2,x_3)\,p(x_5|x_1,x_3)\,p(x_6|x_4)\,p(x_7|x_4,x_5) \tag{4.6}$$

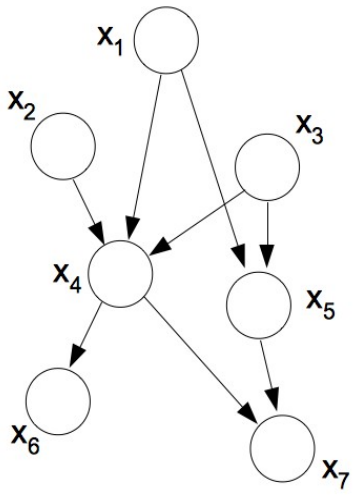

Figure 4.2: Example of a directed graph

A specific, and very familiar, example of a directed graph is the hidden Markov model, which is widely used in speech recognition, handwriting recognition, DNA analysis, and other sequential data applications, and is shown in figure 4.3. The joint distribution of this model is given by:

$$p(x_1,\ldots,x_N,z_1,\ldots,z_N)=p(z_1)\left[\prod_{n=2}^{N} p(z_n|z_{n-1})\right]\prod_{n=1}^{N} p(x_n|z_n) \tag{4.7}$$

Here $x_1, \ldots, x_N$ represent the observed variables (i.e. the data). In a graphical model the observed variables are denoted by shading the corresponding notes. The variables $z_1, \ldots, z_N$ represent latent (or hidden) variables which are not directly observed but which play a key role in the formulation of the model. In the case of the hidden Markov model, the latent variables are discrete, while the observed variables may be discrete or continuous according to the particular application.
Many other models can easily be constructed in this way. The key point is that new models can be formulated simply by drawing the corresponding graphical model, and prior knowledge from the application domain can be expressed through the structure of the graph. In particular, missing links in the graph determine the conditional independence properties of the joint distribution.

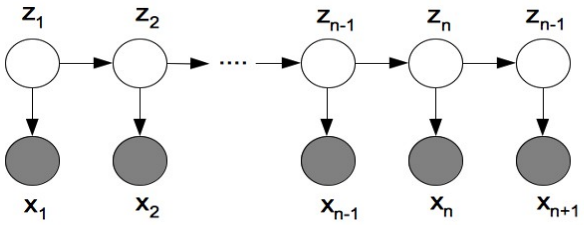

Figure 4.3: Directed graph corresponding to hidden Markov model

The second major class of graphical model is based on undirected graphs. A well-known example is the Markov random field. This graphical structure can be used to solve image processing problems such as denoising and segmentation.
As with directed graphs, an undirected graph specifies the way in which the joint distribution of all variables in the model factorizes into a product of factors each involving only a subset of the variables.
In order to simplify and because no undirected graphs were used in this study, these undirected graphical models will not be developed in this chapter.

Directed and undirected graphs together allow most models of practical interest to be constructed. Which type of graph is more appropriate will depend on the application. Generally speaking, directed graphs are good at expressing causal relationships between variables.

4.3.3. Inference

Once we have formulated a model in terms of a probabilistic graph, we need to learn the parameters of the model and to use the trained model to make predictions. Some of the nodes in the graph correspond to observed variables representing the training data, and we are interested in finding the posterior distribution of other nodes, representing variables whose value we wish to predict, conditioned on the training data. This refers to inference problem. The remaining nodes in the graph represent other latent, or hidden, variables whose values we are not directly interested in.
In a Bayesian setting, the model parameters are also random variables and are therefore represented as nodes in the graph. In the graph of figure 4.4, the black arrows represent the generative model (direct sense), while the red arrow expresses the Bayesian inference (inverse sense).
First we need to define the priors of the model. Since the priors represent the state of knowledge of random variables, before the use of data, we have an idea of the probability density functions (pdfs) to use to define the priors. Then the joint pdf is computed. The joint pdf is the product of all priors and conditional pdfs according to the graphical model. Finally, the goal of the inference is to obtain the best parameters for the model and the data set. So, the objective is to find the parameter values

that maximize the posterior pdf. According to Bayes' theorem, the posterior pdf is proportional to the joint probability. So, obtaining the parameter values that maximize the posterior pdf is equivalent to maximizing the joint probability. This is called Bayesian estimation.
Bayesian methods have already been used in seismology, to analyse the dependence between interevent time and size of earthquakes (Agostinelli and Rotondi, 2001), to associate events to faults (Wesson et al., 2003), to define a ground motion model (Kuehn et al., 2011) or in the definition of recurrence models (Fitzenz et al., 2010).

4.4. Seismic zoning

In most of study areas, where the seismicity is relatively low and where other sources of information (e.g., geology, tectonics, geomorphology) are not available or not constrained well enough, a seismic zoning is used in PSHA calculation instead of a seismotectonic zoning (Vilanova and Fonseca, 2007). So, we decide to start with the achievement of a seismic zoning. The only required data is a complete seismicity catalog. In this study, Bayesian methods are used in order to define a generative model, according to the graphical model. A model of two zones, differentiated by two activity surface rates, will be generated. Then, this model will be inverted (inference) to obtain the posterior probability of the target variables, which are, in this case, the seismic activity rates of each zone and the limit between the 2 zones. In order to control the input data and to have an idea on the expected results, a synthetic catalog will be generated.

Several inference calculations will be achieved, using different synthetic realizations of catalogs, in order to test the resolving power of this method in a controlled case, where the input parameters, both temporal and spatial occurrence models are known.

4.4.1 Graphical model

As explained before (paragraph 4.3.2.), the graphical model constitutes a guide to define the joint probability. The black arrows show the generative model or direct model while the red ones express the inference model (Figure 4.4).
In this graphical model, for the j^{th} zone, the seismicity rate is generated from the surface seismicity rate and the size of the zone, which depends on the limit between the two zones. Then, this seismicity rate is coupled to a Poisson model to determine the different times of events. The seismicity rate and the observation period allow defining the occurrence number of earthquakes I in the zone j. The limit between the two zones is also used to obtain the different locations of the I^j events, drawn in a uniform spatial distribution. Both times and locations are used to generate the synthetic catalog. The inference will provide the joint probability of the model and, after marginalization, will provide the optimal value for the location of the limit between the two zones and the surface seismicity rate in each zone.

4.4.2 Synthetic catalog

The synthetic catalogs are computed using the usual models, even if some of them are questionable. So far, our study is focused on the seismic zoning problem and not on the models used to define the characteristics of each zones. So, the catalogs are achieved from a Poisson model as temporal model, from a uniform spatial model and from the truncated Gutenberg-Richter law for the magnitude distribution. A description of the Matlab code, used to compute the synthetic catalogs, is

given in the chapter 8.

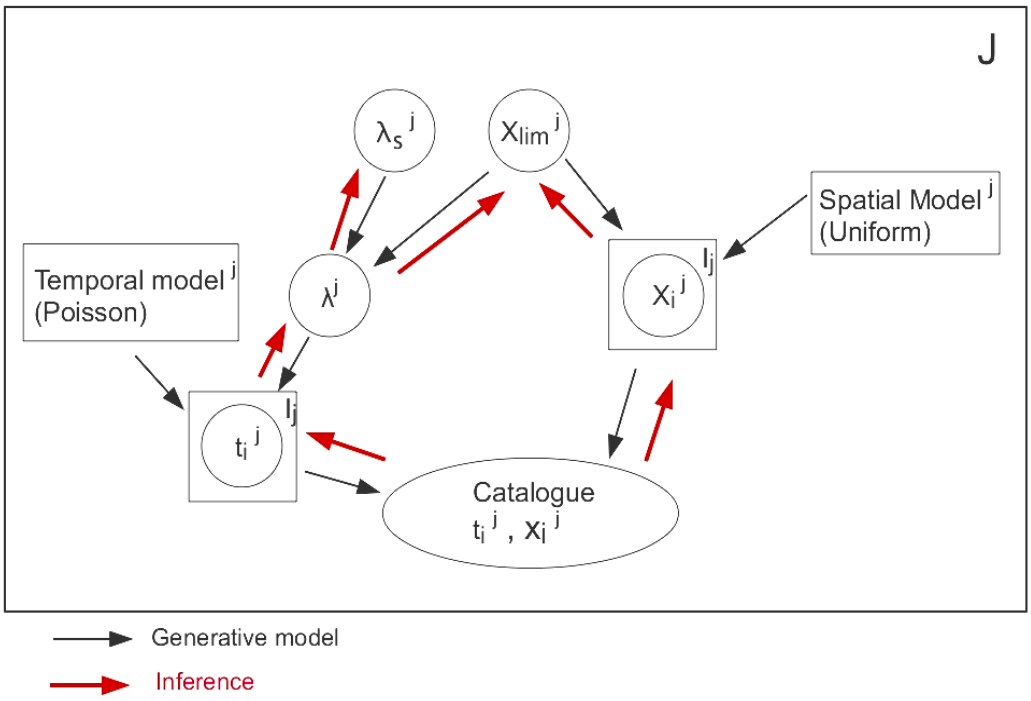

Figure 4.4: Graphical model for generating synthetic catalogs. Black arrows represent the causal relationships of the direct model. The red arrow represents the inference, which allows estimating the limit between geographic zones and their seismic activity rate. More details in paragraph 4.4.1.

4.4.2.1 Temporal repartition of the events

Even though the Poissonian model is often discussed (Zöller et al., 2007; Kuehn et al., 2008; Fitzenz et al., 2010), this distribution is generally considered to model the distribution of inter-event times for earthquakes in a large region, regardless of their magnitude. This model implies that the probability of occurrence of an earthquake does not depend on the elapsed time since the last earthquake. The events are then considered independent one another, supposing that there are neither foreshocks, aftershocks, nor triggered events. The cumulative distribution function (cdf) of the Poisson law, expressing the probability to have at least one event in the time interval Δt, is defined as follow:

$$F(\Delta t) = 1 - e^{-\lambda \Delta t} \tag{4.8}$$

Δt represents the time interval between two events and λ is the seismic activity rate.

The seismic activity rate, λ, is generated from the surface seismicity rate of the j^{th} zone and the limit between the 2 zones. The repartition of the different times of the events follows this algorithm:

1. First a random number, r, is drawn from a uniform distribution in the interval [0,1].
2. This random number, r, is associated to the probability value of the Poisson cdf.
3. The inter-event time, that will relate the time of occurrence of the new event to the last event in

the catalog, is obtain with the corresponding value of the theoretical Poisson cdf.
4. The catalog is updated with the time of the new event.
5. Back to step 1, for the next event, until the elapsed time reaches a given observation time T_{obs}.
For the j^{th} zone, the sampling of the Poisson law (Figure 4.5) provides the times of the different events, t^j_i the number of events, I^j, during the given observation time T_{obs} and according to the seismic activity rate, λ^j .

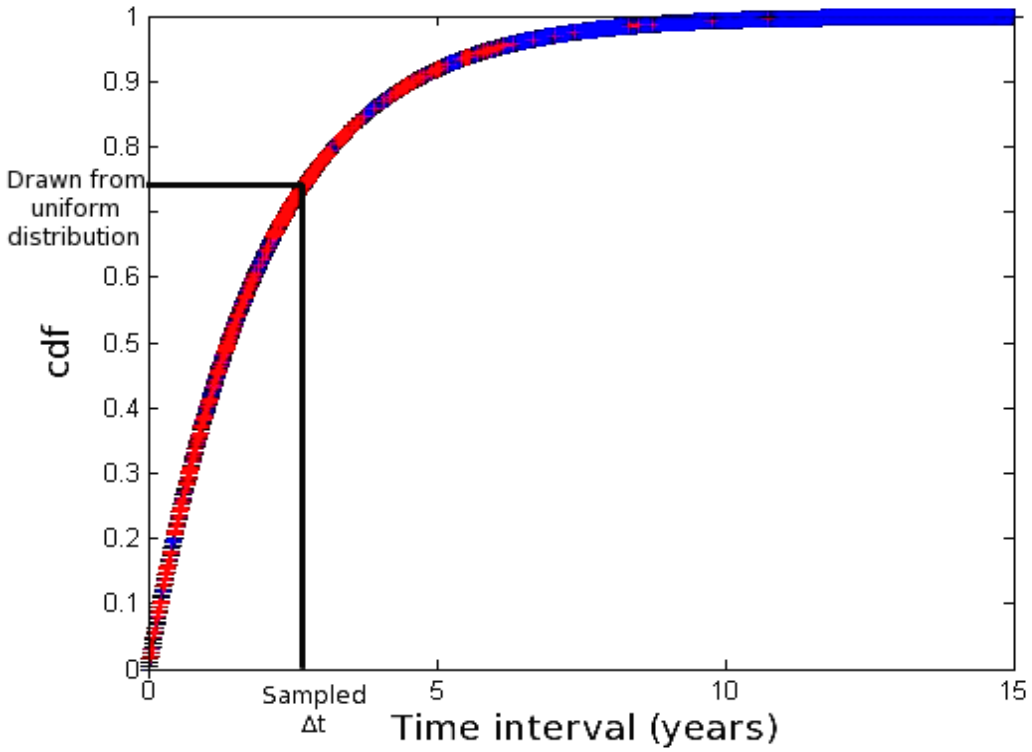

Figure 4.5: Sampling of the time intervals from the Poisson law. In red: samples of the time intervals; In blue: Theoretical cumulative distribution function of the Poisson law

4.4.2.2 Spatial distribution of the events

In PSHA, the uniform spatial model is usually used into a source zone. This source zones are then considered as homogeneous, implying that an event may occur anywhere within the zone. This assumption implies that a part of a zone, with a low seismic activity in reality, may be modeled as allowing the presence of a large number of earthquakes with large magnitudes (Musson, 2004). Moreover, with few data, some events may appear to line-up and be considered as tectonic structures. In such a case, it is difficult to differentiate a zone with a sparse seismicity (background seismicity) from a zone with a seismicity associated to tectonic structures.

To begin with a simple case, the uniform spatial model was simulated. For each event i of the j^{th} zone, a random number is drawn from a uniform distribution in the interval [0,1]. Then, this number is multiplied by the dimension of the zone along the x-axis. The same calculation is achieved along the y-axis, and we obtain the location (x,y) of the events (Figure 4.6). To obtain a good location of the events, the random number drawn needs to have a good accuracy to avoid rounding errors.

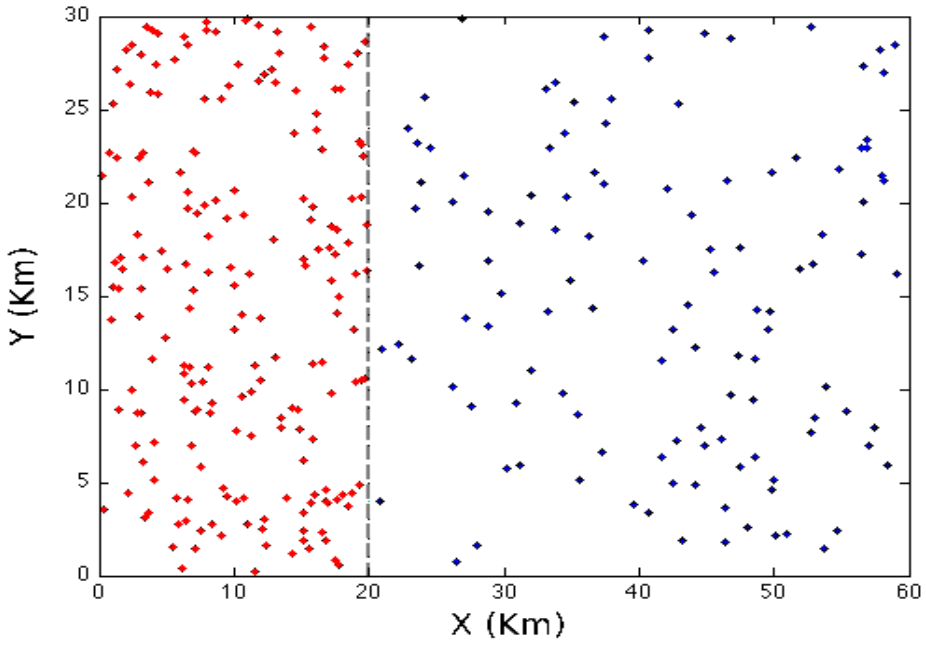

Figure 4.6: Uniform spatial repartition of the events into the two zones. In red: events of the 1th zone; In blue: events of the 2nd zone

4.4.2.3. Magnitude-frequency relationship

The chosen frequency-magnitude model is the truncated exponential model. It expresses the fact that the proportion of larger earthquakes compared to smaller ones is linear over the whole size range encountered in a region, until a roll-over for magnitudes close to the maximum magnitude. It provides, for a given magnitude M, the annual number of event, λ, of magnitude larger or equal to M. This relationship may be express as follow:

$$\lambda = \lambda_{min} \frac{e^{-\beta(M-M_{min})} - e^{-\beta(M_{max}-M_{min})}}{1 - e^{-\beta(M_{max}-M_{min})}} \tag{4.9}$$

Here, λ denotes the annual number of events with magnitude larger than M. λ_{min} expresses the annual number of events with magnitude larger than M_{min}. M_{min} is the minimal magnitude considered in the study and M_{max} is the magnitude of the Maximum Credible Earthquake (MCE) considered in the zone. β corresponds to the coefficient of the exponential decrease.

The different magnitudes are generated from the seismic activity rate, λ, and attributed to each event i of the J zones. The attribution of the different magnitudes follows almost the same algorithm than the one defined for the time distribution of the events:

1. First a random number, r, is drawn from a uniform distribution, in the interval [0,1]
2. This random number, r, is associated to the probability value of the truncated exponential cdf.
3. The magnitude of the event is obtained with the corresponding value of the theoretical truncated exponential cdf.
4. Back to step 1, for the next event.

According to the sampling (Figure 4.7), the samples may present a more or less good fit with the theoretical magnitude-frequency law (Figure 4.8), and the extrapolation of the b-values and the maximum magnitude from a catalog realization may lead to a large variability (Page, 2011).

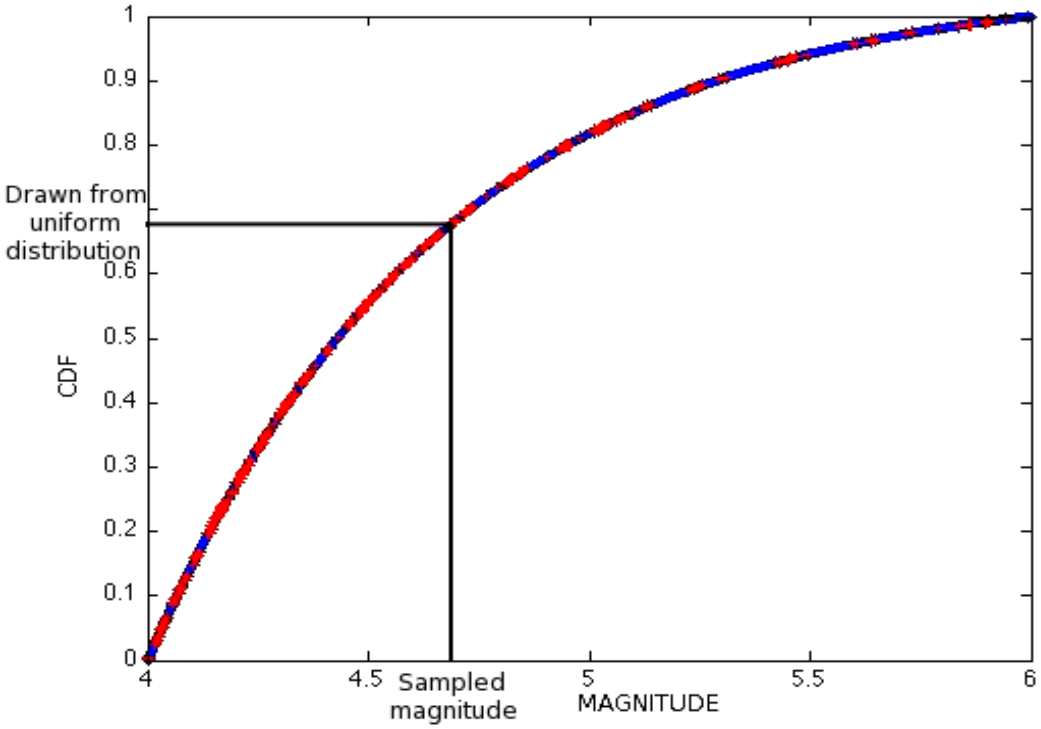

Figure 4.7: Sampling of the magnitudes from the truncated Gutenberg-Richter law. In blue: Theoretical cumulative distribution function of the truncated Gutenberg-Richter law; in red: samples of magnitudes

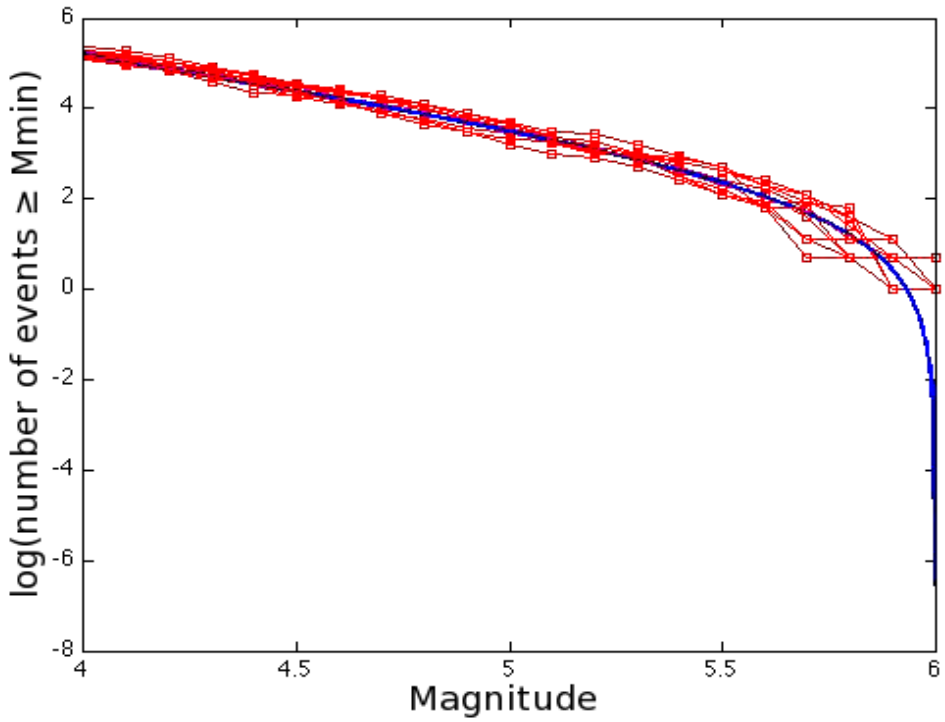

Figure 4.8: Magnitude-frequency law. In blue: Theoretical truncated Gutenberg-Richter law; In red: number of samples drawn by magnitude intervals, for 10 realizations of synthetic catalogs.

4.4.3. Bayesian inference

In this case study, the inference allows, from the synthetic catalog, recovering the pdf for initial parameters. A first step is the definition of priors, expressing the degree of belief about a random variable before taking into account the data. Then the method consists in evaluating the posterior probability of the model. According to Bayes' theorem, the posterior probability is proportional to the joint probability and one can determine the optimal value of the parameters and also the covariance matrix. The joint probability expresses the relationship between all the elements of the model. If the number of zones, J, is fixed, the joint probability may be expressed as follow:

$$P_j = P\left(\lambda_S^j, x_{limit}, \lambda^j, t_i^j, (\vec{x}_i)^j, Spat.Mod^j, Temp.Mod^j\right) \tag{4.10}$$

Here, λ_S^j denotes the surface activity rate of the j^{th} zone while λ^j is the activity rate of the j^{th} zone. x_{limit} represents the limit between the 2 zones. t_i^j is the elapsed time between two events. $(\vec{x}_i)^j$ is the vector location of the i^{th} event into the j^{th} zone. $Spat.Mod^j$ and $Temp.Mod^j$ represent, respectively, the spatial model (uniform in this case) and the temporal model (Poisson) for the j^{th} zone. The graphical model specifies that the joint distribution factorizes into a product over all nodes of a conditional distribution for the variables at that node conditioned on the states of its parents:

$$P_j = \prod_{j=1}^{J} P_r \; P(\lambda^j | \lambda_S^j, x_{limit}) \; P(t_i^j | t_{i-1}^j, \lambda^j, Temp.Mod^j) \; P(x_i^j | x_{limit}, Spat.Mod^j) \; P(y_i^j | Spat.Mod^j) \tag{4.11}$$

where P_r represents the priors and may be expressed as follow:

$$P_r = P(\lambda_S^j) \; P(x_{limit}) \; P(Spat.Mod^j) \; P(Temp.Mod^j) \tag{4.12}$$

To simplify, we decided that both spatial and temporal models are known and may be approximated to a Dirac distribution. Because there are more variables than the data and the parameters we want to infer, we need to integrate the joint pdf over all possible values of the variables we are not interested in. This called a marginalization step.
First we decide to marginalize with respect to λ, giving:

$$P\left(\lambda_S^j, x_{limit}, t_i^j, (\vec{x}_i)^j, Spat.Mod^j, Temp.Mod^j\right) = \int P_j \, d\lambda^j \tag{4.13}$$

Then, we assume that the pdf $P(\lambda^j \mid \lambda_S^j, x_{limit})$ is simply the Dirac distribution $\delta(\lambda^j - f(\lambda_S^j, x_{limit}, Ly_{max}))$, where Ly_{max} represents the upper limit in the y-axis. Also to simplify the calculation, the prior distributions are considered as uniform. So we can write them as follow:

$$P(\lambda_S^j) = \frac{1}{\lambda_{S,max}^j - \lambda_{S,min}^j} \tag{3.14}$$

and

$$P(x_{limit}) = \frac{1}{Lx_{max}} \tag{4.15}$$

Here, $\lambda^j_{S,max}$ denotes the maximum surface activity rate used in the study while $\lambda^j_{S,min}$ is the minimum one. Lx_{max} expresses the upper limit possible in the x-axis.
In this study case, we generated a model with two zones (J=2). So we obtain for the prior distribution:

$$P_r = P(\lambda_S^1)\ P(\lambda_2^S)\ P(x_{limit}) = \left(\frac{1}{\lambda^1_{S,max} - \lambda^1_{S,min}}\right)\left(\frac{1}{\lambda^2_{S,max} - \lambda^2_{S,min}}\right)\left(\frac{1}{Lx_{max}}\right) \quad (4.16)$$

The joint pdf of this model is

$$P_j = P_r \prod_{i=1}^{I_1} \lambda_S^1 e^{-\lambda_S^1 x_{limit} Ly_{max}(t^1_{i+1} - t^1_i)} \prod_{i=1}^{I_2} \lambda_S^2 e^{-\lambda_S^2 (Lx_{max} - x_{limit}) Ly_{max}(t^2_{i+1} - t^2_i)} \quad (4.17)$$

and then:

$$P_j = P_r (\lambda_S^1)^{I_1} e^{-\lambda_S^1 x_{limit} Ly_{max} \sum_{i=0}^{I_1} (t^1_{i+1} - t^1_i)} (\lambda_S^2)^{I_2} e^{-\lambda_S^2 (Lx_{max} - x_{limit}) Ly_{max} \sum_{i=0}^{I_2} (t^2_{i+1} - t^2_i)} \quad (4.18)$$

If the limit between the two zones is the only parameter we are interested in, we can marginalize the joint pdf with respect to λ^1_S and λ^2_S. The resulting pdf is:

$$P_{m|\lambda^1_S, \lambda^2_S} = P_r \int \prod_{i=1}^{I_1} \lambda_S^1 e^{-\lambda_S^1 K_1 (t^1_{i+1} - t^1_i)} d\lambda_S^1 \int \prod_{i=1}^{I_2} \lambda_S^2 e^{-\lambda_S^2 K_2 (t^2_{i+1} - t^2_i)} d\lambda_S^2 \quad (4.19)$$

$$\text{with} \quad K_1 = x_{limit} Ly_{max} \quad \text{and} \quad K_2 = (Lx_{max} - x_{limit}) Ly_{max}$$

If we develop this equation, we obtain:

$$P_{m|\lambda^1_S, \lambda^2_S} = P_r \int (\lambda_S^1)^{I_1} e^{-\lambda_S^1 K_1 \sum_{i=1}^{I_1} (t^1_{i+1} - t^1_i)} d\lambda_S^1 \int (\lambda_S^2)^{I_2} e^{-\lambda_S^2 K_2 \sum_{i=1}^{I_2} (t^2_{i+1} - t^2_i)} d\lambda_S^2 \quad (4.20)$$

To resolve this equation, we apply the following variable change:

$$C_1 = \lambda_S^1 K_1 \sum_{i=1}^{I_1} (t^1_{i+1} - t^1_i) \Leftrightarrow \lambda_S^1 = \frac{C_1}{K_1 \sum_{i=1}^{I_1} (t^1_{i+1} - t^1_i)} \quad (4.21)$$

$$C_2 = \lambda_S^2 K_2 \sum_{i=1}^{I_2} (t^2_{i+1} - t^2_i) \Leftrightarrow \lambda_S^2 = \frac{C_2}{K_2 \sum_{i=1}^{I_2} (t^2_{i+1} - t^2_i)} \quad (4.22)$$

$$d\lambda_S^1 = \frac{1}{K_1 . \sum_{i=1}^{I_1} (t_{i+1}^1 - t_i^1)} dC_1 \tag{4.23}$$

$$d\lambda_S^2 = \frac{1}{K_2 . \sum_{i=1}^{I_2} (t_{i+1}^2 - t_i^2)} dC_2 \tag{4.24}$$

So, the equation is expressed as:

$$P_{m|\lambda_S^1, \lambda_S^2} = P_r \int \frac{(C_1)^{I_1}}{(K_1 . \sum_{i=1}^{I_1} (t_{i+1}^1 - t_i^1))^{I_1}} e^{-C_1} \frac{1}{K_1 \sum_{i=1}^{I_1} (t_{i+1}^1 - t_i^1)} dC_1 \int \frac{(C_2)^{I_2}}{(K_2 \sum_{i=1}^{I_2} (t_{i+1}^2 - t_i^2))^{I_2}} e^{-C_2} \frac{1}{K_2 \sum_{i=1}^{I_2} (t_{i+1}^2 - t_i^2)} dC_2 \tag{4.25}$$

Using the property of the Gamma distribution, $\Gamma(z) = \int_0^\infty t^{z-1} e^{-t} dt$, we finally obtain:

$$P_{m|\lambda_S^1, \lambda_S^2} = P_r \frac{1}{(K_1 \sum_{i=1}^{I_1} (t_{i+1}^1 - t_i^1))^{I_1}} \Gamma(I_1 + 1) \frac{1}{(K_2 \sum_{i=1}^{I_2} (t_{i+1}^2 - t_i^2))^{I_2}} \Gamma(I_2 + 1) \tag{4.26}$$

If we are interesting in the parameters λ_S^1 and λ_S^2, we can marginalize the joint pdf with respect to x_{limit}:

$$P_{m|x_{limit}} = P_r \int (\lambda_S^1)^{I_1} e^{-\lambda_S^1 Ly_{max} x_{limit} \sum_{i=1}^{I_1} (t_{i+1}^1 - t_i^1)} (\lambda_S^2)^{I_2} e^{-\lambda_S^2 Ly_{max} (Lx_{max} - x_{limit}) \sum_{i=1}^{I_2} (t_{i+1}^2 - t_i^2)} dx_{limit} \tag{4.27}$$

$$P_{m|x_{limit}} = P_r (\lambda_S^1)^{I_1} (\lambda_S^2)^{I_2} e^{-\lambda_S^2 Ly_{max} Lx_{max} \sum_{i=1}^{I_2} (t_{i+1}^2 - t_i^2)} \int_0^{Lx_{max}} e^{-a.x_{limit}} dx_{limit} \tag{4.28}$$

$$\text{with} \quad a = \lambda_S^1 Ly_{max} \sum_{i=1}^{I_1} (t_{i+1}^1 - t_i^1) - \lambda_S^2 Ly_{max} \sum_{i=1}^{I_2} (t_{i+1}^2 - t_i^2) \tag{4.29}$$

Finally we obtain:

$$P_{m|x_{limit}} = P_r(\lambda_S^1)^{I_1} \ (\lambda_S^2)^{I_2} \ e^{-\lambda_S^2 Ly_{max}.\, Lx_{max} \sum_{i=1}^{I_2}(t_{i+1}^2 - t_i^2)} \left(\frac{-1}{a} e^{-aLx_{max}} + \frac{1}{a}\right) \tag{4.30}$$

4.4.4. Results

In order to obtain a clearer representation, the results may be expressed as the energy, corresponding to *-log(P_j)*. The energy functions of the joint pdf and of the two other marginal pdfs are expressed as follow:

$$\begin{aligned} U_{P_j} = &-\log(P_r) - I_1 \log\left((\lambda_S^1) + \lambda_S^1 \ x_{limit} \ Ly_{max} \sum_{i=1}^{I_1}(t_{i+1}^1 - t_i^1)\right) \\ &- I_2 \log\left((\lambda_S^2) + \lambda_S^2 (Lx_{max} - x_{limit}) Ly_{max} \sum_{i=1}^{I_2}(t_{i+1}^2 - t_i^2)\right) \end{aligned} \tag{4.31}$$

$$\begin{aligned} U_{P_{m|\lambda_S^1,\lambda_S^2}} = &-\log(P_r) + I_1 \log\left((K_1 \sum_{i=1}^{I_1}(t_{i+1}^1 - t_i^1))\right) - I_1 \log(I_1) + I_1 \\ &+ I_2 \log\left((K_2 \sum_{i=1}^{I_2}(t_{i+1}^2 - t_i^2))\right) - I_2 \log(I_2) + I_2 \end{aligned} \tag{4.32}$$

$$\begin{aligned} U_{P_{m|x_{limit}}} = &-\log(P_r) - I_1 \log(\lambda_S^1) - I_2 \log(\lambda_S^2) + \lambda_S^2 \ Ly_{max} \ Lx_{max} \\ &\sum_{i=1}^{I_2}(t_{i+1}^2 - t_i^2) + \log(a) - \log\left(-e^{-a \ Lx_{max}} + 1\right) \end{aligned} \tag{4.33}$$

In a first step the Bayesian inference is used to recover the limit between the 2 zones. The optimal value of the limit between the zones is only the minimum value of the equation (4.32). Since we obtain this optimal value, we can use the equation (4.33) to recover the surface activity rate of each of the two zones.
Several cases, with different ratios between the surface seismicity rates and different observation periods, were investigated to observe the behavior of the model with the number of data.
The first example (Figure 4.9) is a representation of the 2 zones, for an observation period of 100 years. The limit between the two zones was placed at 20 kilometers, before generating the catalog.

The algorithms of the Bayesian inference are described in the chapter 9, concerning the geographical limit, and in the chapter 10, concerning the surface seismicity rates.

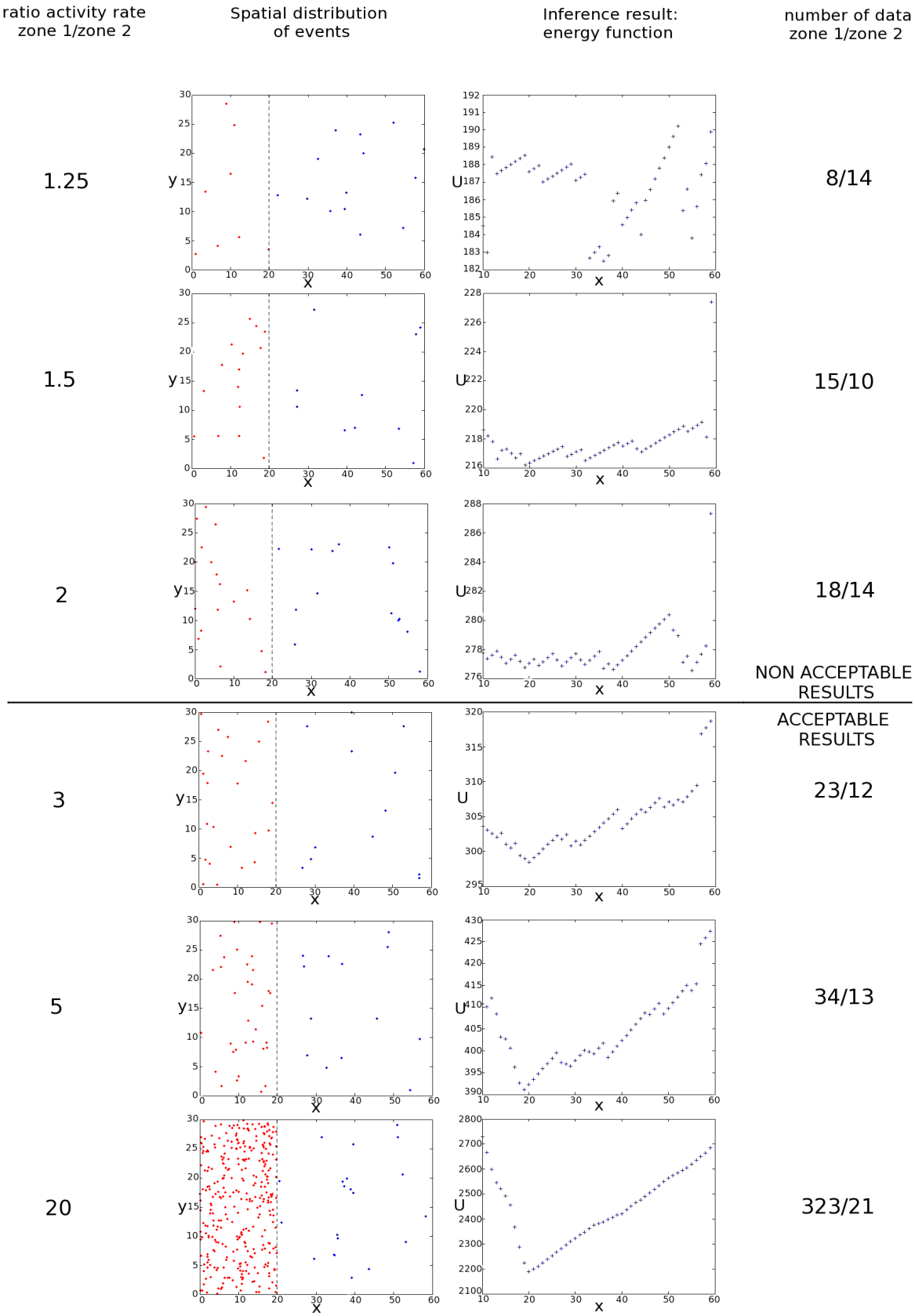

Figure 4.9: Results of the Bayesian inference to recover the limit between the two zones, for an observation period of 100 years and with different ration between the surface activity rates.

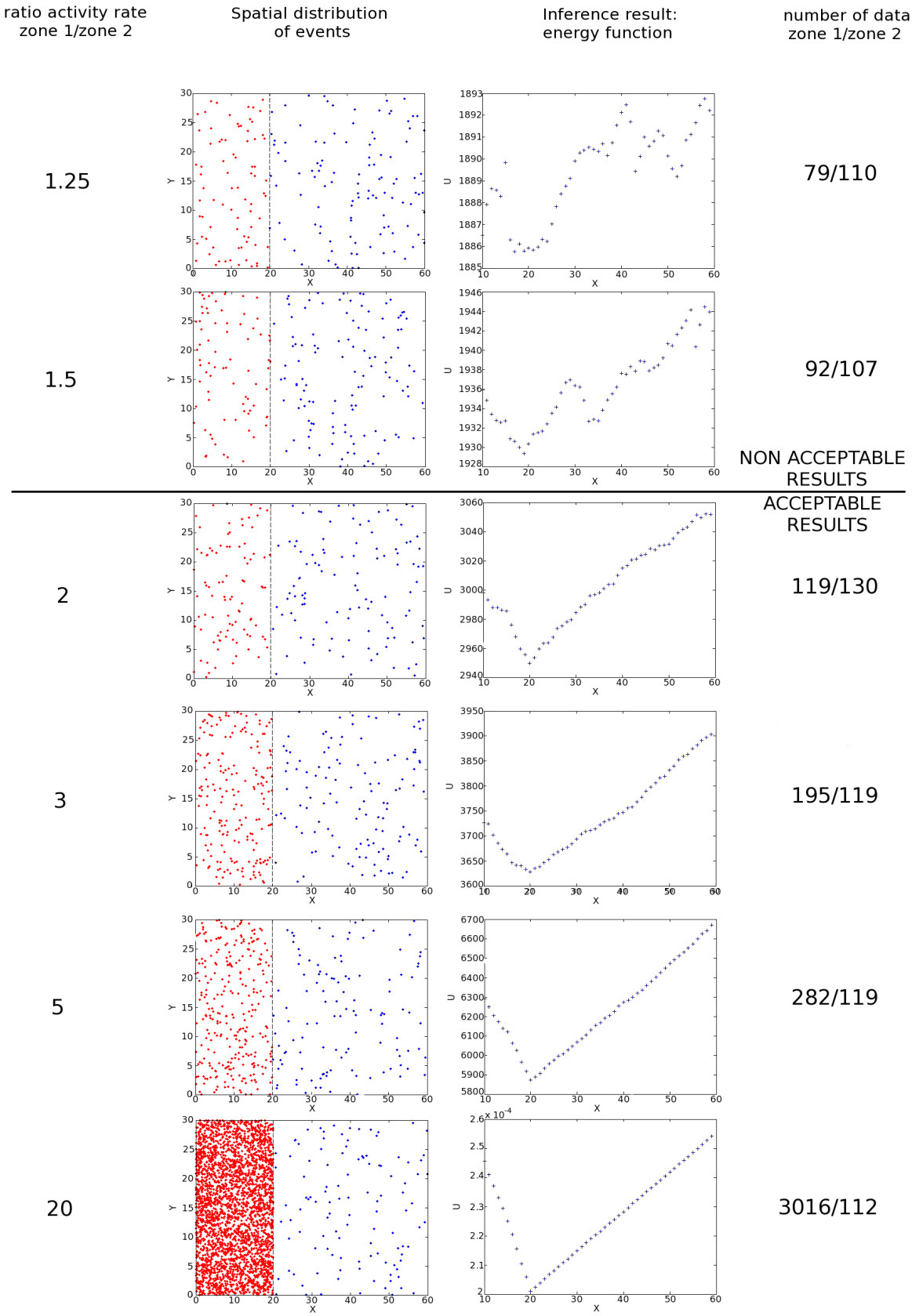

Figure 4.10: Results of the Bayesian inference to recover the limit between the two zones, for an observation period of 1000 years and with different ratio between the surface activity rates.

From the spatial distribution of the events into the 2 zones (left part of the Figure 4.9 and 4.10), we calculated the joint probability and plotted the energy function (right part of the Figure 4.9 and 4.10). Depending on the number of data, we can identify an absolute minimum value for the energy function, defining the optimal value for the limit between the two zones. We can see, in this example, that the ratio between the surface seismicity rates of the 2 zones has to be larger than 3, if we want to reach an optimal value of the limit. Some local minima may appear with a few numbers of data, and it is then necessary to achieve several realizations (paragraph 4.5).

In the second example (Figure 4.10), the limit was placed on the same location (20 kilometers), but we considered an observation period of 1000 years. The number of data points is then higher. On this example and because of the higher number of data, we can reach an acceptable solution with a ratio lower than the first example. Here a minimum value of the energy function may be reached for a ratio of 1.5. Obviously, this observation period is unrealistic but is taken into example to show the improvement of the resolving power of the Bayesian inference, when the number of data becomes larger.

Once we obtain an optimal value for the limit, we can evaluate both surface seismicity rates (Figure 4.11 and 4.12). The catalog was generated for an observation period of 1000 years and with a limit between the two zones at 20 kilometers. On these examples, the surface seismicity rates are $3x10^{-4}$ for the first zone and $1x10^{-4}$ for the second one, for the first case (Figure 4.11), and $4x10^{-4}$ for the first zone and $1.5x10^{-4}$ for the second one, in the second example (Figure 4.12).
We observe that it is possible to recover the surface seismicity rates used to generate the catalog, with a quantitative measure of the uncertainty (including the covariance).

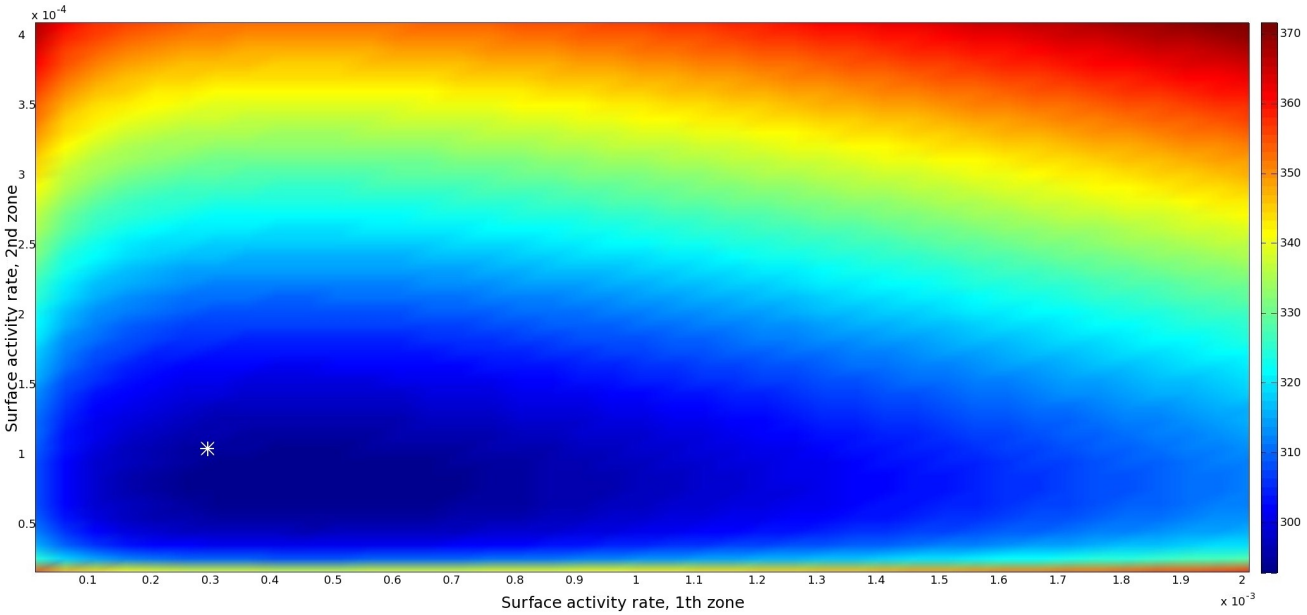

Figure 4.11: Results of the Bayesian inference to evaluate the surface seismicity rate of the 2 zones, separated at 20 kilometers. The synthetic catalog was drawn for an observation period of 100 years, with the surface seismicity rates of 3 x 10^{-4} for the first zone and 1 x 10^{-4} for the second zone (white cross). The colour variation from the red to the blue represents the decrease of the energy function. The optimal values are around 3.5 x 10^{-4} for the first zone and 1.25 x 10^{-4} for the second one.

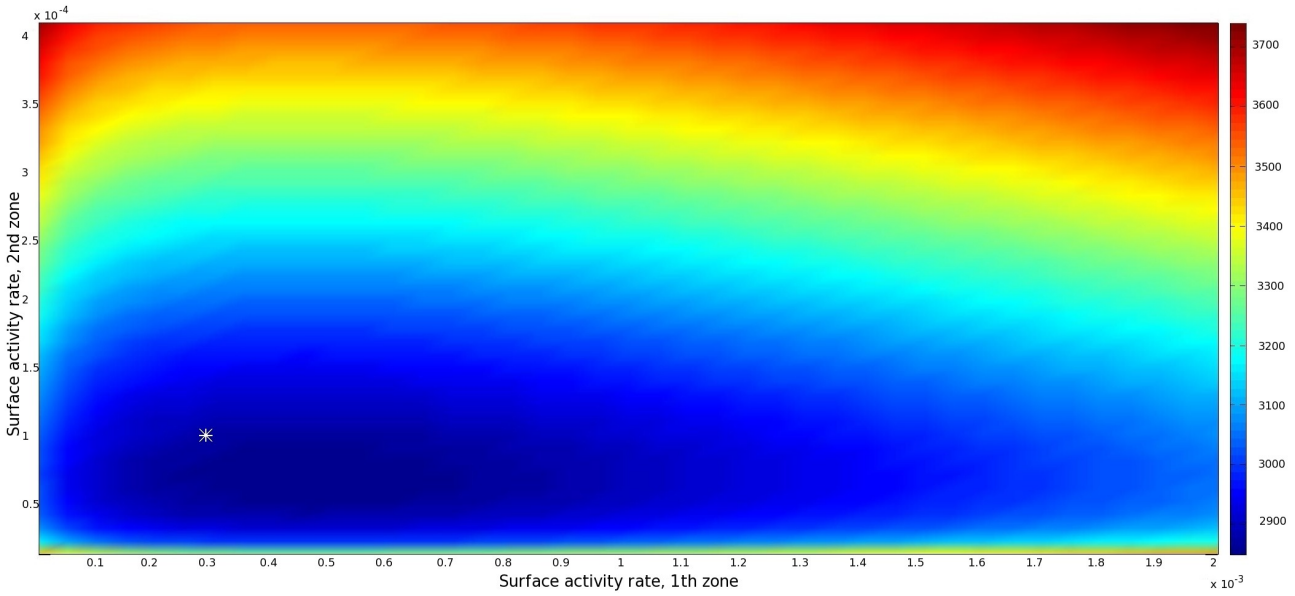

Figure 4.12: Results of the Bayesian inference to evaluate the surface seismicity rate of the 2 zones, separated at 20 kilometers. The synthetic catalog was drawn for an observation period of 1000 years, with the surface seismicity rates of 4 x *10^{-4} for the first zone and 1.5* x *10^{-4} for the second zone (white cross). The color variation from the red to the blue represents the decrease of the energy function. The optimal values are around 4* x *10^{-4} for the first zone and 1.6* x *10^{-4} for the second one.*

4.4.5. Uncertainty and variability

According to the realization of the catalog, the optimal value may not represent the real solution. It is then important to compare the distribution of the optimal values we can obtain. The histograms, presented in the figures 4.13 and 4.14, express the optimal values of the limit between the two zones, for 100 realizations of catalogs. In the first example (Figure 4.13), 100 synthetic catalogs were drawn for an observation period of 100 years and with the surface seismicity rates of 3 x 10^{-4} for the first zone and 1 x 10^{-4} for the second one. In the second example (Figure 4.14), 100 synthetic catalogs were drawn for an observation period of 1000 years with the surface seismicity rates of 1.5 x 10^{-4} for the first zone and 1 x 10^{-4} for the second one.

These figures show the importance of using different realization of synthetic catalogs. Indeed, with only one synthetic catalog, the optimal value for the limit may be on the tail of the distribution. With the distribution shown on the figure 4.13, the use of Monte-Carlo draws, with an initial value on the right of the distribution, may lead to a local minimum, around 27 kilometers or 37 kilometers.

The standard deviation of the resulting Bayesian inference is given by the curvature of the energy function in the optimum value. This corresponds to the inverse of the square root of the second derivative of the energy function in the optimum value.
Concerning the limit between the two zones, the second derivative is given by:

$$\frac{\partial^2 \left(U_{P_{m|\lambda_S^1,\lambda_S^2}}\right)}{\partial x_{limit}^2} = \frac{-I_1}{x_{limit}^2} - \frac{I_2}{\left(x_{limit} - Lx_{max}\right)^2} \tag{4.34}$$

and the resulting standard deviation is given by:

$$\sigma_{x_{limit}} = \frac{1}{\sqrt{\left| \frac{-I_1}{x_{limit}^2} - \frac{I_2}{(x_{limit} - Lx_{max})^2} \right|}} \tag{4.35}$$

The standard deviations of the Bayesian inference, corresponding to each catalog realization, are resumed in the histograms 4.15 for an observation period of 100 years and 4.16 for an observation period of 1000 years. We observe an uncertainty in the limit between the two zones around 4 kilometers for an observation period of 100 years. This uncertainty decreases largely with an increase of the number of data (larger observation period) to go down to 1 kilometer for a observation period of 1000 years.

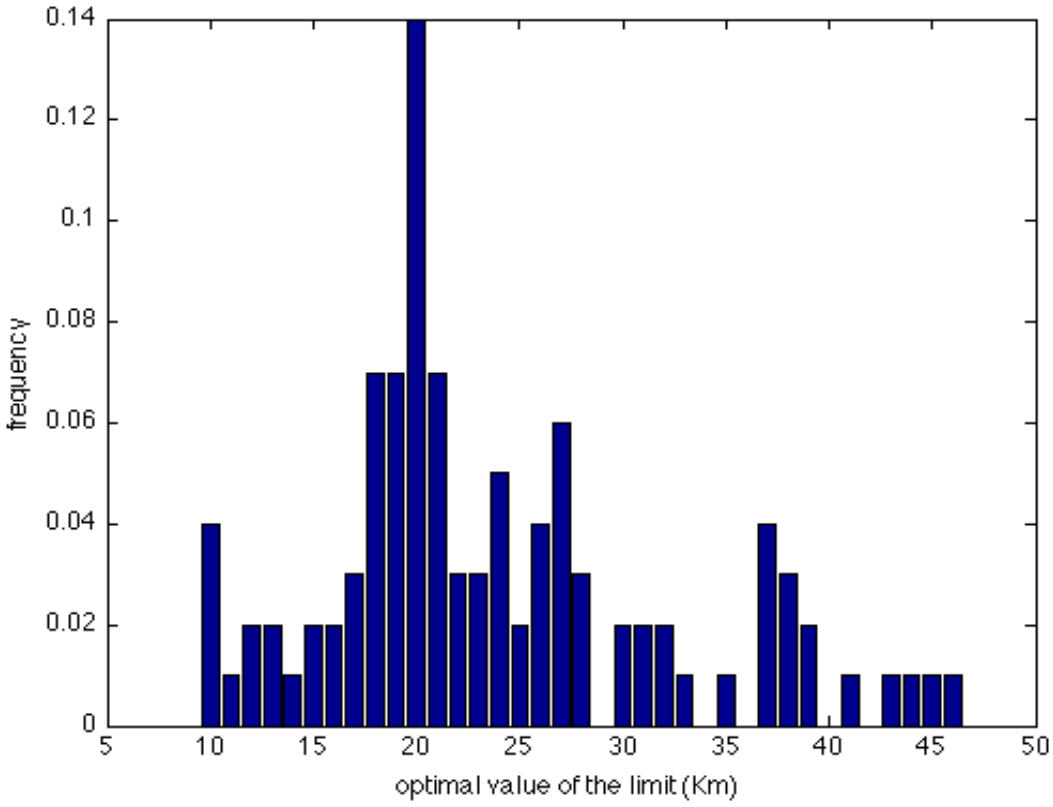

Figure 4.13: Distribution of optimal values for the limit from 100 synthetic catalogs, drawn for an observation period of 100 years and with the surface seismicity rates of 3 x 10^{-4} for the first zone and 1 x 10^{-4} for the second one.

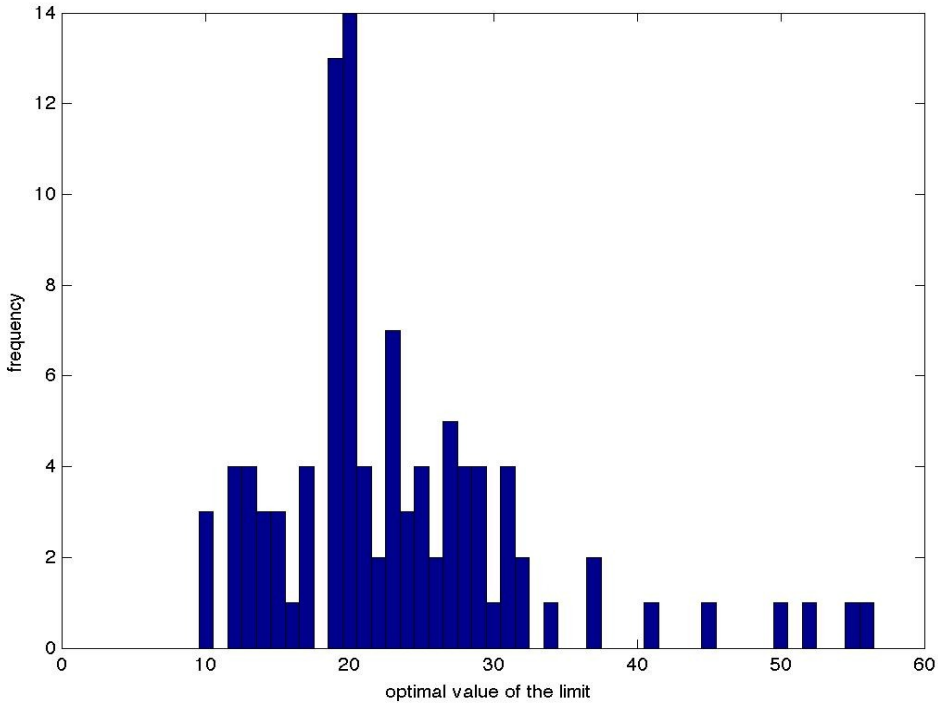

Figure 4.14: Distribution of optimal values for the limit from 100 synthetic catalogs, drawn for an observation period of 1000 years and with the surface seismicity rates of 1.5 x 10^{-4} for the first zone and 1 x 10^{-4} for the second one.

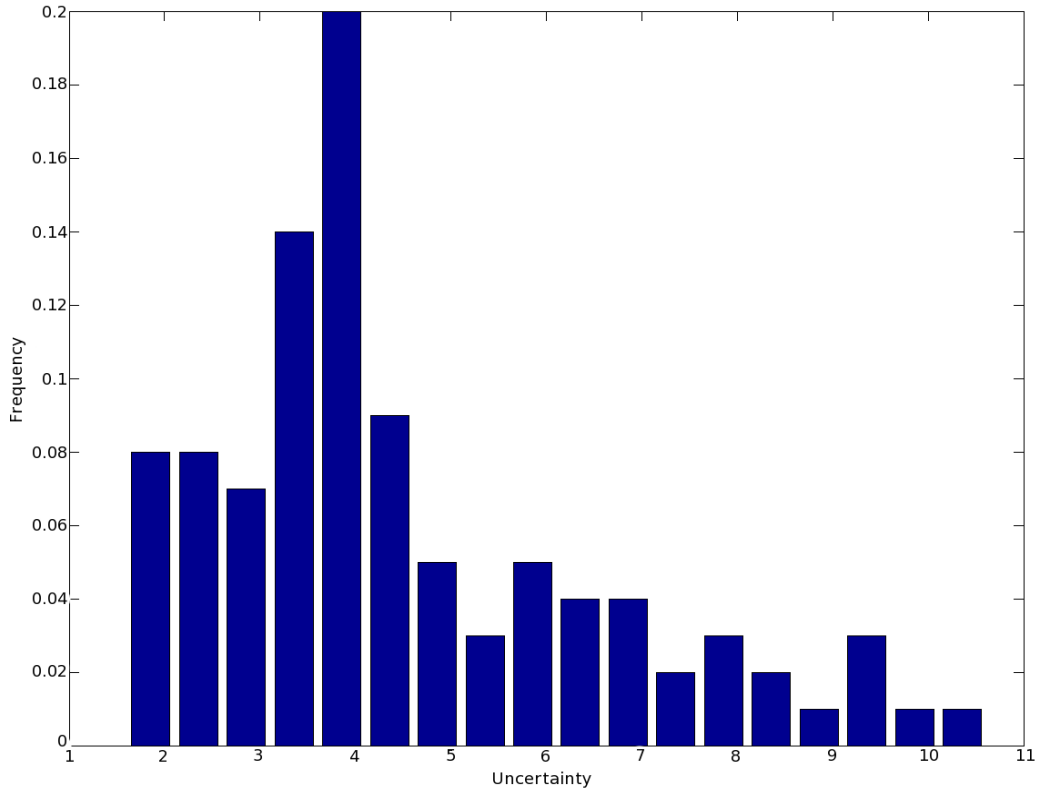

Figure 4.15: distribution of the uncertainties on the determination of the limit between the two zones, from 100 synthetic catalogs drawn for an observation period of 100 years.

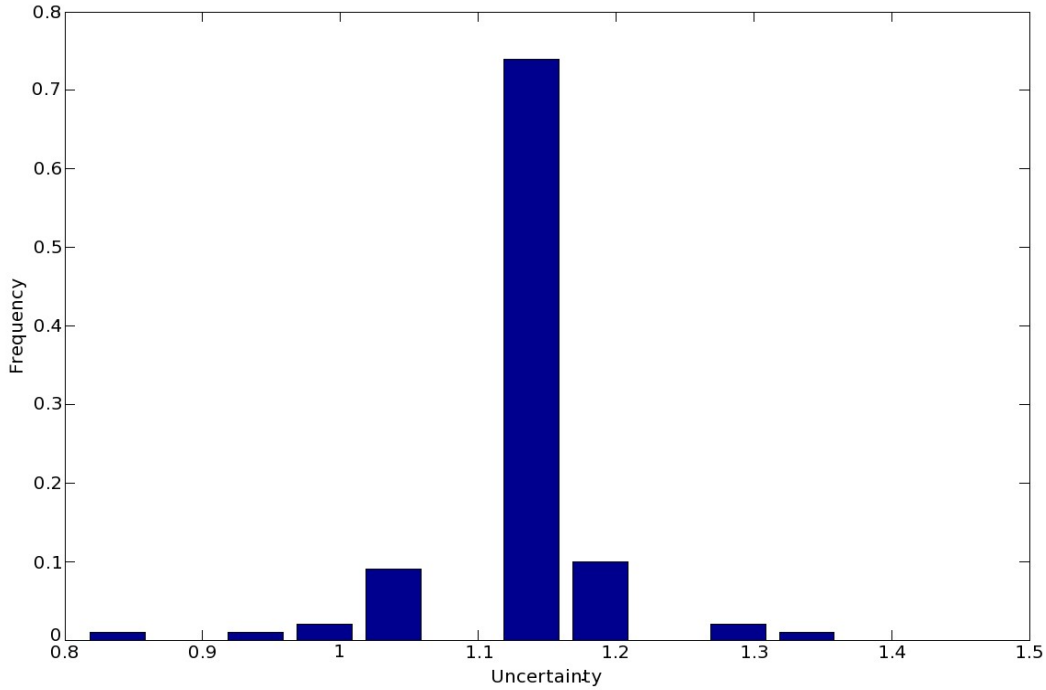

Figure 4.16: distribution of the uncertainties on the determination of the limit between the two zones, from 100 synthetic catalogs drawn for an observation period of 1000 years.

4.5. Applications

The previous results are obtained from synthetic catalogues that are considered complete, without uncertainties or lack of data. Applying this methodology to real cases is an important point to define if the model may overcome the lack of data.

We studied two different cases:

- Example from GEOTER International data to detected the existence of a limit between two zones or if the two zones may be joined in a single one.
- Example from the PSHA of Portugal (Villanova and Fonseca, 2007) to define the location of the limit

4.5.1. Geoter International example

In this example, the data are provided by Geoter International. However, these data are confidential and no sources can be provided. We wonder if it is justified to isolate a seismic swarm from the rest of the zone or if we can consider a single zone incorporating the seismic swarm (figure 4.17 and 4.18) to evaluate the probabilistic seismic hazard. The PSHA calculation each model has been considered through a logic tree with different weight.

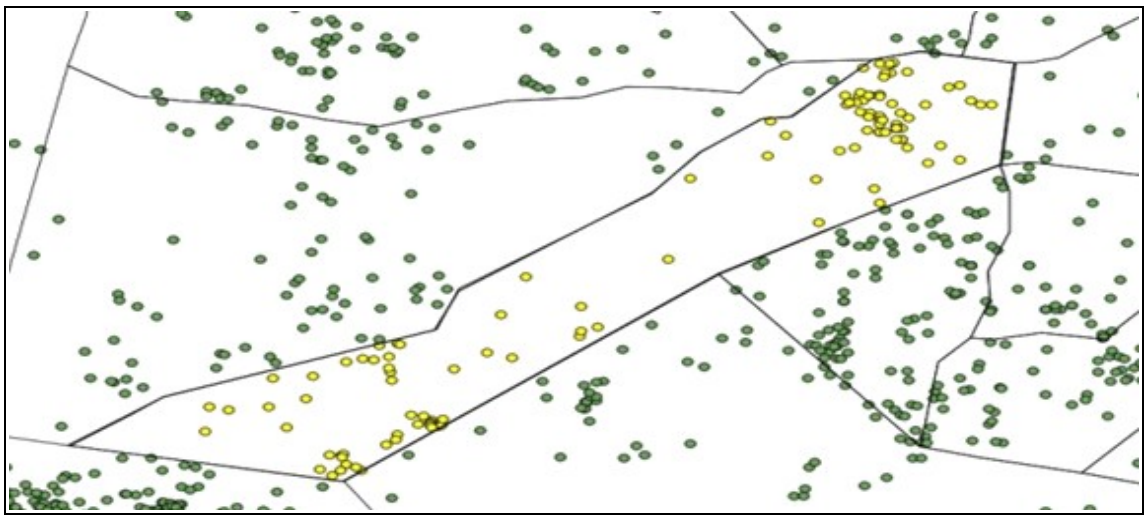

Figure 4.17: Zoning 1 of GEOTER study. The yellow points represent the earthquakes that are inside the study zone and the green ones represent the earthquakes outside the study zone. The seismic is in top right corner of the figure.

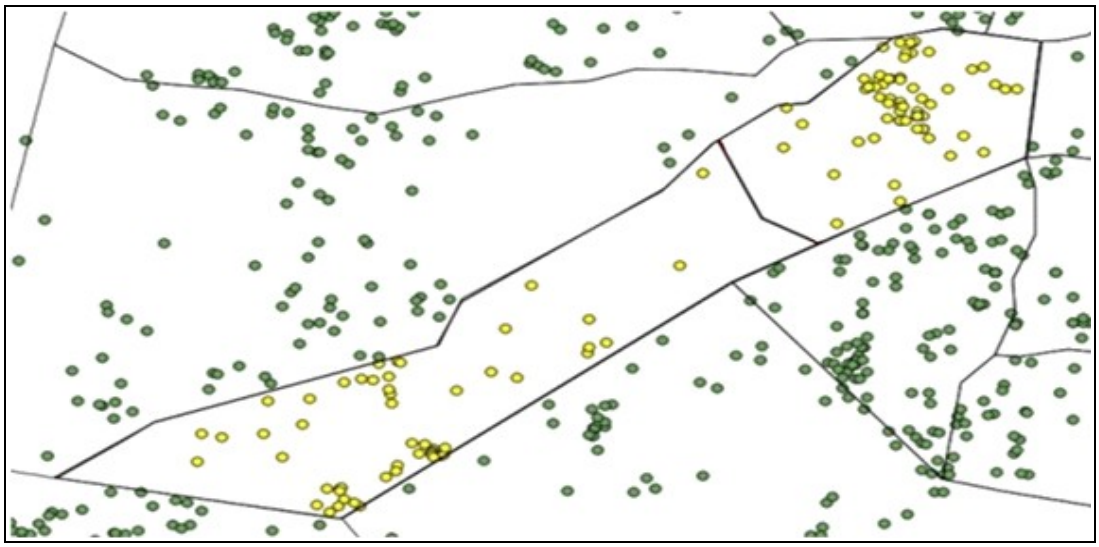

Figure 4.18: Zoning 2: In this case, the seismic swarm is isolated into a zone

Defining one or two zones has an important impact into the resulting seismic hazard. Using the events of the unique zone, in the zoning 1, we computed the energy function to obtain the optimal value of the limit. The results obtained with our Bayesian model are represented in the figure 4.19.

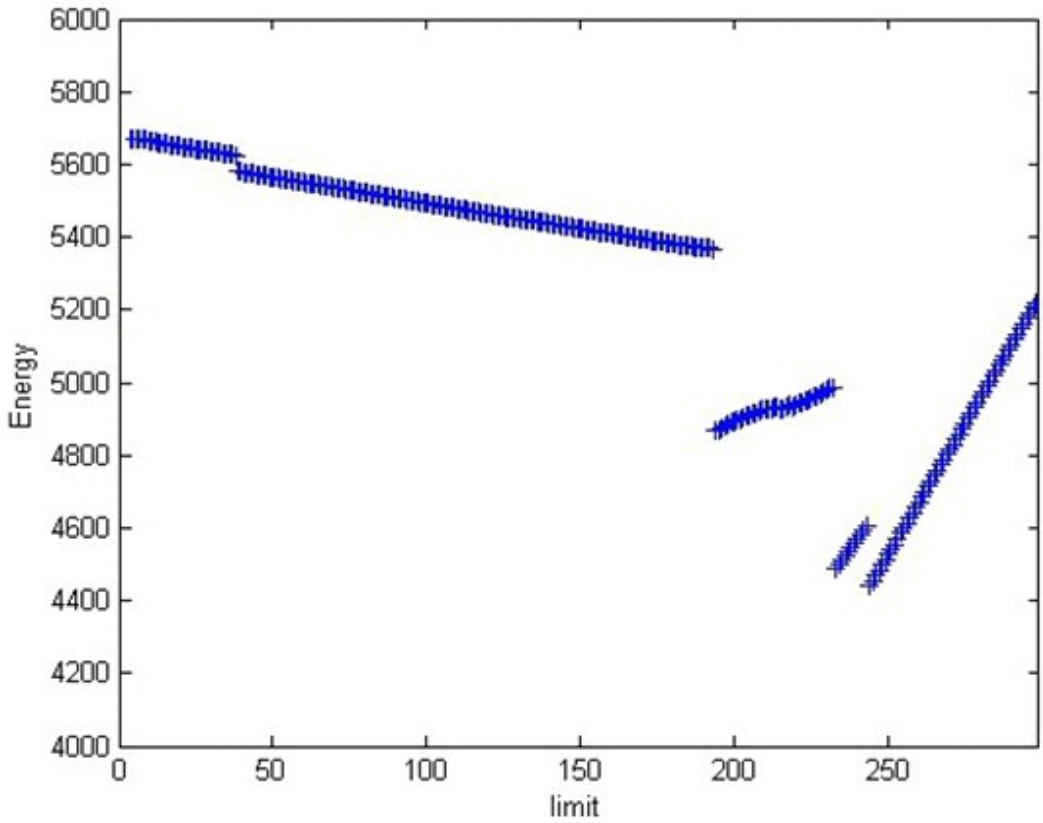

Figure 4.19: Resulting energy function as a function of the limit.

We observed an absolute minimum of the energy function at 246 kilometers. The uncertainty related to this value is 5.574 kilometers.

If we represent the optimal value of the limit in the previous map, we observe that the probabilistic limit is close to the seismotectonic limit (figure 4.20).

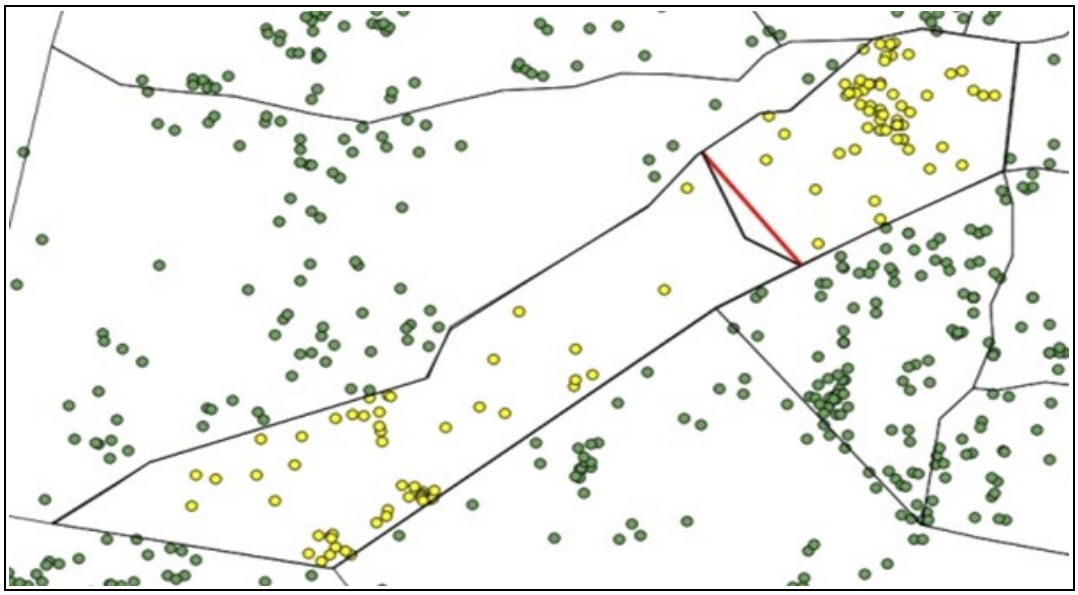

Figure 4.20: Representation of the probabilistic limit of the zone (in red) and the seismotectonic limit (black).

In this study case, we can conclude that a limit to isolate the seismic swarm is justified by the surface activity rates using the Bayesian model. We also provide a location of this limit with its related uncertainty.

4.5.2. PSHA in Portugal (Villanova and Fonseca, 2007)

For this example, we used the same data as the one used in the definition of the PSHA achieved in Portugal by Villanova and Fonseca (2007). In order to be coherent with the PSHA study, the same catalogue was used (not an updated one) and the same seismotectonic zoning (figure 4.21).

The interest of this example is to observe if we obtain the same location of the limit between two zones in the Algarve region, in the south of Portugal.

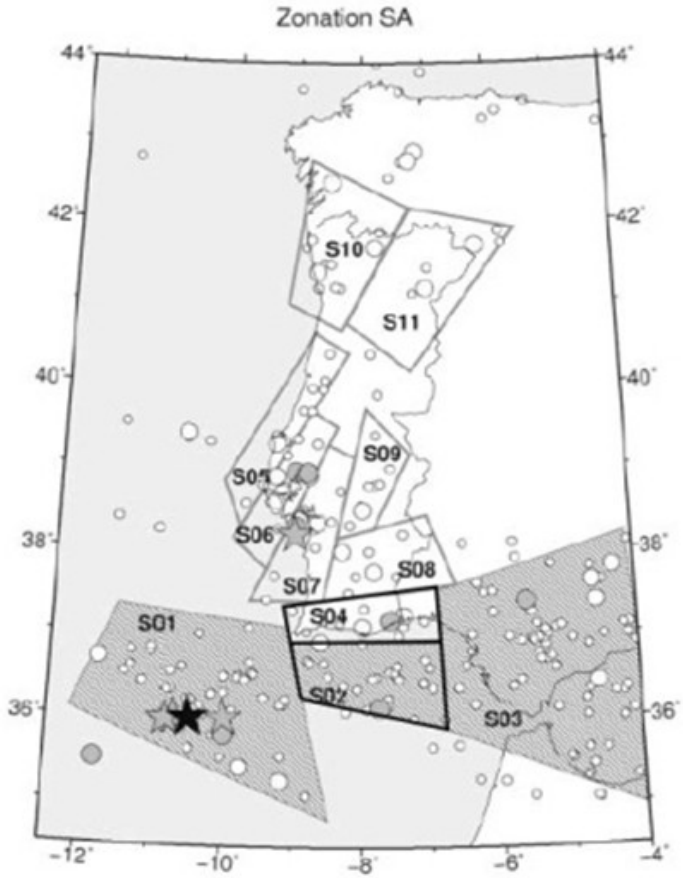

Figure 4.21: Seismotectonic zoning and earthquake catalogue used for the PSHA calculation in Portugal (Villanova and Fonseca, 2007). The bold zones S02 and S04 are the ones considered in this study and, more particularly, the limit between them.

Using the events of both S02 and S04 zones, we computed the energy function to obtain the optimal value of the limit. The results obtained with our Bayesian model are represented in the figure 4.22.

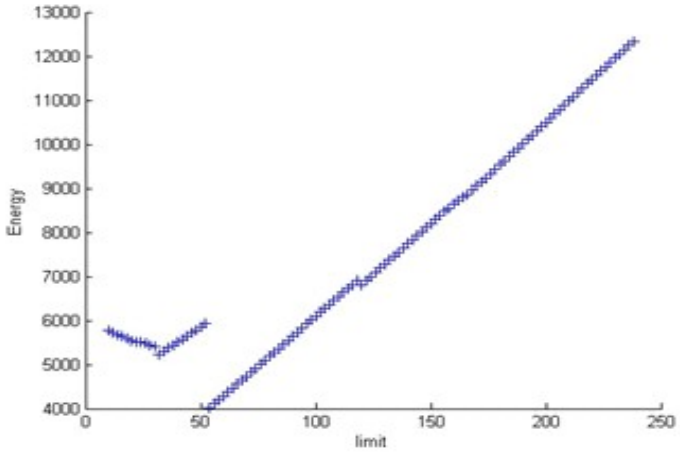

Figure 4.22: Resulting energy function as a function of the limit.

We observed an absolute minimum of the energy function. The uncertainty related to this value is 4.212 kilometers.

If we represent the optimal value of the limit in the previous map, we observe that the probabilistic limit is lightly northward from the seismotectonic limit (figure 4.23).

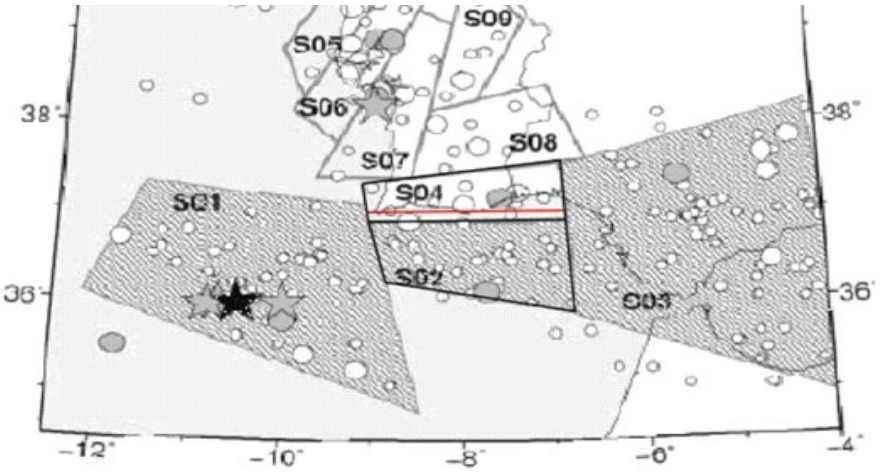

Figure 4.23: Representation of the probabilistic limit of the zone (in red) obtained in this study and the seismotectonic limit (in black) used in the PSHA calculation (Villanova and Fonseca, 2007).

In this study case, we can conclude that a limit is justified by the surface activity rates between the S02 and S04 using the Bayesian model. Moreover we provide a location of this limit with its related uncertainty.

4.6. Discussion

During about 20 years, the evolution of PSHA in current practice has been slowed down by using paying software within which code source is not known and shared. But recently, initiatives have been undertaken, first in California with openSHA and after in international-wide with Global Earthquake Model (GEM), to propose an open source code, making it easier to incorporate new methodologies. The methodology, presented in this thesis, could therefore be inserted in the hazard calculation process.

The intervention of panels of experts, that was used in first attempts at assessing epistemic uncertainties, needs to be transformed and moved "upstream" whenever it is possible. The expert decisions may be incorporated as priors and avoid using expert decisions.

With our contribution, we show how Bayesian Inference would be useful in Probabilistic Seismic Hazard Assessment. Other authors have pointed that out in the recent past, for renewal models (Biasi and Weldon, 2008; Fitzenz and al, 2007), or for a general view (Esmer, 2006).

The Bayesian model used in this study is developed to find a limit between two zones, differentiated by two different surface activity rates. So far, the results may not be used in a PSHA calculation and is not representative of a seismotectonic zoning.
Indeed, a seismotectonic zoning allows linking the seismicity with the tectonically-active geological structures. In our model, only data from seismicity catalogs are used, reducing the zoning to a seismic zoning. Geological data (e.g., alluvial zones, granitic uplands), structural data (e.g., fault orientations, fault lengths, focal mechanisms) but also complementary seismicity data (e.g., paleoseismicity) have to be incorporated into this model. A new joint probability density function, related to a new graphical model, needs to be achieved. All additional data will improve the resolving power of this method, reducing the minimum number of data, n_{min}, required in a seismicity catalog to recover the geographical limit between the two zones and their respective surface activity rates.

Moreover, this Bayesian model is restricted to two different zones. It is important to consider a model with an undefined number of zones. Two approaches are conceivable: the first one consists in redefining the graphical model and recalculate the corresponding joint pdf for a number n of zones. The second approach consists in subdividing each resulting zone, using the same Bayesian inference, until no absolute minimum can be identifiable.

The method of Bender (1986) may be adapted in order to calculate the seismicity rates. In our method, the uncertainty, related to the limit between the zones instead of arbitrary defined for all events, can be used to define the contribution of this source to several zones. A point source would contribute to the seismicity rate calculation of several zones. The fact that a source, close to a seismotectonic zoning boundary, may participate in the calculation of several seismicity rates allows smoothing these rates in source zone boundaries. Thus, in proximity to a source zone boundary, resulting acceleration levels for two close sites may not differ considerably.

4.7. Conclusion

The objective of this approach is to model a seismotectonic zoning which 1) is reproducible and 2) preserves the information on the source and extent to the uncertainties, so as to allow propagating them and issue recommendations for optimized future data acquisitions.

An inference with two zones, differentiated by two different surface seismicity rates, was performed to obtain the geographic limits between them. To obtain an acceptable accuracy on the location of the limit between the 2 zones, the ratio of the surface activity rates has to be larger than 3, for an observation period of 100 years. Considering an observation period of 1000 years, this ratio is reduced to 1.5, because of the higher number of data.

This 2 zone model will be a reference in the comparison with other models, which will incorporate

other available data. Future improvements need to be achieved to obtain a seismotectonic zoning. This model needs to integrate structural data (e.g., fault orientation, fault length) and the geology data as well. This will allow reducing the minimum number of data, n_{min}, required in an earthquake catalog to recover the activity rates of both zones and the geographical limit between them, with some confidence. Also, this model needs to be extended to a number n of zones with a unspecified shape.

We emphasize that such an approach is reproducible once priors and data sets are chosen. Indeed, we will strive to incorporate expert opinions as priors, and avoid using expert decisions. Instead, the products will be directly the result of the inference, when only one model is considered, or the result of a combination of models in the Bayesian sense.

CHAPTER 5

Historical event relocation and Intensity-distance attenuation law

5.1. Introduction

In our probabilistic model, the earthquake locations are essential. So, we need to obtain these data with the best accuracy possible. First, we need to differentiate the data provided by the instrumental catalogs and the data provided by the historical catalogs. In the first case, the uncertainty on earthquake location is related to the occurrence date of the event. The improvement of calculation methods and the development of the seismic network, allowed obtaining more accurate instrumental location. Nevertheless, this uncertainty can be reduced using the method of the double-difference (Waldhauser and L. Ellsworth, 2000). The location uncertainty of the historical earthquakes is related to the number of intensity data points available and the method used to achieve this location. Most of time, the estimation of an historical earthquake location is done using isoseismal lines delimited by experts, introducing a subjective part. The method of Bakun and Wentworth (1997) allows estimating the epicentral region and the moment magnitude of an historical earthquake, directly from its intensity data points rather than the isoseismal lines. The significant advantage in using individual intensity observations directly is that the procedures are explicit so that the results are reproducible. The results of such a method provide an estimation of the epicentral region with levels of confidence appropriated for the number of intensity data points used.

We chose to apply this methodology to the 1909 Benavente event (M_w=6.0) because it is one of the most documented (Bensaude, 1910; Teves-Costa and Batlló, 2010). This event is also the only one, in Portugal mainland, who provides intensity data points with small epicentral distances. The other reason to investigate this event is its controversial location, estimated from its isoseismal lines that present particular shapes (Mezcua, 1982; Senos et al., 1994; Teves-Costa and Batlló, 2010). This method will be applied using the attenuation law of Atkinston and Boore (1997), already used in the calculation of the PSHA in Portugal (Vilanova and Fonseca, 2007). We developed a new intensity-distance attenuation law for the Portugal mainland, using the macroseismic reports of events that provide intensity data points and instrumental magnitudes. This law is directly derived from the intensity data points and expressed as a function of magnitude and epicentral distances.

5.2. Bakun and Wentworth methodology

The methodology of Bakun and Wentworth (1997) allows estimating the epicentral region and the moment magnitude of an earthquake, from its intensity data points. The method consists in defining a magnitude M_I and its related error (noted rms[M_I]) over a grid of assumed epicenters. M_I corresponds to the mean of the M_i, with M_i the magnitude calculated from the attenuation law related to the i^{th} intensity data point. The rms[M_I] is defined by rms[M_I] = rms($M_I - M_i$) – rms$_0$($M_I - M_i$), where rms$_0$($M_I - M_i$) is the minimum of rms over the grid of assumed epicenters. For each point of the grid of assumed epicenters, a value of M_I and rms[M_I] is calculated. The epicentral region is bounded by contours of rms[M_I], while the estimated magnitude is bounded by the M_I values. These empirical contour values are estimated for different levels of confidence, associated to the quantity of intensity data points available. This method is particularly appropriate for the evaluation of historical earthquakes, for which the only available data are sparse set of intensity observations.

5.3. 1909 Benavente event

5.3.1 State of art

The earthquake of Benavente occurred the 23th of April 1909, in the region of the Lower Tagus Valley. This earthquake is associated to the city of Benavente because it was the city the most damaged.
According to the estimation of Choffat and Bensaude (1912), around 40% of the building collapsed or had to be demolished and another 40% required major repairs. This earthquake is considered as the largest crustal earthquake in the Iberian Peninsula.

This event is located in the Low Tagus Valley, where severe earthquakes already occurred (1344, 1531), and is associated to the fault system of the Low Tagus Valley (Cabral et al., 2000, 2004). The epicenter location was estimated at 38.9˚ N, 8.8˚ W, using the available macroseismic information, by Kárnick (1969). From different studies, based on the seismic moment estimation, the moment magnitude, M_w, was estimated between 6.0 and 6.2 and M_s close to 6.3 (Teves-Costa et al. 1999, 2005; Dineva et al. 2002; Stich et al. 2005).

Stich et al. (2005) determined a focal mechanism of a reverse faulting. This is in agreement with other focal mechanisms calculated for this region (Borges et al. 2001). However, this focal mechanism is not well constrained due to the lack of data.

Several authors have proposed an isoseismal map for this event (Mezcua 1982, Moreira 1991, Senos et al. 1994, Teves-Costa and Batlló, 2010). The map of Mezcua is represented in the figure 5.1 and the map of Teves-Costa and Batlló in the figure 5.2. The map of Mezcua presents a simplified copy of the original map of Choffat and Bensaude (1912) with slight modifications. The map of Teves-Costa and Batlló expresses the isoseismal lines after a review of the macroseismic intensity data points. They underline an East-West extension of the isoseismal curves. This extension may be explained by local site effects or by cascading events.

This event is the most documented, owing to the preliminary work of Bensaude (1910) and the work of macroseismic field revision of Teves-Costa et al. (2010) and because of its occurrence in the continent (figure 4.1 and 4.2).

5.3.2. Relocation of the 1909 Benavente event using the Bakun and Wentworth method (1997)

The data used in this study are the intensity data points provided by the macroseismic field revision of Teves-Costa and Batlló (2010) (figure 5.2). The database is composed by 504 intensity data points. The name of the locality, the longitude, the latitude and the intensity are given for each of the intensity data point. All the intensity values are expressed in the Modified Mercalli scale (Wood and Neumann 1931).

The method of Bakun and Wentworth (1997) is applied to this event using the Atkinston and Boore (1997) attenuation law (used in the Portuguese PSHA calculation).
In the resulting map of earthquake location and magnitude estimations, achieved with the Atkinston and Boore (1997) attenuation law (figure 5.3), we observe that the epicenter estimated by Kárník (1969) is within all the confidence level contours. The minimum of rms[M_I] is close to the Kárník

epicenter estimation.

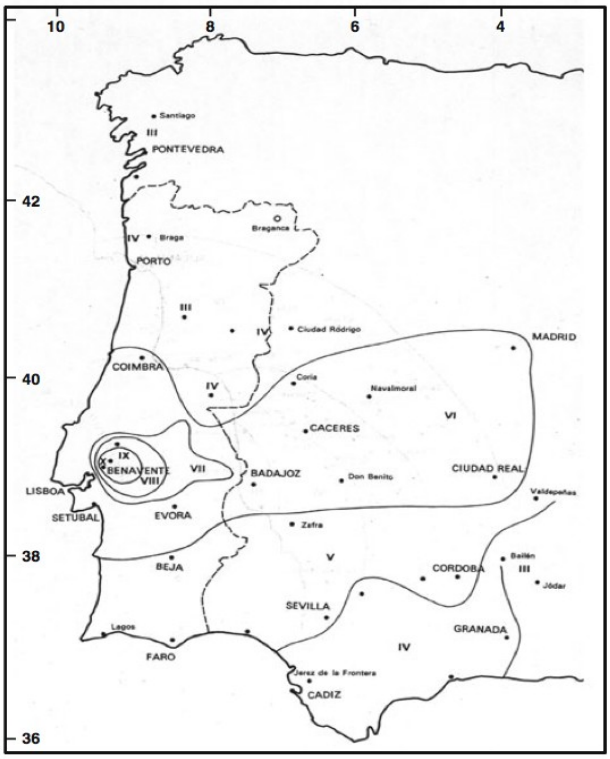

Figure 5.1: Isoseismal curves for the 1909 Benavente earthquake. From Mezcua (1982)

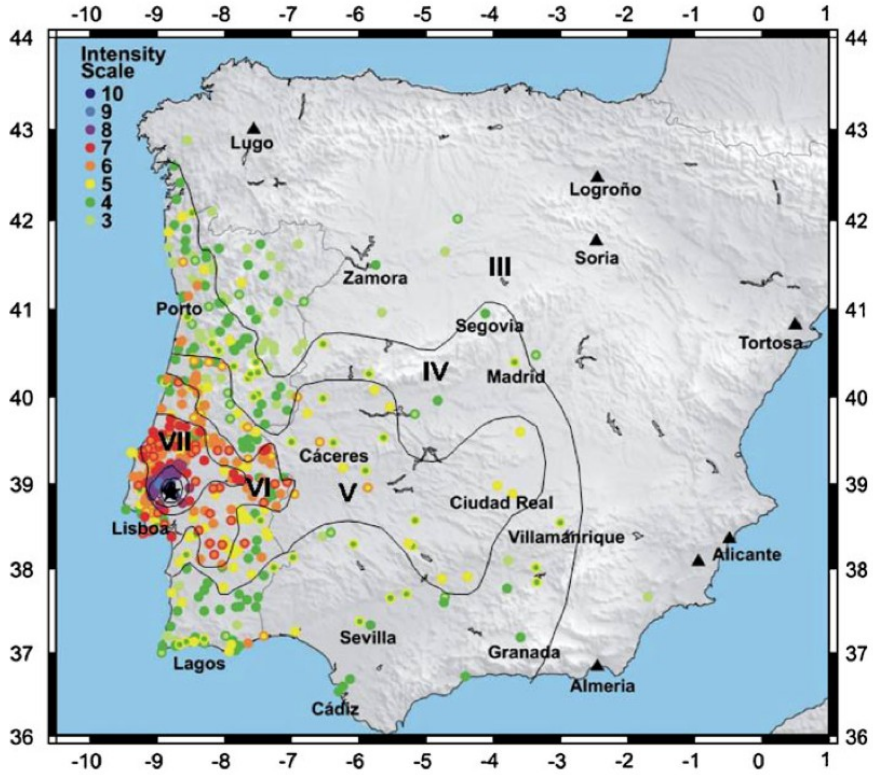

Figure 5.2: Intensity data points and tentative isoseismal curves for the 1909 Benavente event, using intensity information collected for 504 points. When the assigned intensity present incertitude between two degrees (for instance IV–V), the inner colour is the lower degree and the outside circle presents the color of the higher degree. Black triangles indicate localities where the earthquake was not felt. From Teves-Costa and Battló (2010)

Generally, the minimum of rms[M_I] does not correspond to an estimation of the epicenter but expresses the location that best explains the maximum observed intensity. Indeed, the rupture process cannot be represented by a point source model and we have to consider the rupture propagation. But, because the Kárníc epicenter estimation is done with macroseismic data, we can directly correlate this epicenter estimation with the obtained minimum rms[M_I]. We therefore expect a minimum of rms[M_I] nearby the epicenter. The estimated magnitude for this event is 5.8 (minimum rms[M_I] inside the 5.8 contour) that is lower than the reference instrumental magnitude M_w of 6.0, defined in the literature (Teves-Costa et al. 1999, 2005; Dineva et al. 2002; Stich et al. 2005). The estimation of the earthquake location is quite satisfying for the 50% and 80% confidence level contours. However, the 95% confidence level contour extends in the N-W and becomes large.

The underestimation of the magnitude and the N-W extension of the 95% confidence level contour may be due to the use of an inappropriate intensity-distance attenuation law. We decide to test the sensibility of this method to the attenuation law. A new attenuation law is developed using a compilation of macroseismic reports and will be used to re-estimate the epicentral region and the magnitude of the 1909 Benavente event.

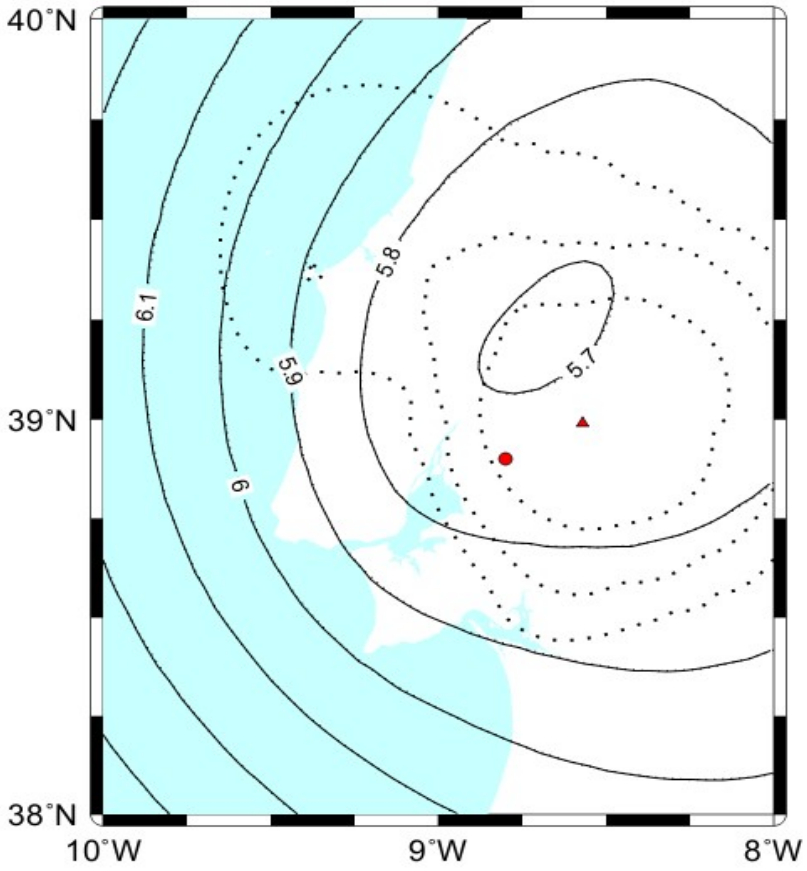

Figure 5.3: Resulting magnitude and earthquake location of the 1909 Benavente event, using the Bakun and Wentworth method (1997) with the Atkinston and Boore (1997) attenuation law. Solid lines represent the contours of M. The red dot represents the epicenter estimated by Kárník (1969). The red triangle represents the location of the minimum value of rms[M_I] over a grid of assumed epicenters. The rms[M_I] contours corresponding to the 50%, 80% and 95% confidence levels for location are shown as the innermost, middle, and outermost contours of dotted lines, respectively.

5.4. Intensity-distance attenuation law for the Portugal mainland

5.4.1. Introduction

In low to moderate seismic regions, like the Portugal mainland, the computation of attenuation laws is made difficult by the lack of data. Given that most of the largest earthquakes occurred before the development of seismic instruments, the instrumental data are small and are related to low magnitude events.

The attenuation laws are mainly used to compute the seismic hazard. Usually, in regions of moderate tectonic and seismic activity, such as the study area, the resulting seismic hazard is computed using preexisting attenuation laws, developed for similar areas and for similar ranges of magnitude. In Portugal, Vilanova and Fonseca (2007) computed the Probabilistic Seismic Hazard using 3 attenuation models (included into a logic tree): Ambraseys et al. (1996), Toro et al. (1997) and Atkinston and Boore (1997), developed for target areas of Europe and Middle-East in one case and Central and Eastern North America in the other two.

Several attempts have been done to evaluate an attenuation law in the Iberian Peninsula (Muñoz, 1974, Martin 1984; Lopez Casado et al. 1992; Sousa and Oliveira, 1997; Lopez Casado et al., 2000). Yet, the results are not satisfying and do not directly use the intensity data points of the available events but the isoseismal maps instead. In these maps, the isoseismal lines are set by expert decisions, introducing a subjective part into the resulting laws. The main advantage of using directly the intensity data points allows the procedures to be explicit and the results to be reproducible. Moreover, in most of the studies, the attenuation laws are not expressed as a function of the magnitude, but as a function of the epicentral intensity I_0.

We developed a new intensity-distance attenuation law for the Portugal mainland, using the macroseismic reports of events that provide intensity data points and instrumental magnitudes. This law is directly derived from the intensity data points and expressed as a function of magnitude and epicentral distance.

The methodology includes three steps: 1) the estimation of the equation form, 2) the study of the attenuation law parameters as a function of the magnitude, 3) the definition of the attenuation equation. The attenuation law will be provided with its associated uncertainties. It is important to notice that the obtained attenuation law does not take into account the site effects.

Subsequently, two methods are achieved using the new intensity-distance attenuation law to validate it. The first one consists in relocating the Benavente earthquake occurred the 23th of April 1909 (moment magnitude M_w=6), located closed to Lisbon, with the Bakun and Wentworth method (1997), using 1) the Atkinston and Boore (1997) attenuation law (used in the Portuguese PSHA calculation) and 2) the new attenuation law, in order to validate whether the use of the new attenuation law improves the results. The second one consists in studying the site effects and check if there is a correlation between them and the intensity residuals, defined by the difference between the observed 1909 Benavente event intensity data points and the ones calculated with the new attenuation law, into which the site effects are not expressed.

5.4.2. Methodology

The methodology used to compute the attenuation law for the Portugal mainland is inspired from Bakun and Wentworth (1997). First we needs to estimate the equation form. It consists in defining for each event the regression line that better fits the intensity data points in function of the epicentral distances. We consider here the median epicentral distance for each range of intensity to minimize the weight of extreme values, which might be erroneous or exaggerated. Three different kinds of regression are tested: linear, exponential and logarithmic. For each event, the regression coefficient of the different tendencies is calculated and compared each other. The tendency that presents the best regression coefficients over all events is used to define the form of the attenuation equation.

Once we obtained the form of the attenuation equation, we study the behavior of its parameters as a function of the magnitude. These parameters correspond to the slope and the intercept of the attenuation law. The slope of each earthquake is represented as a function of its corresponding magnitude. Then, the evolution of the slope with the magnitude is estimated. Similar plot is obtained using the intercepts instead of the slopes, to evaluate the behavior of these intercepts with the magnitude. This allows defining the analytic form of the different parameters that are introduced into the attenuation equation.

Finally, from the complete analytic expression of the attenuation equation, the attenuation law is obtained using the least square method. This method provides the uncertainty associated to the attenuation law.

Then, we tested our attenuation law by studying the site effects. Because our attenuation law does not include site effects, the positive intensity residuals (that is the difference between the theoretical and the observed intensity: I_{obs}-I_{theo}) should match with Portuguese regions where site effects are known (Bezzeghoud et al., 2011), like the Meso-Cenozoic basins.

5.4.3. Data

The data required for the computation of the attenuation law, have to provide an instrumental magnitude and a felt intensity report. We obtained, from the Instituto Português do Mar e da Atmosfera (IPMA, Portugal; ex-IM), 30 events, covering the period since 1909 until 1997. These events are listed in the table 5.1 and mapped in the figure 5.4. The largest magnitude is Ms=8.4 for the 1941 November 25th earthquake, located closed to the boundary separating the Eurasian and the Nubian plates. The intensities are expressed in the Modified Mercalli scale. The magnitudes are expressed in different scales and are converted to a homogeneous magnitude. The moment magnitude, Mw, is chosen as reference. The magnitudes provided by the Instituto Geografico Nacional (IGN, Madrid) are calculated in m_{bLg}. The ones collected from publications (Buforn et al. 1988, Buforn et al. 1995, Grandin et al. 2007) are expressed as surface wave magnitude, Ms. We noticed that the magnitudes (m_b) provided by the IPMA are equals to the ones calculated by the IGN. So, we consider $m_b = m_{bLg}$ for the conversions. The relations of Johnston (1996a) are chosen for the conversions. These empirical relationships are used to convert both teleseismic (Ms and M_L) and regional magnitudes to *M*0 (dyn cm) for stable continental crust earthquakes. The relationships are the followings:

$$log\ M_0 = 24.66 - 1.083\ M_S + 0.192\ M_S^2\ for\ M_S \geq 3.6 \quad (5.1)$$

$$log\ M_0 = 18.28 + 0.679\ mb + 0.077\ m_b^2 \quad (5.2)$$

Due to the small number of observed intensities (only 4), the 1909 December 8th and the 1912 January 23th earthquakes are not considered in this study.

For this study, the 1909 Benavente event will be considered as a reference because it is the most documented, owing to the preliminary work of Bensaude (1910) and the work of macroseismic field revision of Teves-Costa et al. (2010).

Here we only use epicentral distances because large uncertainties on the earthquake depths or the lack of value prevent to consider hypocentral distances. The definition of epicentral distances is essential. The intensity data point refers to a municipality and the location of this intensity data point is situated in the city center or city hall of this municipality. This may lead to an uncertainty in the calculation of the epicentral distance that depends on the municipality density. An area with a lot of municipalities will have more accurate intensity data point locations than an isolated municipality. The quality of the intensity data point itself is also controlled by this municipality density but also by the population density. Indeed, an isolated building located on a sedimentary basin, may suffer more important damage than the closest city, where this intensity observation will be associated. Moreover, the intensity data point for this city will be the one based on the damage statement of one isolated building or the testimony of the few people living there.

The intensity data points of each event of the table 5.1, are described in the chapter 12.

Table 5.1. Seismic events used to estimate the attenuation law;
IPMA: Instituto Português do Mar e da Atmosfera; ISC: International Seismological Center;
IGN: Instituto Geografico Nacional

Date	Latitude (°)	Longitude(°)	Magnitude	Type of M	Source	Mw	number of intensities	ID
23/04/1909	38,9	-8,8	6,0	Mw	Teves-Costa et al. 2010	**6,0**	504	1
04/05/1909	38,9	-8,8	4,5	mb	IPMA	**4,6**	20	2
11/06/1909	38,9	-8,8	5,0	mb	IPMA	**5,0**	14	3
17/08/1909	38,9	-8,8	5,2	mb	IPMA	**5,2**	17	4
08/12/1909	38,9	-8,8	5,2	mb	IPMA	**5,2**	4	5
09/02/1911	41,7	-8,9	5,0	mb	IPMA	**5,0**	7	6
12/08/1911	36,5	-7,8	4,8	mb	IPMA	**4,8**	17	7
23/01/1912	38,8	-7,8	5,0	mb	IPMA	**5,0**	4	8
11/07/1912	36,5	-7,8	5,0	mb	IPMA	**5,0**	18	9
18/10/1912	41,5	-8,5	5,0	mb	IPMA	**5,0**	36	10
27/10/1913	41,7	-8,7	5,0	mb	IPMA	**5,0**	18	11
23/09/1914	38,9	-8,8	5,3	mb	IPMA	**5,3**	12	12
25/09/1914	38,9	-8,8	5,3	mb	IPMA	**5,3**	83	13
11/07/1915	37,0	-10,5	6,2	Ms	ISC	**6,3**	71	14
02/03/1924	38,9	-8,8	5,0	mb	IPMA	**5,0**	17	15
28/02/1926	38,5	-8,0	5,5	mb	IPMA	**5,5**	104	16
10/02/1930	37,4	-8,1	5,0	mb	IPMA	**5,0**	38	17
25/11/1941	37,5	-18,5	8,4	Ms	Buforn et al. 1988	**8,7**	61	18
27/12/1941	36,0	-10,5	6,8	Ms	ISC	**6,7**	16	19
02/10/1947	38,5	-9,9	5,1	mb	IPMA	**5,1**	47	20
12/08/1948	40,1	-8,6	5,2	mb	IPMA	**5,2**	33	21
05/12/1960	35,6	-7,2	5,0	mb	IPMA	**5,0**	7	22
10/02/1961	41,5	-6,0	5,2	mb	IPMA	**5,2**	14	23
15/03/1964	36,1	-7,9	6,2	Ms	Buforn et al. 1995	**6,2**	81	24
28/02/1969	35,9	-10,9	8,0	Ms	Grandin et al. 2007	**8,2**	194	25
24/12/1969	36,0	-10	5,0	mb	ISC	**5,0**	7	26
14/06/1972	36,7	-8,4	5,2	mblg	IGN	**5,2**	20	27
04/04/1982	39,0	-10,3	4,4	mblg	IGN	**4,5**	16	28
10/08/1986	41,0	-7,2	4,3	mblg	IGN	**4,4**	41	29
21/05/1997	42,4	-7,2	5,2	mb	ISC	**5,2**	72	30

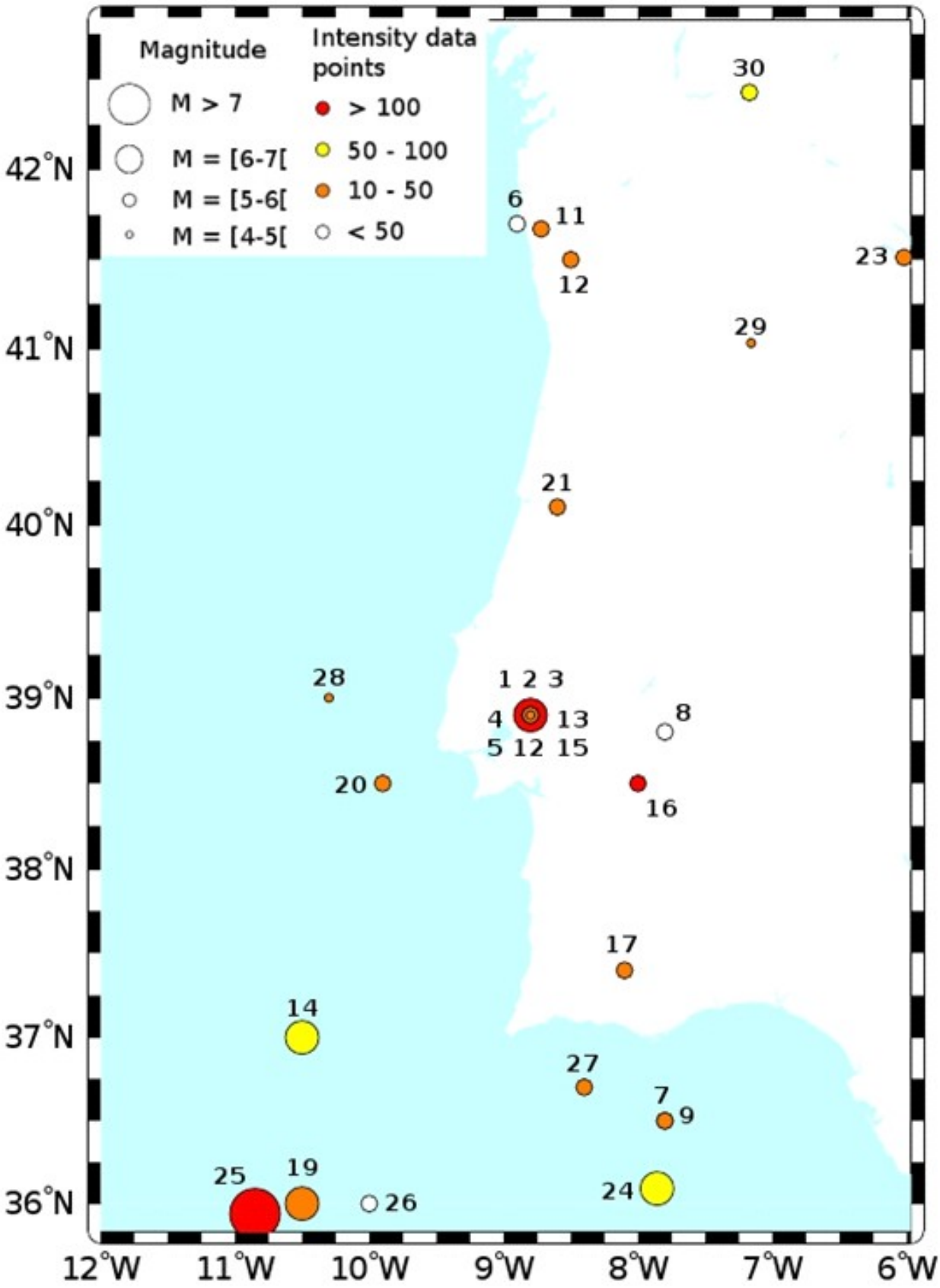

Figure 5.4: Map of the seismic events used to estimate the attenuation law (the 1941 earthquake of magnitude 8,4 is out of this map) (see table 1)

5.4.4. Attenuation equations

5.4.4.1 Equation form

In order to estimate the form of the attenuation law, several plots representing the intensity data points versus the epicentral distances, have been achieved for every earthquake. Different regression curves (linear, logarithmic and exponential) have been calculated to identify which one best fit the data (figure 5.5). This regression is achieved from the median epicentral distance of every intensity range, to avoid giving an important weight to the extreme values that might be erroneous or exaggerated.
Considering the regression coefficient, we obtained a mean value of 0.682 for the linear regressions, 0.693 for the exponential ones and 0.710 for the logarithmic ones. Some of the events provide few intensity data points or, for low magnitude events, intensity data points of same range. Taking into consideration the median value of the regression coefficients is more appropriate to give less weight to these events. The calculated median values correspond to 0.782 for the linear regressions, 0.801 for the exponential ones and 0.817 for the logarithmic regressions. According to these regression coefficients, the logarithmic regressions better fit the data, and are used to define the equation form.

This leads to an attenuation equation of the following form:

$$I = C_0(Mw)\,\ln(D) + C_1(Mw) \tag{5.3}$$

where I represents the intensity data point, M the magnitude and D the epicentral distance. C_0 and C_1 are the slope and the intercept of the attenuation law, respectively. So far, we do not know their dependency with the magnitude.

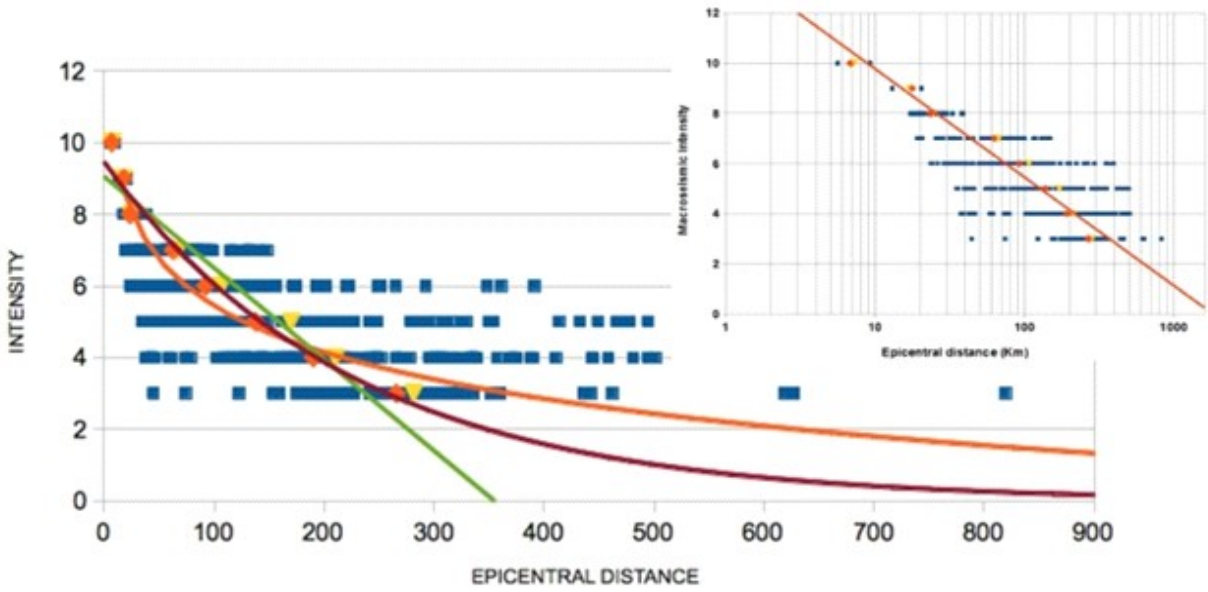

Figure 5.5: Intensity data versus Epicentral distance of the 1909 Benavente event. Blue dots represent intensity data. Yellow triangles and orange diamonds represent, respectively, the mean and median epicentral distance for each intensity range. The green, red and orange curves are, respectively, the linear, exponential and logarithmic regressions of the median epicentral distances. Plot in the top-right corner shows the best fit line of the logarithmic regression for the 1909 Benavente observed intensities.

5.4.4.2. Behavior of the parameters C_0 and C_1 related to the magnitude

To estimate the magnitude dependence of C_0, the slope of the logarithmic regression of each earthquake is plotted as a function of its related magnitude (figure 5.6). Note that the median slope is considered for same magnitude events. We observed that the slopes are constant for magnitude lower than 6.2 and seem to decrease for higher magnitudes. The same behavior is observed in figure 5.7, representing the intercepts of the logarithmic regression of each earthquake versus its related magnitude. The intercepts increase linearly for $M \leq 6.2$ and, increase with different coefficients for larger. If the constant slope and the linear increase of the intercepts for the $M < 6.2$ events are obvious, the linear trend of the decreasing slope and the increasing intercept, for $M \geq 6.2$, are not evident. This is due to the small number of events of $M \geq 6.2$, and to the lack of intensity data points of small epicentral distances, introducing large uncertainties in the calculation of both slope and intercept. We decided to restrain the attenuation law to the magnitude interval [4.4 – 6.2].

Constant slope and linear increase of intercepts lead to the following expressions of C_0 and C_1:

$$C_0(Mw) = C_0 \tag{5.4}$$

and

$$C_1(Mw) = k_1 Mw + k_2 \tag{5.5}$$

5.4.4.3. Attenuation laws

From the equation form and the expressions of its parameters, we can define the attenuation law.

The attenuation law is expressed as follow:

$$I = C_0 \ln(D) + k_1 Mw + k_2 \tag{5.6}$$

Using a weighted least-square fit we obtain the following expression:

$$I = -1.9438 \ln(D) + 4.1 Mw - 9.5763 \tag{5.7}$$

The standard deviation of the residuals is obtained comparing the obtained intensities from the previous attenuation relation with the observed intensities. We obtained a root mean square (RMS) standard error of 0.63. Concerning the parameters, the RMS are 0.37, 1.19 and 5.69 for the C_0, k_1 and k_2, respectively. The attenuation law is represented with all the data of $M \leq 6.2$ events in the figure 5.8, plotted for the magnitude 4.5, 5.0, 5.5 and 6.0.

The comparison between the observed and the theoretical intensities are expressed in the figure 5.9. We observed that the attenuation laws tends to underestimated the intensities lower than 5 and to overestimate the intensities larger than 5.

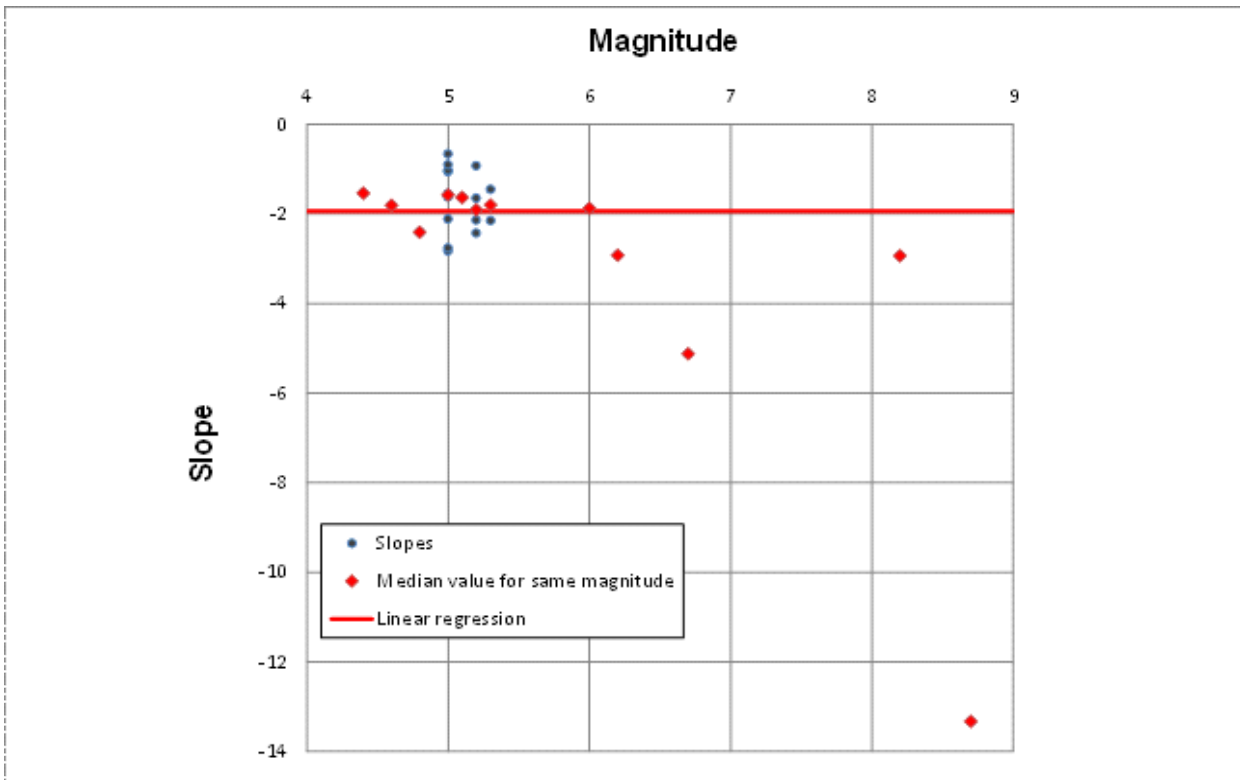

Figure 5.6: Slopes of the logarithmic regressions versus the magnitudes. The linear regression has been done using events of $M \leq 6.2$

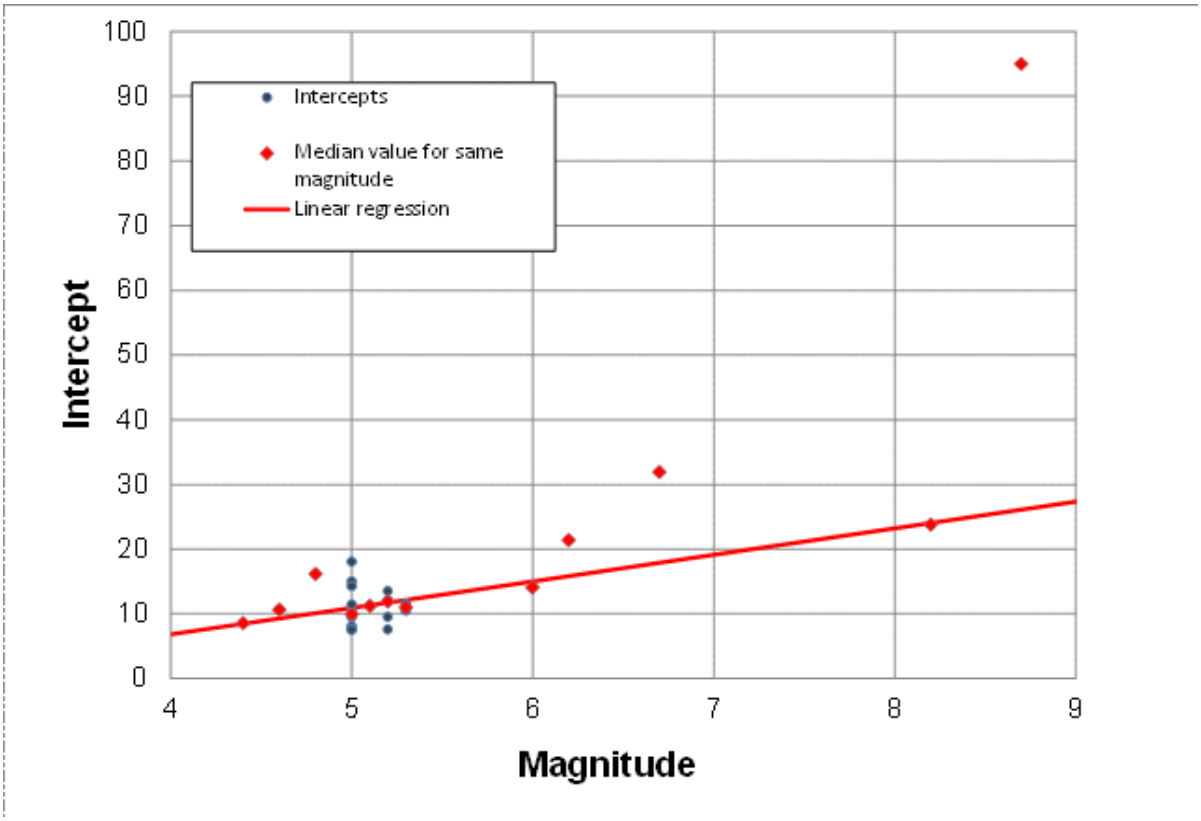

Figure 5.7: Intercepts of the logarithmic regressions versus the magnitudes. The linear regression has been done using events of $M \leq 6.2$

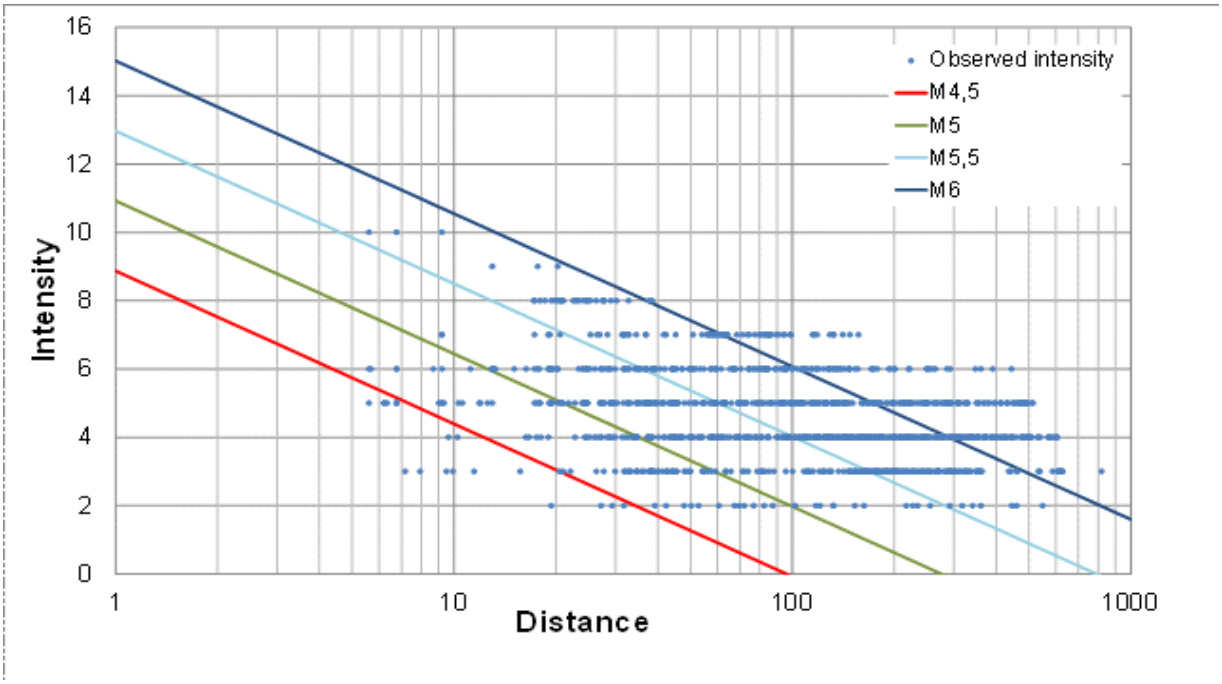

Figure 5.8: attenuation law plotted for M = 4.5, M = 5.0, M = 5.5 and M = 6.0

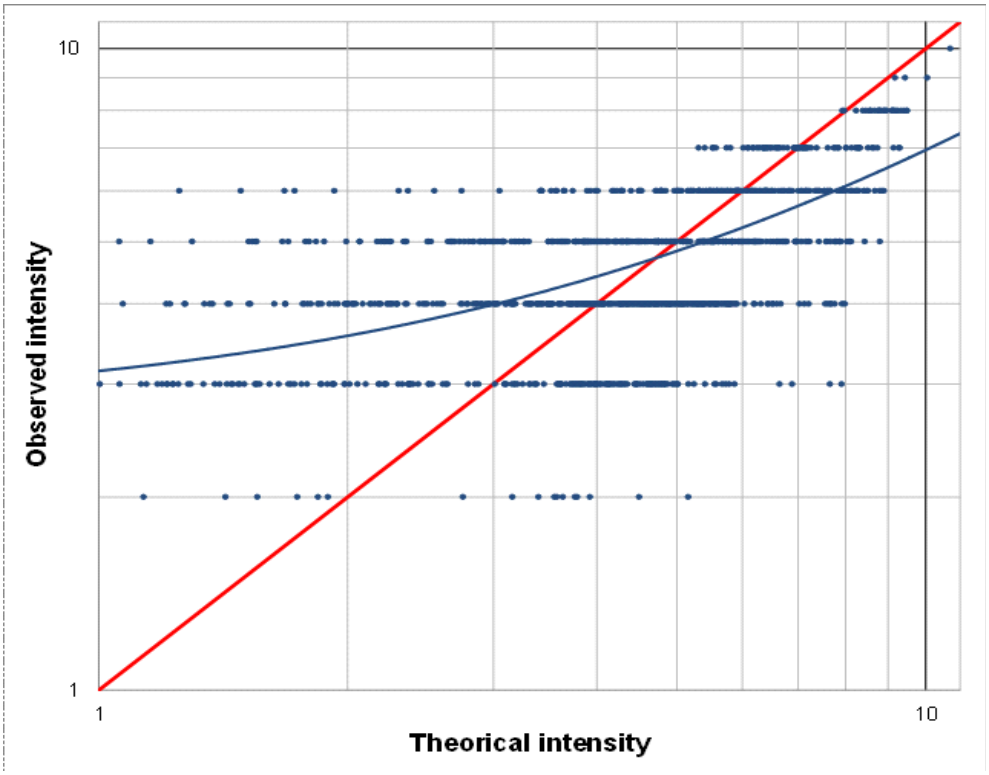

Figure 5.10: observed intensity versus theoretical intensity, obtained from the attenuation law. Red line represented the 1:1 trend line. Blue line represents the best fit line.

5.4.5 Comparison the Lopez-Casado et al. (2000) attenuation law

The attenuation law of Lopez-Casado et al. (2000) has been developed for the Iberian Peninsula. The comparison has been done for the 1909 Benavente event (Mw = 6.0) and are represented in the figure 5.11.

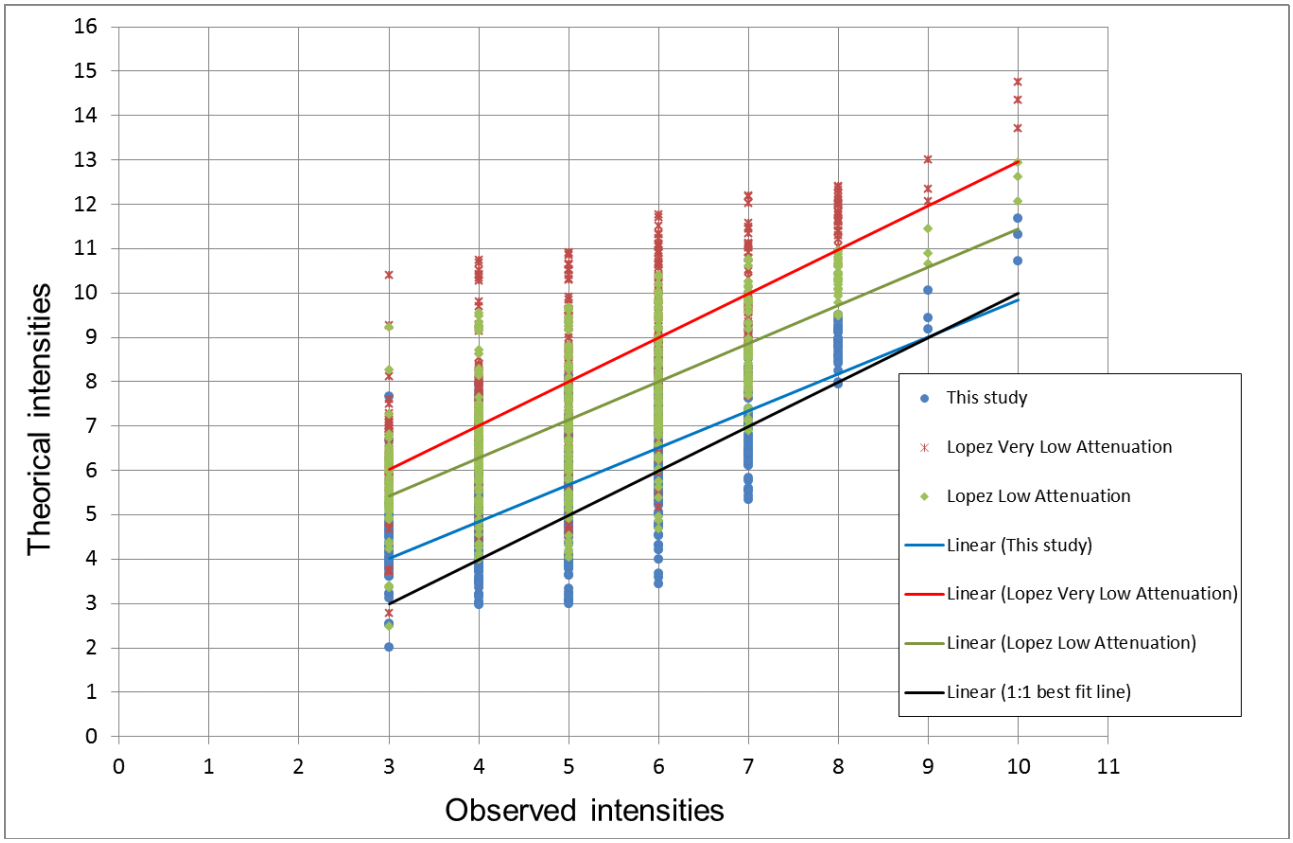

Figure 5.11: Comparison between the Lopez-Casado (2000) attenuation law (for low and very low attenuation) and the law developed in this study.

We observe that the new attenuation law better fits the data than the Lopez-Casado attenuation laws. The 1:1 best fit line represents the perfect attenuation model, where the theoretical intensities equal the observed intensities. Our attenuation law fits very well this line, considered as a reference.

5.4.6. Validation

5.4.6.1. Site effects

The computed attenuation law does not incorporate site corrections and site effects are not taken into account. By calculating the intensity residuals, ΔI, expressed as the difference between the observed intensities (I_{obs}) and the intensities calculated from the attenuation law (I_{theo}), we can study where they are situated and if they can be correlated with geological structures that present site effects. A positive value of ΔI expresses an underestimation of the theoretical value of the intensity I_{theo}, in regards to the observation value I_{obs}, explained by an amplification. These

intensity residuals may be represented through a Geographic Information System (GIS) with a map of the geological structures. The intensity residuals are then correlated to the topographic slope. Site effects are expected where the topographic slope is low.

We use this methodology with the 1909 Benavente event, which presents a large number of intensity data points with small epicentral distances (0-200 kilometers). The intensity residuals are interpolated and are represented in a GIS (QGIS) with the main basins of Portugal (figure 5.12). We expect positive values of the intensity residuals in the basins, expressing an effect of amplification. The study of Bezzeghoud et al. (2011) shows that the Portuguese meso-cenozoic basins (Lusitanian basin, Low Tagus basin, Arrabida basin and Algarve basin) are plausible regions for site effects.

The northern part of Portugal presents mainly negative intensity residuals, with few positive ones near the ocean. In the central part, the intensity residuals are mainly positives. Some negative values are located in the occidental part of Lisbon, with low punctual residuals around the Tagus river mouth. The southern part is clearly dominated by negative intensity residual values, except some positive values detected in the region of Algarve.

From the intensity residual interpolation map, we may clearly delimitate the different geological structures. The positive values match well with the limits of the meso-cenozoic basins, where site effects were already highlighted. We can also isolate the South Portuguese zone and the central Iberian zone, where the intensity residuals are negatives, from the Ossa-Morena zone where intensity residuals are positives. In the south Portuguese zone and in the Central Iberian Zone the negative intensity residuals are best explained by the bedrock made of consolidated rocks (mainly granites). No explanations may explain the positive values of the Ossa-Morena zone as this zone is also mainly composed of granites and should present negatives intensity residuals, because of the high velocity of the seismic wave propagation. The Algarve basin is evidenced by positive values. Even if no limits can be made up between the Lusitanian basin and the Low Tagus basin, both of them can be extracted from the other formations. In spite of the few data in the Arrabida basin, it is possible to differentiate this basin from the Low Tagus basin. The large negative residual values detected around the Tagus river mouth highlight the volcanic complex of Lisbon. Indeed, the fast propagation of seismic waves into volcanic rocks leads to negative intensity residual values. The negative residuals observed in the north-west of Lisbon may be explained by the presence of relief, limiting the rule of the geologic site effects. Unfortunately the lack of data in Spain prevents the intensity residual interpolation map to be interpreted.

A cross-section has been achieved and is represented in the figure 5.13. The part of the graphic with low elevation and low topographic slope corresponds to the Low Tagus basin. We observe a connection between the elevation and topographic slope with the intensity residuals. Positive values are found at the level of the basin, while negative values are observed in the part with higher elevation and slope. This confirms the correlation of the positive intensity residuals with the site effects in the meso-cenozoic basins. Nevertheless, we observe another patch of positive intensity residuals, between the kilometers 35 and 45 of the cross-section. Even if few of these intensity residuals may be explained by the intensity location problem, this concentration of positive residuals may be related to the basin edge effect (Choi et al. 2005, Paolucci and Morstabilini 2006) or by a transition zone (change of rock composition).

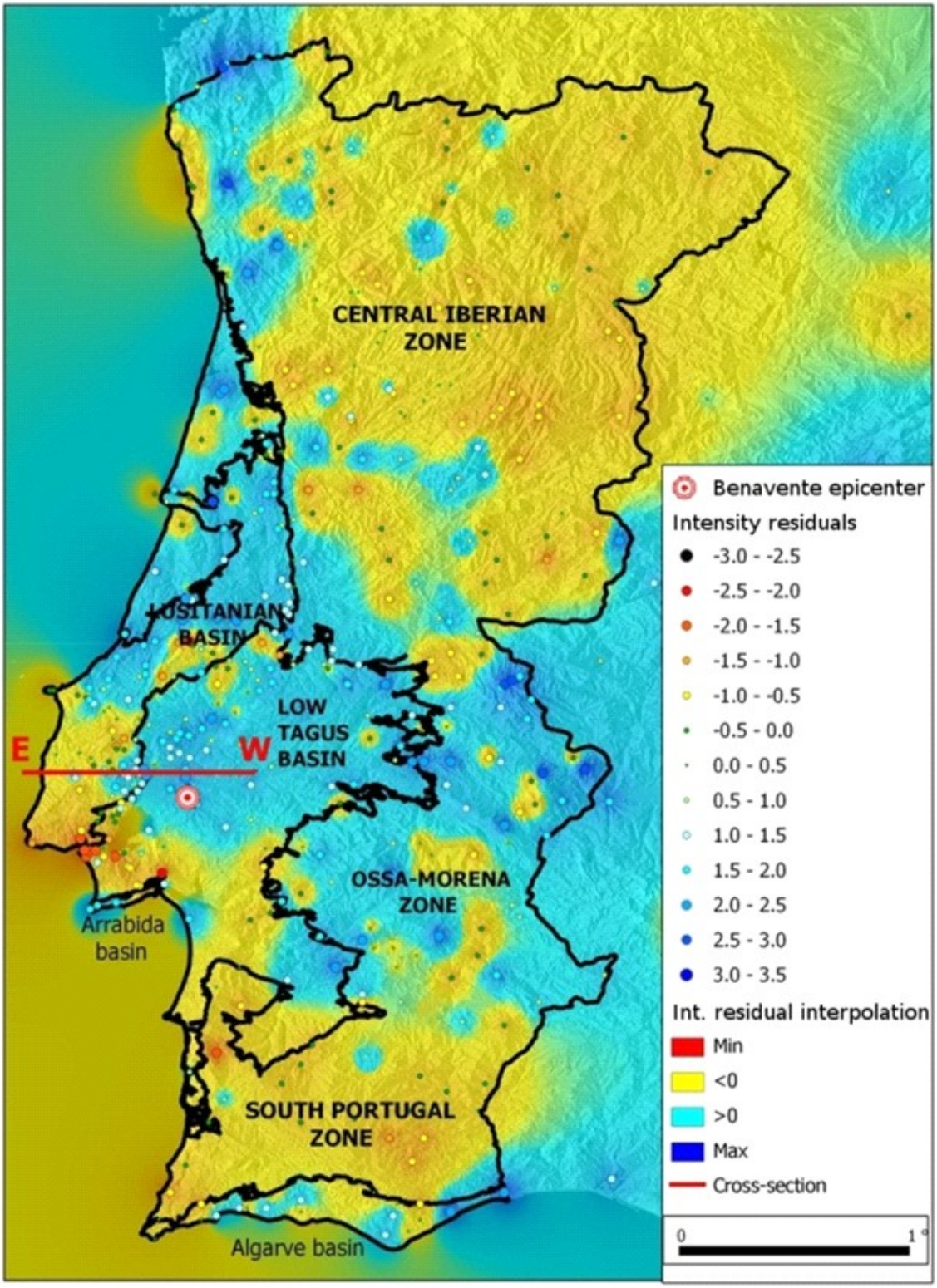

Figure 5.12: Intensity anomalies map and their interpolation. Cross-section represented in the figure 5.13

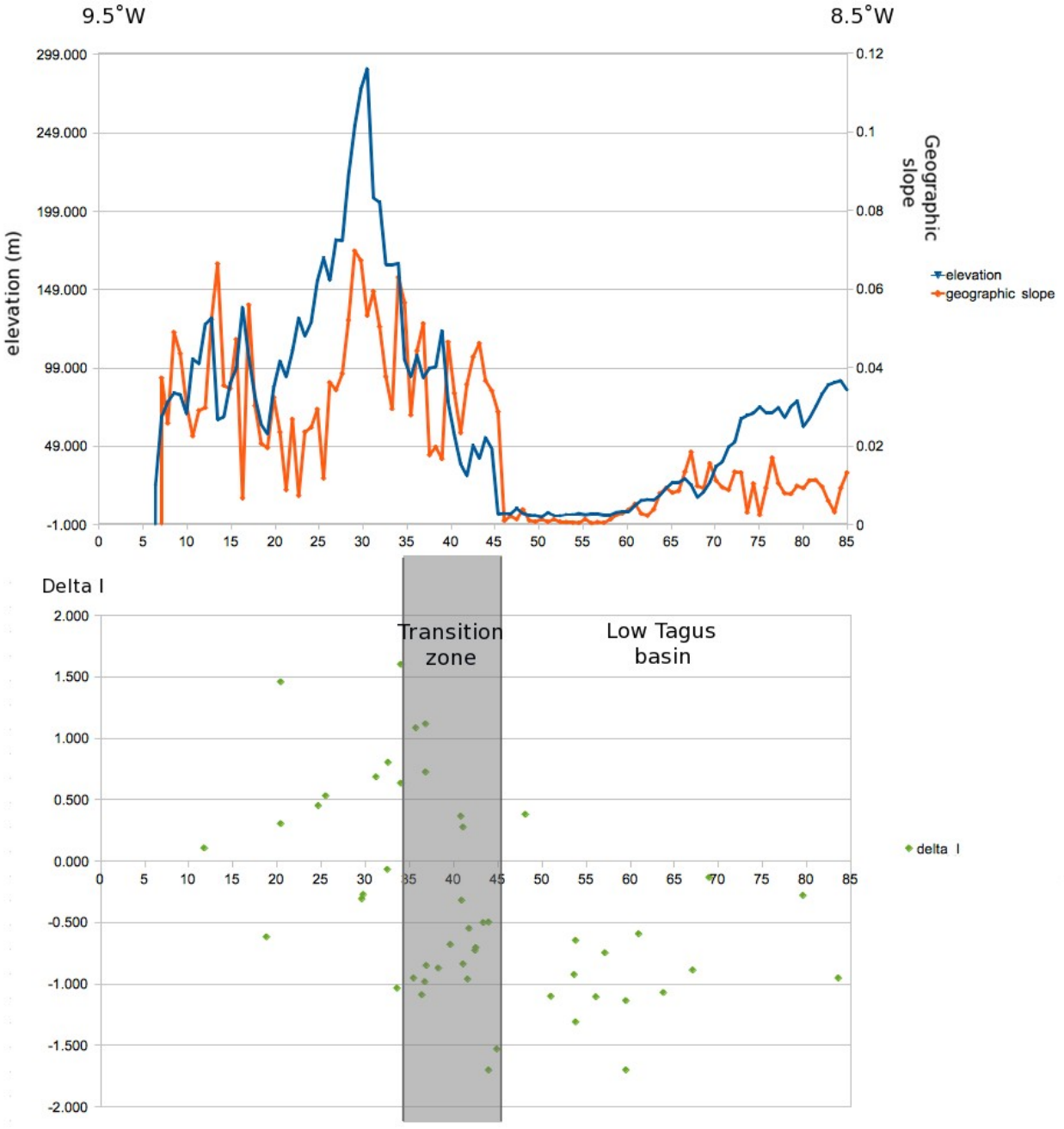

Figure 5.13: relation between the topographic slope, the elevation and the intensity anomalies. Cross-section between the longitudes -9.5˚ and -8.5˚ at the latitude 39˚N. The orange curve represents the topographic slope along the profile. The blue curve represents the elevation along the profile. Green dot represents the intensity anomaly. Cross-section located in figure 5.12

5.5. Re-estimation of the epicentral region and magnitude of the 1909 Benavente event

Using the attenuation law developed in this study, we re-estimated the epicentral region and the magnitude of the 1909 Benavente event with the Bakun and Wentworth method (1997). The resulting map is presented in the figure 5.14 with the previous results obtained using the Atkinston and Boore (1997) attenuation law.

First, we observe that we obtained a magnitude estimation of M=6.1 (figure 5.14, right side). This is slightly larger than the instrumental magnitude (M_w=6.0), but better than the estimation done with the Atkinson and Boore (1997) law. We also notice that the Karnik (1969) estimation is still within all the confidence level contours.

The minimum of rms[M_I] is getting closer to the Karnik (1969) estimation and the confidence level contours become closers. The N-W extension, presented in the first resulting map (figure 5.14, left side), disappeared.

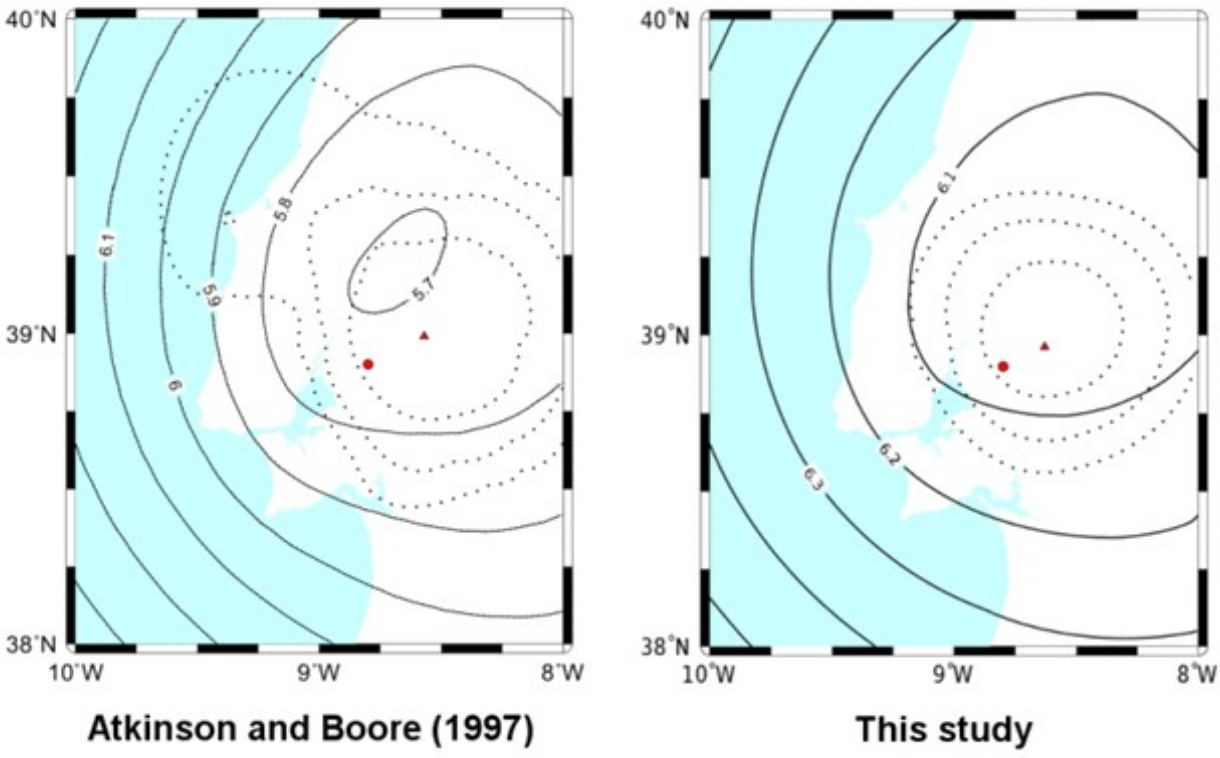

Figure 5.14: Resulting magnitude and earthquake epicentral position of the 1909 Benavente event, using the Bakun and Wentworth method (1997) with the Atkinston and Boore (1997) attenuation law (left side) and the attenuation law computed in this study (right side). Solid lines represent the contours of M. The red dot represents the epicenter estimated by Kárník (1969). The red triangle represents the location of the minimum value of rms[M_I] over a grid of assumed epicenters. The rms[M_I] contours corresponding to the 50%, 80% and 95% confidence levels for location are shown as the innermost, middle, and outermost contours of the dotted lines, respectively.

From these results, we can conclude that the use of the computed attenuation law, appropriate for this region, allows performing better resulting maps of earthquake location and magnitude estimations. Indeed, the most significant improvement, using this attenuation law, is the estimation of the magnitude that is in good agreement with the instrumental one, while the one defined with the Atkinston and Boore (1997) attenuation law underestimates it (figure 5.14, left side). We also observe a better earthquake location with a tightening of the confidence level contours and a minimum of rms[M_I] coming closer to the epicenter estimation of Kárník (1969).

5.6. Discussion

The relocation of the 1909 Benavente event with the Bakun and Wentworth method (1997), gives us an epicentral region estimation with confidence levels, related to the number of intensity data points. The location of historical earthquake uses to be estimated from isoseismal lines, set up by expert decisions, and expressed as a macroseismic epicenter. We recommend incorporating epicentral region of historical earthquakes with the corresponding confidence levels (pdf) into PSHA calculations rather than the macroseismic epicenters. Such large earthquakes are essential in the definition of seismotectonic zoning and should not be considered as point sources.

The data used to compute the attenuation laws are few and, sometimes, of poor quality; only six earthquakes of $M \geq 6.2$ have been used, with only one event intensity data points having epicentral distances lower than 200 kilometers. This lack of nearby intensity data is explained by the offshore location of largest earthquakes. Because of the offshore position of these events, the uncertainties related to their location and magnitude calculation are considerable.
The intensity data estimation also contributes to the uncertainty in the attenuation law. As the location of an intensity data is associated to the closest municipality, the calculated epicentral distance corresponds to the distance between the earthquake epicenter and this municipality, and not the location of the observed intensity itself. According to the municipality density, this association may contribute to large uncertainties. Moreover, this intensity may be exaggerated if it results from a single testimony or a single damage statement.

Even if this attenuation laws present good results with the Bakun and Wentworth method (1997), or with the study of site effects, more steps of validations are required before using it into a Probabilistic Seismic Hazard Analysis. The attenuation law needs to be adapted according to different soil conditions. The map of residual intensities can be used to detect regions where site effect studies are suitable. Then, local site amplification effects will be accounted for by using empirical corrective coefficients.

Indeed, to use in PSHA calculation, the calculated intensities needs to be convert into spectral accelerations that may lead to largest uncertainties. After the intensity to acceleration conversion, the empirical accelerations need to be compared with accelerometer data.

5.7. Conclusion

A new method for computing attenuation law for the Portugal mainland has been presented in this paper. This method uses the intensity observations directly, rather than the areas enclosed by

isoseismal lines, made up by subjective expert decisions. The significant advantage in using individual intensity observations directly is that the procedures are explicit so that the results are reproducible. Another improvement of this attenuation law is that it is expressed as a function of the magnitude.

From the logarithmic regression of each collected event and the study of their slope and intercept behavior with the magnitude, we obtained the following attenuation law:

$$I = -1.9438 \ ln(D) + 4.1 \ M_w - 9.5763$$

The range of validity corresponds to moment magnitude values between 4.4 and 6.2. So far this attenuation law may be used in Portugal mainland, but can be extend to a wider area by incorporating additional events of stable region (e.g., additional events from Spain to obtain an attenuation law for use in the Iberian Peninsula).

Using the new attenuation law with the methodology of Bakun and Wentworth (1997), we obtained better results in the 1909 Benavente earthquake epicentral position and magnitude estimation, than the use of the Atkinston and Boore (1997) attenuation law. We reached to a magnitude estimation of 6.1 for the 1909 Benavente event that is close to the instrumental one.

Table 5.2: locations and magnitudes of the 1909 Benavente event

	Latitude	Longitude	Magnitude
Kárník (1969)	38.9˚	-8.8˚	$M_S = 6.6$
Teves-Costa et al. (1999)	-	-	$M_w = 6.0$
This study	38.99˚	-8.61˚	$M_w = 6.1$

This attenuation law does not consider the site effects. Comparing the intensity observations of the 1909 Benavente event to the ones computed with the attenuation, we can detect regions of amplification. The positive intensity residuals, considered as amplified intensities, match really well with the meso-cenozoic basins, known for their potential site effects. These local site amplification effects can be accounted for by using empirical corrective coefficient.

CHAPTER 6

Discussion

During about 20 years, the evolution of PSHA in current practice has been slowed down by using paying software within which code source is not known and shared. But recently, initiatives have been undertaken, first in California with openSHA and after in international-wide with GEM, to propose an open source code, making it easier to incorporate new methodologies. The methodology, presented in this thesis, could therefore be inserted in the hazard calculation process.

The intervention of panels of experts, that was used in first attempts at assessing epistemic uncertainties, needs to be transformed and moved "upstream" whenever it is possible. The expert decisions may be incorporated as priors and avoid using expert decisions.

The evolutions of PSHA leads to modifications into the risk models insurance. As example, the European Commission implemented the Solvency II directive to introduce economic risk-based solvency requirements across all EU Member States. Solvency II is currently scheduled for introduction in 2014. It defines catastrophe risk as "the risk of loss, or of adverse change in the value of insurance liabilities, resulting from significant uncertainty of pricing and provisioning assumptions related to extreme or exceptional events" (Cf. Solvency II Directive 2009/138/EC of 25 November 2009, Art. 105 2 (b).). In the fifth quantitative impact study, insurance companies were able to test two valuation methods (Solvency Consulting Knowledge Series "QIS5: European Commission publishes instructions for fifth Quantitative Impact Study"):

- Method 1: standard scenarios
- Method 2: factor-based approach

Method 1 draws a distinction between natural catastrophes and man-made catastrophes. First, the capital requirements for each peril are aggregated at country level to determine the catastrophe risk capital per peril. Then, the capital requirements are aggregated using a correlation matrix. This produces the natural catastrophe risk capital according to Method 1. The natural catastrophe risk capital and the risk capital for man-made catastrophes should then be aggregated on the assumption that they are independent of each other.
Method 2 is factor-based, the capital requirement being calculated by multiplying a risk factor by a volume figure. The risk factors relate to individual events. The volume figure is calculated by apportioning the gross premiums written for a business segment to the events.
Model providers, such as EQECAT (Company of risk management) or RMS (Risk Management Solutions), need to prepare documentation on the methodology underlying their suite of natural catastrophe peril models to support Solvency II compliance. A particular emphasis will need to be put in the treatment of the uncertainties, both aleatory (data driven) and epistemic (model driven).

With our contribution, we show how Bayesian Inference would be useful in earthquake source modeling. Other authors have pointed that out in the recent past, for renewal models (Biasi and Weldon, 2008; Fitzenz and al, 2007), or for a general view (Esmer, 2006).
Nevertheless, only data from seismicity catalogs are used in our model, reducing the zoning to a seismic zoning. Geological data (e.g., alluvial zones, granitic uplands), structural data (e.g., fault orientations, fault lengths, focal mechanisms) but also complementary seismicity data (e.g., paleoseismicity) have to be incorporated into this model. All additional data will improve the resolving power of this method, reducing the minimum number of data, n_{min}, required in a seismicity catalog to recover the geographical limit between the two zones and their respective surface activity rates.
Moreover, this Bayesian model is restricted to two different zones. It is important to consider a model with an undefined number of zones.
The method of Bender (1986) may be adapted in order to calculate the seismicity rates. The limit

uncertainty, obtained with the Bayesian inference, may be used to smooth the seismicity activity rate in the source zone boundaries.

In more recent studies, like the third version of Uniform California Earthquake Rupture Forecast (UCERF3, 2012), the polygonal area zones are mainly used to defined the maximum magnitude and to express the fault characteristics. The resulting fault zone polygon is composed by a combination of a geologic polygon, the fault surface projection and the fault trace buffer. Nevertheless, the concept of polygon zone sources differs from previous studies, where all the parameters where deemed homogeneous. Indeed, the a-values of the Gutenberg-Richter frequency-magnitude law are calculated on a grid, with Gaussian smoothing kernels (UCERF2, Field 2009) or an adaptive smoothing algorithm in which the kernel width depends on data density (UCERF3 and based on Helmstetter et al., 2007). The b-values of the Gutenberg-Richter law are calculated from a group of polygon zones to obtain enough large magnitudes to get slopes with a larger robustness. The results are smoothed and the seismicity is concentrated where its already occurred.

The relocation of historical events using the Bakun and Wentworth method (1997), provide an epicentral region with uncertainties corresponding to any desired level confidence, related to the number of intensity data points. We recommend incorporating epicentral region of historical earthquakes with the corresponding confidence levels (pdf), into PSHA calculation, rather than the macroseismic epicenters obtained from subjective isoseismal lines. The method of Bakun and Wentworth (1997) would be useful in earthquake source modeling and coherent with the requirements of the Solvency II directive.
However we need to be aware of the large uncertainties that the attenuation law may provide to the epicentral region estimation with this method. The example of the 1909 Benavente event shows improvements in the estimation of its epicentral region when a more appropriated attenuation law is used, even if it was developed with few data.
Even if this attenuation laws present good results with the Bakun and Wentworth method (1997), or with the study of site effects, more steps of validations are required before using it into a Probabilistic Seismic Hazard Analysis. The attenuation law needs to be adapted according to different soil conditions. The map of residual intensities can be used to detect regions where site effect studies are suitable. Then, local site amplification effects will be accounted for by using empirical corrective coefficients.

Indeed, to use in PSHA calculation, the calculated intensities needs to be convert into spectral accelerations that may lead to largest uncertainties. After the intensity to acceleration conversion, the empirical accelerations need to be compared with accelerometer data.

CHAPTER 7

Conclusion

To resolve the shortcomings implied with the use of subjective methods, as the current methodology to define the seismotectonic zoning, we propose in this thesis a new approach in area source modeling. This approach is reproducible and preserves the information on the source and extent to the uncertainties, allowing propagating them.

A Bayesian inference with two seismic zones, differentiated by a contrast of surface seismicity rate, was performed to obtain the geographic limit between them (chapter 4). According to the ratio between the seismicity rate of each zone, we can estimate the minimum number of data, n_{min}, required in a earthquake catalog to recover the geographical limit between the two zones. The number of data in an earthquake catalog varies as a function of the observation period and as a function of seismicity activity. The results obtained from synthetic catalogs, which are drawn from a poissonian model (temporal model), a uniform spatial distribution and a truncated exponential model (frequency-magnitude model), show that, for an observation period of 100 years, the ratio between the seismicity rate of each zone has to be larger than 3 to obtain a acceptable geographical limit between the 2 zones. Considering an observation period of 1000 years, this ratio is reduced to 1.5, because of the higher number of data. The geographic limit is obtained with its related uncertainty and is not considered as finite boundary anymore. Once we obtain this optimal value of the geographical limit, we can recover the surface activity rates of each zone, with a quantitative measure of the uncertainty (including covariance).

In this Bayesian model, the earthquake locations are essential. The instrumental location of earthquakes may be improved using the method of the double-difference (Waldhauser and L. Ellsworth, 2000). The historical earthquakes have a large impact in the PSHA calculations and, in particularly, in the definition of the seismic sources. They are directly implied in the definition of the limit between the two zones but, above all, in the definition of the seismicity parameters of each zones (e.g., seismicity activity rates, parameters of the magnitude-frequency relationship, definition of the Maximum Credible Earthquake). So, it is primordial to locate these events with the best accuracy possible. The method of Bakun and Wentworth (1997) allows estimating the epicentral region and the moment magnitude of an historical earthquake, directly from its intensity data points rather than its isoseismal lines. The significant advantage in using individual intensity observations directly is that the procedures are explicit so that the results are reproducible. The results of such a method provide an estimation of the epicentral region with levels of confidence appropriated for the number of intensity data points used.
As example, and because of its controversial location, estimated from its isoseismal lines that present particular shapes (Mezcua, 1982; Senos et al., 1994; Teves-Costa and Batlló, 2010), this methodology was applied to the 1909 Benavente event. A new location of the 1909 Benavente event had been presented in this study (chapter 5.5). The epicentral region of this event is expressed with confidence levels related to the number of intensity data points.

This epicentral region and magnitude estimations of the 1909 Benavente event were improved by the development of a new intensity-distance attenuation law for the Portugal mainland (chapter 5.4). This law is expressed as a function of the magnitude rather than the epicentral intensity I_0.

From the logarithmic regression of each event, we obtained the equation form of the attenuation law. We obtained the following attenuation law:

$$I = -1.9438\ \ln(D) + 4.1\,Mw - 9.5763 \quad \text{for } 4.4 \leq \text{Mw} \leq 6.2$$

Using these attenuation laws, we reached to a magnitude estimation of the 1909 Benavente event that is in good agreement with the instrumental one. The epicentral region estimation was also improved with a tightening of the confidence level contours and a minimum of rms[M_I] coming closer to the epicenter estimation of Kárník (1969).

This attenuation law does not consider the site effects and it is possible to highlight regions of seismic amplification. The negative intensity anomalies, considered as amplified intensities, match really well with the meso-cenozoic basins, known for their potential site effects.

Finally, this 2 zone model will be a reference in the comparison with other models, which will incorporate other available data. Future improvements need to be achieved to obtain a seismotectonic zoning. This model needs to integrate structural data (e.g., fault orientation, fault length) and geological data as well. This will allow reducing the minimum number of data, n_{min}, required in an earthquake catalog to recover the activity rates of both zones and the geographical limit between them, with some confidence. Also, this model needs to be extended to a number n of zones with an unspecified shape.

We emphasize that such an approach is reproducible once priors and data sets are chosen. Indeed, the objective is to incorporate expert opinions as priors, and avoid using expert decisions. Instead, the products will be directly the result of the inference, when only one model is considered, or the result of a combination of models in the Bayesian sense.

CHAPTER 8

Annex 1: Synthetic Catalogs: Matlab code

The synthetic catalogs are achieved using the usual models, even if some of them are questionable. These catalogs are drawn from a Poisson model as temporal model, from a uniform spatial model and from the truncated Gutenberg-Richter law for the magnitude distribution.

The algorithm is computed with Matlab:

```
clear all

M=[4:0.0001:6]; % magnitude vector
Mmax=6; %Mmax used in this study
Mmin=4; %Mmin used in this study
bet=1.5;  %bet=b*ln10 (parameter of the Gutenberg-Richter law)


lamb0_S_1=3e-4;  % Surface activity rate zone 1
lamb0_S_2=1e-4;  % Surface activity rate zone 2


Tobs=100; %Observation period (500, 1000, 2000, 10000 years)
nbrealisation=100; % number of catalog realization
% study area size
Lx_max=60;
Ly_max=30;
x_lim=20; % limit between the two zones
lamb0_1=lamb0_S_1*(Ly_max*x_lim); % activity rate zone 1
lamb0_2=lamb0_S_2*(Ly_max*(Lx_max-x_lim)); % activity rate zone 2

mat_X=zeros(100000,nbrealisation);
mat_Y=zeros(100000,nbrealisation);
mat_EchM=zeros(100000,nbrealisation);
mat_t=zeros(100000,nbrealisation);




for nbreal=1:nbrealisation

clear t_1
clear x_1
clear y_1
clear EchM_1
clear t_2
clear x_2
clear y_2
clear EchM_2
```

```
% Zone 1

%1_ time sampling

delta_T=[0:0.0001:50];

P=1-exp(-lamb0_1*delta_T); % probability to have, at least, one event during the time interval
delta_T


%figure(1)
%plot(delta_T,P,'+')
%xlabel('delta T')
%ylabel('cdf')


i=1;
t_1(1)=0.5;
t_total_1=0;

while (t_total_1<Tobs)

r=rand(1,1);
diff=abs(P-r);
[val,ind]=min(diff);


Ech_delta_T_1(i)=delta_T(ind);
EchP_1(i)=P(ind);

 t_1(i+1)=t_1(i)+Ech_delta_T_1(i);

   t_total_1=t_1(i+1);

   i=i+1;
end

t_1=t_1(1:length(t_1)-1);

%hold on
%plot(Ech_delta_T_1,EchP_1,'r+')

%figure (2)
%hist(Ech_delta_T_1,50)
%xlabel('delta t')
%ylabel('nombre de tirages')


N_1=length(t_1); % number of events
```

```
% 2_ Spatial distribution

% x and y samplings

r=rand(1,N_1); % drawn from uniform distribution
x_1=r.*x_lim; % values of x
r=rand(1,N_1); % drawn from uniform distribution
y_1=r.*30;  % values of y

%figure(3)
%plot(x_1,y_1,'.')
%xlabel('x')
%ylabel('y')



%3_ Magnitude sampling

Ediff=exp(-bet*(Mmax-Mmin));
PmSupM=((exp(-bet*(M-Mmin))-Ediff)./(1-Ediff)); % troncated G-R law

A=exp(bet*Mmin)/(1-exp(-bet*(Mmax-Mmin)));
B=-exp(-bet*(Mmax-Mmin))/(1-exp(-bet*(Mmax-Mmin)));

lamb_1=lamb0_1*PmSupM; % occurrence model of earthquakes (annual number of events >= M)

cdfPmSupM=1-PmSupM;


%figure (4)
%plot(M,cdfPmSupM,'.')



for i=1:N_1

r=rand(1,1);

diff=abs(cdfPmSupM-r);

[val,ind]=min(diff);

sval=size(val);

if max(sval)>1 max(sval)
end

EchM_1(i)=M(ind);
EchCdf_1(i)=cdfPmSupM(ind);
end
```

```
%hold on
%plot(EchM_1,EchCdf_1,'+r')
%ylabel('cdf');
%xlabel('magnitude')


% verification and dispersion

bins=[4.1:0.1:6];

[h, binpos]=hist(EchM_1,bins);

hnew(1)=sum(h);
for i=2:length(bins);

    hnew(i)=hnew(i-1)-h(i-1);


end

%figure (5)
%plot(M,log(lamb_1*Tobs))
%xlabel('Magnitude')
%ylabel('log (nombre d evenements sup?rieurs ou ?gaux ? Mmin)')
%%hold on
%plot(binpos,log(hnew),'r*','markersize',4)


% zone 2

delta_T=[0:0.0001:50];


P=1-exp(-lamb0_2*delta_T);

%figure(6)
%plot(delta_T,P,'+')
%xlabel('delta T')
%ylabel('cdf')

i=1;
t_2(1)=0.7;
t_total_2=0;

while (t_total_2<Tobs)

r=rand(1,1);
diff=abs(P-r);
[val,ind]=min(diff);
```

```
Ech_delta_T_2(i)=delta_T(ind);
EchP_2(i)=P(ind);

 t_2(i+1)=t_2(i)+Ech_delta_T_2(i);

   t_total_2=t_2(i+1);

   i=i+1;
end

t_2=t_2(1:length(t_2)-1);

%hold on
%plot(Ech_delta_T_2,EchP_2,'r+')

%figure(7)
%hist(Ech_delta_T_2,50)
%xlabel('delta t')
%ylabel('nombre de tirages')


N_2=length(t_2);


% 2_ Saptial distribution


r=rand(1,N_2);
x_2=r.*(Lx_max-x_lim)+x_lim;
r=rand(1,N_2);
y_2=r.*30;

%figure(8)
%hold on
%plot(x_2,y_2,'r.')


%3_ Magnitude Sampling

Ediff=exp(-bet*(Mmax-Mmin));
PmSupM=((exp(-bet*(M-Mmin))-Ediff)./(1-Ediff));

A=exp(bet*Mmin)/(1-exp(-bet*(Mmax-Mmin)));
B=-exp(-bet*(Mmax-Mmin))/(1-exp(-bet*(Mmax-Mmin)));

lamb_2=lamb0_2*PmSupM;

cdfPmSupM=1-PmSupM;
```

```
%figure(9)
%plot(cdfPmSupM,M,'.')



for i=1:N_2

r=rand(1,1);

diff=abs(cdfPmSupM-r);

[val,ind]=min(diff);

sval=size(val);

if max(sval)>1 max(sval)
end

EchM_2(i)=M(ind);
EchCdf_2(i)=cdfPmSupM(ind);
end


%hold on
%plot(EchCdf_2,EchM_2,'+r')
%xlabel('cdf');
%ylabel('magnitude')



% verification and dispersion

bins=[4.1:0.1:6];

[h, binpos]=hist(EchM_2,bins);

hnew(1)=sum(h);
for i=2:length(bins);

   hnew(i)=hnew(i-1)-h(i-1);


end

%figure(10)
%plot(M,log(lamb_2*Tobs))
%xlabel('Magnitude')
%ylabel('log (number of events larger than Mmin)')
%hold on
%plot(binpos,log(hnew),'r*','markersize',4)
```

```
%4_Sub_Catalog

nx1=length(x_1);
mat_X1(1:nx1,1)=x_1;
ny1=length(y_1);
mat_Y1(1:ny1,1)=y_1;
nEchM1=length(EchM_1);
mat_EchM1(1:nEchM1,1)=EchM_1;
nt1=length(t_1);
mat_t1(1:nt1,1)=t_1;

Subcat1=[mat_X1,mat_Y1,mat_EchM1,mat_t1];
Subcat1=Subcat1(1:length(x_1),:);


nx2=length(x_2);
mat_X2(1:nx2,1)=x_2;
ny2=length(y_2);
mat_Y2(1:ny2,1)=y_2;
nEchM2=length(EchM_2);
mat_EchM2(1:nEchM2,1)=EchM_2;
nt2=length(t_2);
mat_t2(1:nt2,1)=t_2;

Subcat2=[mat_X2,mat_Y2,mat_EchM2,mat_t2];
Subcat2=Subcat2(1:length(x_2),:);

Cat_rea=[Subcat1;Subcat2];
Cat_rea=sortrows(Cat_rea,4);


nevent=length(Cat_rea(:,1));
Cat_2Z_Sept(1:nevent,4*nbreal+1)=Cat_rea(:,1);
Cat_2Z_Sept(1:nevent,4*nbreal+2)=Cat_rea(:,2);
Cat_2Z_Sept(1:nevent,4*nbreal+3)=Cat_rea(:,3);
Cat_2Z_Sept(1:nevent,4*nbreal+4)=Cat_rea(:,4);

end


%figure(11)
%plot(x_1,y_1,'.r')
%hold on
%plot(x_2,y_2,'.b')
%hold on
%plot(x_lim,1:1:30)
%xlabel('x')
%ylabel('y')

save ('Catal_2Z_Sept2011_100rea.txt', 'Cat_2Z_Sept', '-ascii')
```

CHAPTER 9

Annex 2: Bayesian inference to recover the limit between the 2 zones: Matlab code

According to the graphical model (figure 4.4), we obtained a expression of the joint probability (equation 4.18) to recover the geographical limit between the two zones. An easier way of representing the Bayesian inference results is as a energy function (equation 4.31).

The algorithm used to computed the Bayesian inference to recover the limit between the two zones is described, in the Matlab language, as follow:

```
clear all

load ('-ascii','Catal_2Z_Sept2011_100rea.txt')

% dimensions of the study area
Lx_max=60;
Ly_max=30;
nbrealisation=100;  % number of catalogs

U2=0;

x_lim=10:1:60;  % vector of the limit between the two zones
lambda_S1=3e-4;
lambda_S2=1e-4;
opt=0;

for nrea=1:nbrealisation

    clear x
    clear y
    clear M
    clear t
    clear M2



x=Catal_2Z_Sept2011_100rea(:,4*nrea+1);
y=Catal_2Z_Sept2011_100rea(:,4*nrea+2);
M=Catal_2Z_Sept2011_100rea(:,4*nrea+3);
t=Catal_2Z_Sept2011_100rea(:,4*nrea+4);

    for i_M=1:length(M)
        if (M(i_M)~=0)
            M2(i_M)=M(i_M) ;
        end
    end

 nevent=length(M2);
```

```
Cat_rea=[x(1:nevent),y(1:nevent),M(1:nevent),t(1:nevent)];


for indx_lim=1:length(x_lim)
SubCat_1=[0,0,0,0];
SubCat_2=[0,0,0,0];

for i=1:nevent

   if (x(i)<x_lim(indx_lim))
      SubCat1=Cat_rea(i,:);
      SubCat_1=[SubCat_1;SubCat1];
   else
      SubCat2=Cat_rea(i,:);
      SubCat_2=[SubCat_2;SubCat2];
   end

end

SubCat_1=SubCat_1(2:end,:);
SubCat_2=SubCat_2(2:end,:);


t_1=SubCat_1(:,4);
t_2=SubCat_2(:,4);


n1=length(SubCat_1(:,1));
n2=length(SubCat_2(:,1));

delta_t_1=0;
delta_t_2=0;

for i=1:n1-1
   delta_t_1(i)=t_1(i+1)-t_1(i);
end

for i=1:n2-1
   delta_t_2(i)=t_2(i+1)-t_2(i);
end

S1=sum(delta_t_1);
S2=sum(delta_t_2);

n=length(SubCat_1(:,1));
m=length(SubCat_2(:,1));


log_Priors=log(1/(Lx_max*1e6));
```

```
% -log of the joint pdf

U=-log_Priors-n*log(lambda_S1)+lambda_S1.*x_lim(indx_lim).*Ly_max*S1-
m*log(lambda_S2)+lambda_S2.*(Lx_max-x_lim(indx_lim)).*Ly_max*S2;


U2(indx_lim)=U;



end
[val,ind]=min(U2);

opt=[opt,x_lim(ind)];


hold on
plot(10:1:60,U2,'+')
xlabel('limite en x')
ylabel('Energie')

end

opt=opt(2:end);
binpos=[min(opt):1:max(opt)];

[f,h]=hist(opt,binpos);
hold off
figure(2)
bar(h,f/sum(f))
xlabel('optimal value of the limit (Km)')
ylabel('frequency')


% uncertainty


incert=1./sqrt(abs((-n./(opt.^2))-(m./((opt-Lx_max).^2))));

%binpos2=[min(incert):0.05:max(incert)];
%[f,h]=hist(incert,binpos2);
%hold off
%figure(2)
%bar(h,f/sum(f))
%xlabel('uncertainty')
%ylabel('frequency')
```

CHAPTER *10*

Annex 3: Bayesian inference to recover the surface activity rate of each zone: Matlab code

Once we obtain an optimal value for the limit, we can evaluate both surface seismicity rates (Figure 4.11 and 4.12).
The algorithm used to computed the Bayesian inference to recover the surface seismicity rates is described, in the Matlab language, as follow:

```
clear all


load ('-ascii','Catal_2Z_Sept2011.txt')
x=Catal_2Z_Sept2011(:,1);
y=Catal_2Z_Sept2011(:,2);
M=Catal_2Z_Sept2011(:,3);
t=Catal_2Z_Sept2011(:,4);


lamb0_S_1=0.1e-4:0.5e-4:2.02e-3;  % vector surface activity rate zone 1
lamb0_S_2=0.1e-4:0.1e-4:4.1e-4;    % vector surface activity rate zone 2


Lx_max=60;
Ly_max=30;

x_lim=20; % optimum of the inference on the limit


SubCat_1=[0,0,0,0];
SubCat_2=[0,0,0,0];

for indx=1:1:length(x)


   if (x(indx)<x_lim)
      SubCat1=Catal_2Z_Sept2011(indx,:);
      SubCat_1=[SubCat_1;SubCat1];
   else
      SubCat2=Catal_2Z_Sept2011(indx,:);
      SubCat_2=[SubCat_2;SubCat2];
   end

end


SubCat_1=SubCat_1(2:end,:);
SubCat_2=SubCat_2(2:end,:);


t_1=SubCat_1(:,4);
t_2=SubCat_2(:,4);
```

```
n1=length(SubCat_1(:,1));
n2=length(SubCat_2(:,1));

delta_t_1=0;
delta_t_2=0;

for i=1:n1-1
   delta_t_1(i)=t_1(i+1)-t_1(i);
end

for i=1:n2-1
   delta_t_2(i)=t_2(i+1)-t_2(i);
end

S1=sum(delta_t_1);
S2=sum(delta_t_2);

n=length(SubCat_1(:,1));
m=length(SubCat_2(:,1));


log_Priors=log(1/(Lx_max*1e6));



for i=1:1:length(lamb0_S_1)

   for j=1:1:length(lamb0_S_2)

% -log of the marginal distribution of the joint pdf with respect to x_lim

logPj=-log_Priors-n*log(lamb0_S_1(i))+lamb0_S_1(i).*x_lim.*Ly_max*S1-m*log(lamb0_S_2(j))
+lamb0_S_2(j).*(Lx_max-x_lim).*Ly_max*S2;



log_Pj(i,j)=logPj;

   end

end


pcolor(lamb0_S_1,lamb0_S_2,log_Pj)

shading('interp')

colormap(jet)
colorbar
```

CHAPTER 11

Annex 4: Intensity data points of the 1909 Benavente event (from Teves-Costa and Batlló, 2010)

This annex presents the intensity data points of the 1909 Benavente event, after macroseismic field revision (Teves-Costa and Batlló, 2010).

Locality / Site	Lat (º)	Lon (º)	Intensity (MM)
Abela (Nossa Senhora)	38.001	-8.560	IV
Abrantes	39.467	-8.200	V-VI
Abrigada	39.145	-9.019	VII
A-dos-Francos (Rio Maior)	39.317	-9.050	VI-VII
Águeda	40.567	-8.450	IV
Aguim	40.417	-8.450	V-VI
Alandroal (Estremoz)	38.700	-7.400	V
Alcácer do Sal	38.371	-8.520	V
Alcains	39.917	-7.450	IV
Alcalá de Guadaira	37.333	-5.833	IV
Alcalá de Henares	40.483	-3.367	III-IV
Alcanena	39.459	-8.669	V
Alcanhães (ou Alcanhões)	39.296	-8.660	VI
Alcaria (Minde)	39.567	-8.783	III
Alcaria Ruiva	37.700	-7.783	IV
Alcobaça	39.550	-8.983	VII
Alcobertas	39.417	-8.900	IV
Alcochete	38.756	-8.960	VII-VIII
Alcoentre	39.209	-8.960	VII
Alcofra	40.617	-8.183	IV-V
Alcuescar	39.185	-6.235	V
Aldeacentenera	39.533	-5.633	IV-V
Aldeia do Bispo	40.117	-7.167	IV
Aldeia do Mato	39.533	-8.267	V-VI
Aldeia Galega (Merceana)	39.105	-9.100	VI
Aldeia Galega (Montijo)	38.684	-8.896	VII
Aldeia Nova (de São Bento)	37.917	-7.417	IV
Alegrete	39.233	-7.317	VI
Alenquer	39.055	-9.011	VII-VIII
Alfeizeirão	39.500	-9.100	VI-VII
Alferrarede	39.483	-8.167	VI
Algoz	37.167	-8.300	IV-V
Alhadas	40.183	-8.783	IV
Alhandra	38.924	-9.009	VIII
Aljezur	37.317	-8.800	IV
Aljubarrota	39.567	-8.933	VII
Almada	38.680	-9.159	V-VI
Almagro	38.883	-3.715	V
Almeirim	39.213	-8.627	VII-VIII
Almodovar	37.517	-8.067	IV
Almoster (Santarem)	39.233	-8.800	VII
Alpalhão	39.417	-7.617	IV
Alpiarça	39.260	-8.585	VI
Alqueva	38.217	-7.533	IV
Alter do Chão	39.200	-7.667	V
Alva	40.850	-7.967	IV
Alvados	39.550	-8.767	V
Alvaiazere	39.833	-8.383	V-VI
Alvega	39.467	-8.050	VI
Alvendre	40.583	-7.267	III
Alverca	38.891	-9.034	VIII
Alvito	38.250	-7.983	V

Alviubeira (Zêzere)	39.683	-8.352	VI
Alvor	37.133	-8.567	IV-V
Amares	41.633	-8.350	II
Amiães de Baixo	39.433	-8.733	VII
Amoreiras (Beja)	37.667	-8.383	IV
Areias (Zêzere)	39.733	-8.350	VI
Arez	39.483	-7.733	IV
Arganil (Coimbra)	40.217	-8.050	IIII
Armamar	41.000	-7.700	I
Arroyo de la Luz	39.483	-6.581	V-VI
Arruda dos Vinhos	38.999	-9.068	VII-VIII
Asseiceira	39.508	-8.392	IV
Aveiras de Baixo	39.111	-8.869	VIII
Aveiras de Cima	39.138	-8.900	VIII
Aveiro	40.633	-8.650	VI
Aviz	39.057	-7.891	VI
Azambuja	39.067	-8.867	VIII
Azaruja	38.700	-7.783	V
Azinhaga	39.348	-8.530	VI
Azoia (Sesimbra)	38.433	-9.183	VI-VII
Badajoz	38.879	-6.961	V-VI
Baião (Porto)	41.150	-8.033	III
Bailén	38.100	-3.775	III
Bairros (Sobrado de Paiva)	41.033	-8.233	III-IV
Barbacena	38.967	-7.300	IV
Barca d'Alva	41.017	-6.933	II-III
Barcelona	41.383	2.183	II
Barcelos	41.533	-8.617	V-VI
Barquinha	39.450	-8.433	VI-VII
Barrancos	38.133	-6.983	IV-V
Barreiro	38.658	-9.067	V-VI
Batalha	39.659	-8.815	VII
Beja	38.017	-7.867	V
Belalcázar	38.567	-5.167	IV-V
Bélmez	38.267	-5.200	IV-V
Belmonte (Castelo Branco)	40.350	-7.350	III
Benavente	38.983	-8.800	X
Benavila	39.117	-7.867	VII
Benedicta	39.427	-8.975	VI-VII
Benfica	39.142	-8.689	VII
Bensafrim	37.150	-8.733	III
Bombarral	39.266	-9.153	V-VI
Borba	38.776	-7.416	VI-VII
Bordeira	37.200	-8.867	III
Boticas (Vila Real)	41.683	-7.667	III
Bouro (Parada do)	41.650	-8.267	IV
Braga	41.550	-8.433	III-IV
Brenha	40.200	-8.933	IV
Brotas	38.871	-8.130	V
Buarcos	40.167	-8.883	IV-V
Bucelas	38.902	-9.118	VI-VII
Bujalance	37.905	-4.383	V-VI
Burguillos (del Cerro)	38.383	-6.538	III
Cabanas de Torres	39.150	-9.068	V

Cabeção	38.952	-8.071	VI-VII
Cabo Carvoeiro	39.357	-9.390	V
Cabo Espichel	38.417	-9.215	VI-VII
Cabrela (Évora)	38.599	-8.462	V
Cáceres	39.474	-6.377	IV-V
Cachoeiras (Carregado)	38.983	-9.017	VII
Cachopo (Faro)	37.333	-7.817	III
Cadafais	39.005	-9.001	VIII
Cadaval (Lisboa)	39.233	-9.100	V-VI
Cadiz	36.534	-6.299	IV
Caldas da Rainha	39.404	-9.136	VI-VII
Calhandriz (S. Marcos)	38.925	-9.066	VIII
Caminha	41.867	-8.833	V
Campo Maior	39.017	-7.067	VI-VII
Canha	38.769	-8.626	VII-VIII
Cardosas	38.983	-9.050	VIII
Carmões (S. Domingos de)	39.050	-9.133	VI
Carnaxide	38.719	-9.257	IV
Carneiros (Alenquer)	39.017	-9.117	VI
Carregado	39.017	-8.983	IX
Carreiras	39.367	-7.433	V-VI
Carril	39.599	-8.352	VII
Cartaxo	39.162	-8.786	VIII
Carvalhães	40.067	-8.817	IV
Carvalhal (Leiria)	39.283	-9.133	V-VI
Castanheira	38.990	-8.972	IX
Castelo Branco	39.817	-7.500	IV
Castelo de Penalva	40.667	-7.650	IV
Castendo	40.667	-7.700	IV
Castro Daire	40.900	-7.933	IV
Ceclavín	39.817	-6.767	V
Celorico (da Beira)	40.633	-7.383	III
Ceras (Zêzere)	39.700	-8.367	VI
Cercal (Montejunto)	39.233	-9.000	VI
Cercal (Setúbal)	37.800	-8.667	III
Chamusca (Almeirim)	39.356	-8.480	VI-VII
Chança (Aldeia da Mata)	39.250	-7.817	VI
Charneca (da Caparica)	38.617	-9.183	VII
Chaves	41.733	-7.467	III-IV
Ciudad Real	38.979	-3.933	V
Ciudad Rodrigo	40.607	-6.536	IV
Coimbra	40.200	-8.417	V-VI
Coina	38.600	-9.051	V
Columbeira (Leiria)	39.300	-9.200	VII
Comporta	38.375	-8.786	VII
Condeixa	40.117	-8.500	V
Constância	39.467	-8.333	VI
Córdova	37.883	-4.767	V-VI
Coria (Cáceres)	39.985	-6.536	IV-V
Corroios	38.643	-9.155	V
Cortegana (Lisboa)	39.117	-9.100	V
Coruche	38.950	-8.517	VII-VIII
Costa da Caparica	38.642	-9.232	IV
Cova da Piedade	38.674	-9.156	V-VI

Covilhã	40.283	-7.500	IV-V
Crato e Mártires	39.283	-7.650	V-VI
Cuba	38.167	-7.883	V
Dafundo (Cruz Quebrada)	38.700	-9.250	II
Degolados (Campo Maior)	39.067	-7.117	IV
Don Benito (Badajoz)	38.954	-5.866	V-VI
Eiras	40.250	-8.417	VI
El Puerto de Santa Maria	36.600	-6.233	IV
Elvas	38.883	-7.167	VI
Entradas (Aljustrel / Almodovar)	37.783	-8.017	V
Erada	40.217	-7.650	IV-V
Ereira (Pontevel)	39.178	-8.867	VII
Erra (Coruche)	39.029	-8.429	VI-VII
Ervedal	39.050	-7.817	VII
Escoural (S. Tiago do)	38.533	-8.167	VI
Escusa	39.383	-7.417	VI-VII
Esgueira	40.650	-8.633	VI
Esposende	41.533	-8.783	III
Estoi	37.100	-7.900	V
Estremoz	38.850	-7.583	VI
Évora	38.567	-7.900	VI-VII
Fafe	41.450	-8.167	III
Fão	41.517	-8.767	III
Faro	37.017	-7.933	V
Fataunços	40.517	-8.083	III
Feira	40.917	-8.550	IV-V
Fernan-Núñez	37.667	-4.717	III-IV
Ferreira (do Alentejo)	38.050	-8.033	VI
Ferreira do Zêzere	38.683	-8.292	VI
Figueira (e Barros)	39.050	-7.767	VII
Figueira de Castelo Rodrigo	40.900	-6.967	II
Figueiró	41.306	-8.344	III
Figueiró dos Vinhos	39.907	-8.289	VI
Freixiandra	39.761	-8.456	V-VI
Freixo de Espada-à-Cinta	41.083	-6.817	III-IV
Fronteira	39.050	-7.650	VI-VII
Galveias	39.150	-8.000	V
Gavião	39.267	-8.300	VII
Golegã	39.401	-8.487	VI
Gondomar (Porto)	41.150	-8.533	VI
Gouveia (Guarda)	40.500	-7.600	III
Gradil	38.980	-9.279	VI-VII
Granada	37.183	-3.600	IV
Grândola	38.167	-8.567	IV-V
Granjal	40.883	-7.533	IV
Guarda	40.533	-7.267	III
Guia (Faro)	37.117	-8.300	III-IV
Guimarães (Braga)	41.450	-8.300	V
Hervás	40.267	-5.850	IV-V
Huelva	37.258	-6.951	V
Idanha-a-Nova	39.917	-7.233	III
Igrejinha	38.700	-7.900	VI
Jaén	37.771	-3.794	IV
Jaraiz	40.083	-5.769	V

Jerez de la Frontera	36.683	-6.131	IV
Jódar	37.843	-3.354	IV-V
Juromenha	38.733	-7.233	VI
La Rambla	37.600	-4.733	IV
Lagoa	37.133	-8.450	V
Lagos	37.100	-8.667	IV-V
Lavre (Sto Estevão)	38.800	-8.517	VII
Lazareto (Setúbal)	38.667	-9.217	IV
Leiria	39.750	-8.800	VII
Linhares (Guarda)	40.533	-7.467	III
Lisboa	38.717	-9.133	V
Lora (del Rio)	37.657	-5.534	IV-V
Lorca (Murcia)	37.667	-1.700	III
Loures	38.830	-9.167	VI
Lousã	40.117	-8.250	V
Louzada	41.267	-8.283	IV
Lovelhe (V. Nova Cerveira)	41.950	-8.750	IV
Luso	40.383	-8.383	IV
Madrid	40.400	-3.683	IV-V
Málaga	36.717	-4.417	IV
Malhada Sorda	40.533	-6.917	III
Malpica	39.683	-7.400	IV
Malveira	38.929	-9.260	IV-V
Mangualde (Viseu)	40.600	-7.767	IV
Manteigas	40.400	-7.533	IV-V
Martimlongo (Faro)	37.433	-7.767	II
Marvão	39.400	-7.383	VII
Mealhada	40.367	-8.450	IV
Meca (Lisboa)	39.000	-9.000	VIII
Meda	40.967	-7.267	III
Melgaço	42.117	-8.267	II-III
Mértola	37.633	-7.667	IV
Messejana	37.833	-8.250	IV
Miajadas	39.150	-5.900	IV-V
Milagres (Leiria)	39.791	-8.792	V
Mina de S. Domingos	37.667	-7.500	IV
Minde	39.517	-8.683	V
Mira	40.433	-8.733	IV
Mira (Leiria/ Porto Mós)	39.533	-8.733	VI
Miranda do Corvo	40.090	-8.331	IV-V
Mirandela	41.483	-7.183	III
Mogofores	40.450	-8.467	V
Moimenta (da Beira)	40.983	-7.617	IV
Moita	38.655	-8.994	VI-VII
Moledo (Viana do Castelo)	41.850	-8.850	I
Mombeja	38.017	-8.033	IV
Monção	42.083	-8.483	IV-V
Moncarapacho	37.083	-7.783	IV
Moncorvo (Torre de)	41.167	-7.050	III
Monforte	39.050	-7.433	VI
Monforte (Monfortinho)	40.000	-6.917	V-VI
Monsaraz	38.433	-7.383	V
Montalvão	39.600	-7.533	V
Monte da Caparica	38.668	-9.190	IV

Montemor-o-Novo	38.650	-8.217	VI-VII
Montemor-o-Velho	40.167	-8.683	VI-VII
Mora (Coruche)	38.944	-8.166	VI-VII
Mortágua	40.400	-8.233	V-VI
Moura (Beja)	38.133	-7.450	VI
Mourão	38.383	-7.350	V
Muge (ou Mugem)	39.100	-8.711	VIII
Nandufre	40.533	-8.084	IV-V
Navalmoral (de la Mata)	39.885	-5.545	V
Nave Redonda (Guarda)	40.867	-6.917	II
Nazaré	39.599	-9.064	VII
Nellas	40.533	-7.850	IV
Niza	39.517	-7.650	IV
Noura	41.383	-7.417	IV
Óbidos	39.362	-9.157	VI
Odemira	37.600	-8.633	V
Odivelas (Beja)	38.167	-8.150	VI-VII
Odivelas (Lisboa)	38.793	-9.183	VI
Oitavos (Lisboa)	38.700	-9.467	IV
Oleiros (Castelo Branco)	39.917	-7.917	III-IV
Olhalvo	39.101	-9.067	VI
Olhão	37.033	-7.833	IV
Olho-Marinho	39.326	-9.231	V
Oliveira de Azeméis	40.833	-8.483	III-IV
Oliveira de Frades	40.733	-8.183	III
Oliveira do Bairro	40.517	-8.500	IV
Oliveira do Hospital	40.350	-7.867	IV-V
Oña (Burgos)	42.733	-3.400	II
Ourém	39.657	-8.580	VII
Paços de Ferreireira	41.267	-8.400	VI
Palencia	42.017	-4.533	III-IV
Palhacana (Lisboa)	39.050	-9.133	VI
Palma (Portalegre)	39.067	-7.483	IV
Palma del Rio	37.703	-5.294	IV-V
Palmela	38.572	-8.903	IV
Pampilhosa (da Serra)	40.050	-7.950	III-IV
Panóias (Beja)	37.750	-8.300	IV
Parceiros (Santarém)	39.450	-8.617	V
Paredes de Coura	41.900	-8.567	IV
Payalvo (ou Paialvo)	39.560	-8.468	IV
Pedrógão (Beja)	38.122	-7.646	IV
Peñarroya	38.300	-5.267	V
Penha Garcia	40.033	-7.017	III
Peniche	39.357	-9.374	V
Pernes	39.384	-8.662	V
Pias (Santarém)	39.917	-8.333	IV-V
Pinheiro Grande (Chamusca)	39.391	-8.425	VI-VII
Pó	39.317	-9.219	VII
Podentes (Penela)	40.050	-8.400	VI
Poiares (Coimbra)	40.217	-8.267	III
Pomarão	37.550	-7.533	IV
Pombal (Leiria)	39.917	-8.633	VI
Ponte de Lima	41.767	-8.583	IV
Ponte de Sor	39.248	-8.010	VI

Pontevedra	42.416	-8.656	IV
Pontevel (Cartaxo)	39.149	-8.840	VIII
Portalegre	39.283	-7.433	VI
Portel	38.300	-7.700	VI-VII
Portela do Braz (Santarém)	39.800	-8.333	V
Portimão	37.133	-8.533	IV
Porto	41.150	-8.617	IV
Porto de Mós	39.600	-8.817	VI-VII
Pousa Foles (Viana do Castelo)	42.100	-8.183	III
Pousafoles (Pudente/Penela) (Coimbra)	40.067	-8.383	V
Pousos (Leiria)	39.744	-8.775	VI
Póvoa (de Santa Iria)	38.850	-9.067	V-VI
Póvoa de Lanhoso	41.583	-8.267	IV
Póvoa e Meadas	39.510	-7.516	IV
Povos (Lisboa)	38.967	-8.983	VII-VIII
Prado	41.600	-8.467	III
Proença-a-Nova	39.750	-7.917	III-IV
Proença-a-Velha	40.017	-7.233	IV
Puente del Arzobispo	39.804	-5.169	III-IV
Pussos (Zêzere)	39.807	-8.356	V-VI
Queluz	38.755	-9.253	V
Querença	37.200	-7.983	III-IV
Quiaios	40.217	-8.850	VI
Ranhados (Viseu)	40.633	-7.900	III
Raposa	39.124	-8.564	VII
Redondo	38.650	-7.550	IV
Refoios	41.733	-6.900	III
Refugidos	39.017	-9.017	VIII
Régua (Peso da)	41.167	-7.783	III-IV
Reguengo (Santarém)	39.067	-8.783	VII-VIII
Resende (Viseu)	41.100	-7.967	III
Riachos	39.447	-8.516	VI
Ribafria	39.416	-9.001	VI
Ribaldeira (Lisboa)	39.033	-9.200	VI
Ribeira de Niza	39.652	-7.655	V-VI
Rio Caldo	41.683	-8.183	II
Rio Maior	39.337	-8.936	VI
Rocio (Rossio ao Sul do Tejo)	39.450	-8.183	V
Runa	39.067	-9.210	VI
S. Bartolomeu	39.383	-7.933	VI-VII
S. Braz (S. Brás de Alportel)	37.150	-7.883	IV
S. Cristóvão	38.483	-8.300	V
S. Fagundo	39.382	-8.098	VI-VII
S. Fiel	40.033	-7.500	IV-V
S. Francisco da Serra	38.083	-8.667	V
S. João da Talha	38.826	-9.092	VI
S. João dos Montes	38.940	-9.020	VII
S. Julião	39.317	-7.300	V-VI
S. Marcos do Campo	38.333	-7.517	IV
S. Martinho do Bispo	40.200	-8.450	VI
S. Miguel de Machede	38.650	-7.733	V
S. Miguel do Pinheiro	37.550	-7.833	IV
S. Pedro da Cadeira	39.081	-9.362	VI
S. Pedro do Sul	40.750	-8.067	IV

S. Quintino (Lisboa)	39.000	-9.150	VII
S. Sebastião (dos Carros)	37.555	-7.772	IV
S. Teotónio	37.500	-8.700	IV
S. Tiago dos Velhos	38.942	-9.105	VIII
S. Tiago Maior	38.567	-7.467	IV-V
Sacavem	38.791	-9.107	VI
Sagres	37.000	-8.933	III-IV
Salamanca	40.965	-5.663	III
Salamonde (Braga)	41.683	-8.083	IV
Salamonde (Viana do Castelo)	41.667	-8.583	IV
Salgueirães (ou Salgueirais)	40.567	-7.433	III
Salorino (Cáceres)	39.483	-7.000	IV-V
Salvaterra de Magos	39.017	-8.800	IX
Samora Correia	38.933	-8.867	X
Sant' Anna da Serra	37.500	-8.300	IV
Santa Catarina (Faro)	37.150	-7.783	II
Santa Catarina de Sítimos	38.400	-8.433	IV-V
Santa Comba Dão	40.400	-8.133	IV
Santa Cruz (Beja)	37.433	-7.917	II
Santa Eulália	39.000	-7.250	VI-VII
Santa Iria (da Azóia)	38.850	-9.083	VIII
Santa Margarida (do Sado)	38.112	-8.358	VI
Santa Maria (de Machede)	38.583	-7.783	V
Santa Susana	38.583	-7.653	V
Santa Susana (Setúbal)	38.450	-8.383	VI-VII
Sant'Anna da Carnota	39.034	-9.072	VIII
Santarem	39.236	-8.687	VII-VIII
Santiago (de Compostela)	42.883	-8.550	III
Santo António das Areias (Castelo Vide)	39.417	-7.350	VI
Santo Estevão	38.867	-8.750	IX-X
Santo Tirso	41.342	-8.470	III
Santo Varão	40.183	-8.600	IV
Sardoal	39.533	-8.160	VI
Seda	39.183	-7.783	V
Segovia	40.950	-4.117	IV
Seixal	38.643	-9.107	IV
Senhora da Luz (Faro)	37.083	-8.733	IV
Sernache (ou Cernache)	40.133	-8.473	VI
Serpa	37.933	-7.600	V
Serpins	40.117	-8.250	III-IV
Serra d'El Rei	39.336	-9.269	IV-V
Serra Ventoso	39.560	-8.829	IV
Serraquinhos	41.800	-7.667	II
Setubal	38.525	-8.893	VI-VII
Sever (do Vouga)	40.733	-8.367	III
Sevilla	37.377	-5.987	IV-V
Sezimbra	38.445	-9.102	VI-VII
Silves	37.183	-8.433	IV
Sinfães (Braga)	41.500	-8.167	III
Sinfães (Viseu)	41.067	-8.083	IV
Sobral (da Adiça - Beja)	38.017	-7.267	IV-V
Sobral (do Campo)	40.000	-7.567	IV-V
Sobral de Monte Agraço	39.018	-9.152	VII
Soure	40.050	-8.633	VI

Sousel (ou Souzel)	38.950	-7.667	VI
Tábua	40.350	-8.033	V-VI
Tabuaço	41.117	-7.567	II
Talavera de la Reina	39.959	-4.825	IV
Talhadas	40.667	-8.333	III
Tavira	37.117	-7.650	VI
Telões (Vila Real)	41.450	-7.683	II
Tendais	41.067	-8.050	IV
Terrugem (Santo António da)	38.833	-7.350	IV
Tolosa	39.417	-7.717	IV
Tomar	39.604	-8.413	VI
Tondela	40.517	-8.083	III
Torrão	38.300	-8.217	VI-VII
Torrão (Setúbal)	38.293	-8.226	VI
Torres Novas	39.480	-8.541	VI
Torres Vedras	39.088	-9.260	VI
Tortosa	40.800	0.517	I
Trafaria	38.670	-9.239	IV
Turleque	39.600	-3.600	V
Turquel	39.464	-8.974	VI-VII
Tuy	42.046	-8.624	V
Ubeda (Jaén)	38.017	-3.367	IV-V
Ulmeiro	39.667	-8.667	VII
Unhais da Serra	40.267	-7.617	IV-V
Unhos	38.817	-9.117	VI
Vagos	40.550	-8.683	IV
Vale da Pinta (Cartaxo)	39.172	-8.826	VIII
Vale de Paços (ou Valpaços)	41.600	-7.317	III
Vale de Santarém	39.191	-8.730	VII-VIII
Vale do Zêzere	38.594	-9.041	V
Valença (do Minho)	42.032	-8.637	V-VI
Vales (Zêzere)	39.817	-7.800	V
Valladolid	41.650	-4.717	III
Vau	39.367	-9.218	VI-VII
Vendas Novas (Sado)	38.677	-8.455	VI
Vialonga	38.874	-9.080	VI
Viana (do Alentejo)	38.333	-8.000	V
Viana do Castelo	41.700	-8.833	III
Vidigueira	38.217	-7.800	V
Viegas	39.416	-8.852	VI
Vieira	39.867	-8.933	VI
Vigo (Pontevedra)	42.233	-8.717	IV
Vila Alva	38.250	-7.900	V
Vila Boim	38.867	-7.283	IV
Vila da Ponte (Leomil)	40.917	-7.500	III
Vila do Bispo	37.083	-8.917	IV
Vila Flor (Bragança)	41.310	-7.150	II
Vila Franca de Xira	38.956	-8.990	VII-VIII
Vila Fresca (de Azeitão)	38.517	-9.000	IV-V
Vila Nogueira de Azeitão	38.519	-9.014	IV-V
Vila Nova da Rainha	39.037	-8.934	VII
Vila Nova de Baronia (Évora /Serpa)	38.283	-8.033	VI-VII
Vila Nova de Fozcoa	41.083	-7.200	IV
Vila Nova de Gaia	41.133	-8.617	IV

Vila Nova de Milfontes	37.717	-8.783	V
Vila Pouca de Aguiar	41.500	-7.650	IV
Vila Real	41.300	-7.750	V
Vila Real (de Santo António)	37.200	-7.417	V-VI
Vila Velha de Rodão	39.667	-7.700	V
Vila Verde (Lisboa)	39.150	-9.117	VI
Vila Viçosa	38.783	-7.417	V-VI
Vilar (Lisboa)	39.183	-9.117	V
Vilar Formoso	40.617	-6.833	III
Vilar Seco (Viseu)	40.550	-7.867	IV
Villagarcia (de la Torre)	38.290	-6.083	IV
Villagarcia de Arousa (Pontevedra)	42.600	-8.750	IV
Villamanrique	38.545	-3.005	IV-V
Vimioso	41.583	-6.533	II
Virtudes	39.088	-8.828	VIII
Viseu	40.650	-7.917	V
Zafra	38.426	-6.417	III-IV
Zamora	41.500	-5.750	IV
Zibreira (Castelo Branco)	39.850	-7.067	IV
Zibreira (Torres Novas)	39.484	-8.611	VI
Alicante	38.35	-0.483	NF
Almería	36.833	-2.45	NF
Logroño	42.467	-2.45	NF
Lugo	43	-7.567	NF
Orihuela	38.083	-0.95	NF
Roquetes	40.821	0.494	NF
Soria	41.767	-2.467	NF

CHAPTER *12*

Annex 5: Intensity data points of the events used to computed the attenuation law

This annex presents a detail of the intensity data points, for each earthquake used to computed the attenuation law.

Earthquake of the 4th of May 1909 at 19:15:00. Epicenter: 38.9˚, 8.8˚. M = 4.5.

Location	Latitude	Longitude	Intensity
Coruche	38.950	-8.517	VI
Carregado	39.017	-8.983	VI
Salvaterra	39.017	-8.800	VI
Benavente	38.983	-8.800	VI
Vila Franca de Xira	38.956	-8.990	VI
Azambuja	39.067	-8.867	V
Mora	38.944	-8.166	IV
Évora	38.567	-7.900	IV
Vendas Novas	38.677	-8.455	IV
Montemor-o-novo	38.650	-8.217	IV
Alcácer do Sal	38.371	-8.520	IV
Pero Moniz	39.217	-9.117	III
Santarém	39.236	-8.687	III
Almeirim	39.213	-8.627	III
Dois Portos	39.033	-9.167	III
Mafra	38.933	-9.317	III
Runa	39.050	-9.200	III
Lisboa	38.717	-9.133	III
Cascais	38.683	-9.417	III
Caparica	38.650	-9.183	III

Earthquake of 11th of June 1909 at 02:57:00. Epicenter: 38.9˚, -8.8. M = 5

Location	Latitude	Longitude	Intensity
Salvaterra	39.017	-8.783	VI
Valada	39.067	-8.75	VI
Samora	38.933	-8.867	VI
Azambuja	39.067	-8.867	V-VI
Pedrógão Grande	39.917	-8.133	V
Pedrógão Pequeno	39.9	-8.117	V
Cinco Vilas (Ansião)	39.9	-8.433	V
Alvaiázere	39.833	-8.383	V
Cabaços (Alvaiázere)	39.8	-8.333	V
Carril (Ferreira do Zêzere)	39.599	-8.352	V
Alqueidão de Sto Amaro	39.767	-8.3	V
Coruche	38.950	-8.517	V
Ferreira do Zêzere	39.683	-8.283	IV
Cardigos (Mação)	39.667	-7.983	IV

Earthquake of the 17th of August 1909 at 03:03:00. Epicenter: 38.9˚, -8.8˚. M = 5.19.

Location	Latitude	Longitude	Intensity
Alenquer	39.055	-9.011	V
Benavente	38.983	-8.800	V
Pero Moniz (Cadaval)	39.217	-9.117	IV-V
Azambuja	39.067	-8.867	IV-V
Samora	38.933	-8.867	IV-V
Vila Franca de Xira	38.956	-8.990	IV-V
Alhandra	38.924	-9.009	IV-V
Cartaxo	39.162	-8.786	IV
Amiais de Cima	39.433	-8.75	IV
Alcochete	38.756	-8.960	IV
Alcacer do Sal	38.371	-8.520	IV
Santarém	39.236	-8.687	III
Carmões	39.050	-9.133	III
Lisboa	38.717	-9.133	III
Almada	38.680	-9.159	III
Caparica	38.650	-9.183	III
Sétubal	38.525	-8.893	III

Earthquake of the 8th of December 1909 at 09:52:00. Epicenter: 38.9˚, -8.8˚. M = 5.19

Location	Latitude	Longitude	Intensity
Salvaterra	39.017	-8.783	VII
Benavente	38.983	-8.800	VI
S. Estevão	38.867	-8.750	VI
Azambuja	39.067	-8.867	V-VI

Earthquake of the 9th of February 1911 at 19:17:00. Epicenter: 41.7˚, -8.9˚. M = 5.0

Location	Latitude	Longitude	Intensity
Caminha	41.867	-8.833	VI
Viana do Castelo	41.700	-8.833	VI
Valença	42.032	-8.637	V
Vila Nova de Cerveira	41.933	-8.733	V
Âncora	41.8	-8.85	V
Ponte de Lima	41.75	-8.567	V
Esposende	41.533	-8.783	III

Earthquake of the 12th of August 1911 at 22:03:00. Epicenter: 36.5˚, -7.8˚. M = 5.2

Location	Latitude	Longitude	Intensity
Vila Real de Sto Antonio	37.200	-7.417	VI
Estói	37.100	-7.900	VI
Boliqueime	37.133	-8.15	VI
Albufeira	37.083	-8.233	VI
Aiamonte (Espanha)	37.35	-7.667	VI
Beja	38.017	-7.867	V
Sabóia	37.467	-8.533	V
S. Bartolomeu de Messines	37.25	-8.283	V
Loulé	38.133	-8.017	V
S. Braz de Alportel	37.15	-8.883	V
Olhão	37.033	-7.833	V
Faro	37.017	-7.933	V
Mértola	37.633	-7.667	IV
Cachopo	37.317	-7.817	IV
Benavente	38.983	-8.800	III
Montemor-o-novo	38.650	-8.217	III
Monchique	37.317	-8.55	III

Earthquake of the 23th of January 1912 at 14:00:00. Epicenter: 38.8˚, -7.8˚. M = 5.0

Location	Latitude	Longitude	Intensity
Vimieiro	38.917	-7.833	VI
Aviz	39.057	-7.891	V
Évora	38.567	-7.900	V
Arraiolos	38.717	-7.983	IV

Earthquake of the 11th of July 1912 at 07:18:00. Epicenter: 36.5˚, -7.8˚. M = 5.0

Location	Latitude	Longitude	Intensity
Vila Real de S. Antonio	37.200	-7.417	VI
Estói	37.100	-7.900	VI
Albufeira	37.083	-8.233	VI
Ferreira do Alentejo	38.050	-8.033	V
Serpa	37.933	-7.600	V
Sabóia	37.467	-8.533	V
Loulé	38.133	-8.017	V
S. Braz de Alportel	37.15	-8.883	V
Tavira	37.117	-7.650	V
Olhão	37.033	-7.833	V
Faro	37.017	-7.933	V
Boliqueime	37.133	-8.15	V
Alcantarilha	37.117	-8.333	V
Arraiolos	38.717	-7.983	IV
Portel	38.300	-7.700	IV
Sines	37.95	-8.85	IV
Monchique	37.317	-8.55	IV
Lagos	37.1	-8.667	IV

Earthquake of the 18th of October 1912 at 21:30:00. Epicenter: 41.5˚, -8.5˚. M= 5.0

Location	Latitude	Longitude	Intensity
Santa Lucrécia de Algeriz	41.594	-8.372	VI
Guimarães	41.450	-8.300	VI
Vila nova de Famalicão	41.4	-8.517	VI
Azões	41.683	-8.5	VI
Santo Tirso	41.342	-8.470	VI
Lousada	41.267	-8.283	VI
Paços de Ferreira	41.267	-8.400	VI
Freamunde	41.283	-8.35	VI
Bico (Paredes de Coura)	41.893	-8.526	V
Arcos de Valdevez	41.833	-8.417	V
Ponte de Lima	41.767	-8.583	V
Amares	41.633	-8.350	V
Fraião	41.535	-8.404	V
Barcelos	41.533	-8.617	V
Esposende	41.533	-8.783	V
Fão	41.517	-8.767	V
Póvoa de Lanhoso	41.583	-8.267	V
Vizela	41.367	-8.267	V
Margaride	41.35	-8.183	V
Póvoa de Varzim	41.367	-8.767	V
Penafiel	41.2	-8.283	V
Vila de Conde	41.333	-8.683	V
Valongo	41.183	-8.5	V
Caminha	41.867	-8.833	IV
Orbacem	41.8	-8.767	IV
Ãncora	41.8	-8.85	IV
Fafe	41.450	-8.167	IV
Amarante	41.267	-8.067	IV
Abragão	41.15	-8.217	IV
Santa Leocádia	41.553	-8.59	IV
Gerez	41.717	-8.15	III
Moncorvo	41.167	-7.050	III
Crestuma	41.05	-8.5	III
Cinfães	41.1	-8.133	III

Earthquake of the 27th of october 1913 at 04:30:00. Epicenter: 41.67˚, -8.72˚. M = 5.0

Location	Latitude	Longitude	Intensity
Barcelos	41.533	-8.617	V
Paredes	41.2	-8.317	V
Vila do Conde	41.333	-8.683	V
Caminha	41.867	-8.833	V
Agueda	40.567	-8.450	V
Famalicão	41.4	-8.517	V
Porto	41.150	-8.617	IV
Povoa de Varzim	41.367	-8.767	IV
Guimarães	41.450	-8.300	IV
Barcelos	41.533	-8.617	IV
Povoa de Lenhao	41.567	-8.267	III
Aveiro	40.633	-8.650	III
Coimbra	40.200	-8.417	III
Oliveira de Frades	40.733	-8.183	III
Ribeira de Pena	41.517	-7.783	III
Albergaria	40.683	-8.467	III
Valadares	41.1	-8.64	III
Vila nova de Cerveira	41.967	-8.683	III

Earthquake of the 23th of September 1914 at 03:19:00. Epicenter: 38.9˚, -8.8˚. M = 5.3

Location	Latitude	Longitude	Intensity
Benavente	38.983	-8.800	VI-VII
Azambuja	39.067	-8.867	VI
Salvaterra de Magos	39.017	-8.800	VI
Alcoentre	39.209	-8.960	V
Cartaxo	39.162	-8.786	V
Pontevel	39.149	-8.840	V
Aveiras de Cima	39.138	-8.900	V
Aveiras de Baixo	39.111	-8.869	V
Samora correia	38.933	-8.867	V
S. Estevão	38.867	-8.750	V
Santarém	39.236	-8.687	IV
Loures	38.830	-9.167	III

Earthquake of the 25th of September 1914 at 17:52:00. Epicenter: 38.9˚, -8.8˚. M = 5.3.

Location	Latitude	Longitude	Intensity
Benavente	38.983	-8.800	VI-VII
Vila Franca de Xira	38.956	-8.990	VI-VII
Tomar	39.604	-8.413	VI
Gavião	39.267	-8.300	VI
Chamusca	39.356	-8.480	VI
Pero Moniz (Cadaval)	39.217	-9.117	VI
Cartaxo	39.162	-8.786	VI
Pontével	39.149	-8.840	VI
Valada	39.067	-8.75	VI
Aveiras de Baixo	39.111	-8.869	VI
Marinhais	39.017	-8.683	VI
Salvaterra de Magos	39.017	-8.800	VI
Coruche	38.950	-8.517	VI
Samora Correira	38.933	-8.867	VI
S. Estevão	38.867	-8.750	VI
Azambuja	39.067	-8.867	VI
Alenquer	39.055	-9.011	VI
Torres Verdas	39.088	-9.260	VI
Arruda dos Vinhos	38.999	-9.068	VI
Alverca	38.891	-9.034	VI
Barreiro	38.658	-9.067	VI
Vimieiro	38.817	-7.833	VI
Ferreira do Zêzere	38.683	-8.292	V
Mação	39.55	-8	V
Entroncamento	39.467	-8.467	V
Caldas da Rainha	39.404	-9.136	V
Golegã	39.401	-8.487	V
Azinhaga	39.348	-8.530	V
Fráguas (Rio Maior)	39.367	-8.85	V
Santarém	39.236	-8.687	V
Alguber	39.26	-9.017	V
Cadaval	39.233	-9.100	V
Lourinhã	39.25	-9.317	V
Ramalhal	39.133	-9.217	V
Torres Verdas	39.088	-9.260	V
Alcoentre	39.209	-8.960	V
Merceana	39.083	-9.1	V
Atalaia	39.233	-9.317	V
Cadafais	39.005	-9.001	V
Runa	39.05	-9.2	V
Carmões	39.050	-9.133	V
Dois Portos	39.133	-9.167	V
Aviz	39.057	-7.891	V
Mora	38.944	-8.166	V
Sobral do Monte Agraço	39.018	-9.152	V
Alhandra	38.924	-9.009	V

Bucelas	38.902	-9.118	V
Caneças	38.817	-9.233	V
Alhos Vedros	38.65	-9.017	V
Coimbra	40.200	-8.417	IV
Alvaiázere	39.833	-8.383	IV
Leiria	39.750	-8.800	IV
Monte Real	39.817	-8.867	IV
Sertã	39.8	-8.1	IV
Vila de Rei	39.667	-8.133	IV
Nazaré	39.599	-9.064	IV
Valado de Frades	39.583	-9.017	IV
Alcobaça	39.550	-8.983	IV
Turquel	39.464	-8.974	IV
Niza	39.517	-7.650	IV
Mouriscas	39.5	-8.083	IV
Abrantes	39.467	-8.200	IV
Alferrarede	39.483	-8.167	IV
Torres Novas	39.480	-8.541	IV
Constância	39.467	-8.333	IV
Portalegre	39.283	-7.433	IV
Vale de Figueira	39.3	-8.617	IV
Alpiarça	39.260	-8.585	IV
Almeirim	39.213	-8.627	IV
Peniche	39.35	-9.367	IV
Bombarral	39.266	-9.153	IV
Elvas	38.883	-7.167	IV
Vila Fernando	40.483	-7.267	IV
Estremoz	38.900	-7.317	IV
Évora	38.567	-7.900	IV
Lavre	38.800	-8.517	IV
Ericeira	38.967	-9.417	IV
Fanhões	38.867	-9.15	IV
Loures	38.830	-9.167	IV
Sintra	38.783	-9.417	IV
Almoçageme	38.8	-9.467	IV
Queluz	38.755	-9.253	IV
Lisboa	38.717	-9.133	IV

Earthquake of the 11th of July 1915 at 11:28:36. Epicenter: 37˚, -10.5˚. M = 6.6

Location	Latitude	Longitude	Intensity
Veiros (Estarreja)	40.733	-8.6	VI
Torres Verdas	39.088	-9.260	VI
Negrelos (Santo Tirso)	41.35	-8.4	V
Lousada	41.267	-8.283	V
Matosinhos	41.183	-8.7	V
Gondomar	41.150	-8.533	V
Porto	41.150	-8.617	V
Arouca	40.933	-8.25	V
S. João da Madeira	40.9	-8.5	V
Aveiro	40.633	-8.650	V
S. Pedro de Muel	39.75	-9	V
Lourinhã	36.25	-9.317	V
Azambuja	39.067	-8.867	V
Alenquer	39.055	-9.011	V
Freiria (Torres Verdas)	39.017	-9.233	V
Sobral de Monte Agraço	39.018	-9.152	V
Coruche	38.950	-8.517	V
Benavente	38.983	-8.800	V
Vila Franca de Xira	38.956	-8.990	V
Alhandra	38.924	-9.009	V
Mafra	38.933	-9.317	V
Enxara dos Cavaleiros	38.983	-9.2	V
Sintra	38.783	-9.417	V
Lisboa	38.717	-9.133	V
Estoril	38.7	-9.383	V
Trafaria	38.670	-9.239	V
Montemor-o-novo	38.650	-8.217	V
Beja	38.017	-7.867	V
Sabóia	37.467	-8.533	V
Alverca	38.891	-9.034	V
Viana do Castelo	41.700	-8.833	IV
Pardelhas	41.333	-7.883	IV
Poiares	40.217	-8.267	IV
Santa Comba Dão	40.4	-8.133	IV
Coimbra	40.200	-8.417	IV
S. Vicente de Beira	40.033	-7.55	IV
Cabaço	41	-7.567	IV
Alqueidão	40.083	-8.767	IV
Leiria	39.750	-8.800	IV
Mação	39.55	-8	IV
Alcobaça	39.550	-8.983	IV
A. dos Francos	39.317	-9.05	IV
Peniche	39.357	-9.374	IV
Chamusca	39.356	-8.480	IV
Santarém	39.236	-8.687	IV
Almeirim	39.213	-8.627	IV
Ramalhal	39.133	-9.217	IV

Carmões	39.050	-9.133	IV
Dois Portos	39.033	-9.167	IV
Bucelas	38.902	-9.118	IV
Belas	38.767	-9.267	IV
Gradil	38.980	-9.279	IV
Linda-a-velha	38.717	-9.233	IV
Montijo	38.683	-8.9	IV
Almada	38.680	-9.159	IV
Lazareto	38.667	-9.217	IV
Elvas	38.883	-7.167	IV
Évora	38.567	-7.900	IV
Setúbal	38.525	-8.893	IV
Palma	39.067	-7.483	IV
Serpa	37.933	-7.600	IV
Sines	37.95	-8.85	IV
Silves	37.183	-8.433	IV
Faro	37.017	-7.933	IV
Lagos	37.100	-8.667	IV
Braga	41.550	-8.433	III
Viseu	40.650	-7.917	III
Portalegre	39.283	-7.433	III
Colares	38.8	-9.467	III

Earthquake of the 2nd of March 1924 at 06:45:00. Epicenter: 38.9˚, -8.8˚. M = 5.0

Location	**Latitude**	**Longitude**	**Intensity**
Azambuja	39.067	-8.867	V
Salvaterra	39.017	-8.800	V
Benavente	38.983	-8.800	V
Samora	38.933	-8.867	V
Coruche	38.950	-8.517	IV
Feliteira	39.017	-9.167	IV
Odivelas	38.793	-9.183	IV
Lisboa	38.717	-9.133	IV
Mora	38.944	-8.166	IV
Pedrógão grande	39.917	-8.133	III-IV
Leiria	39.750	-8.800	III-IV
Farminhão	40.6	-8	III
Batalha	39.65	-8.817	III
Aveiras da Cima	39.138	-8.900	III
Coimbra	40.200	-8.417	II-III
Santarém	39.236	-8.687	II-III
Marvão	39.400	-7.383	II

Earthquake of the 28th of February 1926 at 22:12:00. Epicenter: 38.5˚, -8.0˚. M = 5.5

Location	Latitude	Longitude	Intensity
Évora	38.567	-7.900	VII
Beja	38.017	-7.867	VI
Redondo	38.633	-7.533	VI
Reguengos de Monsaraz	38.417	-7.533	VI
Alandroal	38.700	-7.400	V
Alcanhões	39.296	-8.660	V
Alenquer	39.055	-9.011	V
Almeirim	39.213	-8.627	V
Alverca	38.891	-9.034	V
Arraiolos	38.717	-7.983	V
Aviz	39.057	-7.891	V
Azambuja	39.067	-8.867	V
Belver	39.483	-7.95	V
Cabeço de Vide	39.117	-7.583	V
Cardigos	39.683	-8.017	V
Cartaxo	39.162	-8.786	V
Castelo de Vide	39.417	-7.45	V
Elvas	38.883	-7.167	V
Estremoz	38.850	-7.583	V
Faro	37.017	-7.933	V
Ferreira do Zêzerre	38.683	-8.292	V
Monforte	39.05	-7.433	V
Motemor-o-novo	38.650	-8.217	V
Moura	38.133	-7.450	V
Pias	39.917	-8.333	V
Ponte de Sôr	39.248	-8.010	V
Portalegre	39.283	-7.433	V
Samora Correira	38.933	-8.867	V
Santarém	39.236	-8.687	V
Setubal	38.525	-8.893	V
Sintra	38.783	-9.417	V
Torrão	38.300	-8.217	V
Torres Novas	39.480	-8.541	V
Tremês	39.35	-8.75	V
Viana do Alentejo	38.333	-8.000	V
Vila Boim	38.867	-7.283	V
Vila Franca de Xira	38.956	-8.990	V
Vila Viçosa	38.783	-7.417	V
Lisboa	38.717	-9.133	IV-V
Agueda	40.567	-8.450	IV
Amoreira	37.667	-8.383	IV
Arganil	40.217	-8.050	IV
Arouca	40.933	-8.25	IV
Barquinha	39.450	-8.433	IV
Barreiro	38.658	-9.067	IV
Cascais	38.683	-9.417	IV

Castelo Branco	39.817	-7.500	IV
Coimbra	40.200	-8.417	IV
Covilhã	40.283	-7.500	IV
Fundão	40.133	-7.5	IV
Ilhavo	40.6	-8.667	IV
Loriga	40.317	-7.683	IV
Lousada	41.267	-8.283	IV
Obidos	39.362	-9.157	IV
Pombal	39.917	-8.633	IV
S. Comba Dão	40.4	-8.133	IV
Seia	40.417	-7.7	IV
Tabua	40.350	-8.033	IV
Tontela	40.517	-8.083	IV
Vila Real	37.200	-7.417	IV
Vilarinho	40.117	-8.2	IV
Viseu	40.650	-7.917	IV
Aguas de Moura	38.567	-8.683	III
Alcaçovas	38.4	-8.167	III
Alcochete	38.756	-8.960	III
Alenquer	39.055	-9.011	III
Alpalhão	39.417	-7.617	III
Alvalade	38.733	-8.167	III
Alvito	38.250	-7.983	III
Amieira	38.283	-7.55	III
Arronches	39.117	-7.283	III
Assumar	39.133	-7.383	III
Azinhaga	39.348	-8.530	III
Belver	39.483	-7.95	III
Benfeita	40.217	-7.933	III
Cabeção	38.952	-8.071	III
Castro Verde	37.7	-8.083	III
Crato	39.283	-7.65	III
Elvas	38.883	-7.167	III
Galveias	39.150	-8.000	III
Louriçal do Campo	40.033	-7.5	III
Mação	39.55	-8	III
Marinhais	39.05	-8.683	III
Merceana	39.067	-9.1	III
Messejana	37.833	-8.250	III
Montemor-o-novo	38.650	-8.217	III
Odemira	37.600	-8.633	III
Ourique	37.65	-8.217	III
Palmela	38.572	-8.903	III
Pavia	38.883	-8.017	III
Penacova	40.267	-8.267	III
Pinheiro Grande	39.391	-8.425	III
S. Cristóvão	38.483	-8.3	III
Samora Correira	38.933	-8.867	III
Santarém	39.236	-8.687	III
Seixal	38.643	-9.107	III
Sousel	38.950	-7.667	III
Tavira	37.117	-7.650	III
Veiros do Alentejo	38.95	-7.417	III
Vermelha	39.267	-9.1	III
Viana do Alentejo	38.333	-8.000	III

Vila Nova da Barouia	38.283	-8.033	III
Vila velha de Ródão	39.667	-7.700	III
Vimieiro	38.817	-7.833	III

Earthquake of the 10th of february 1930 at 08:04:00. Epicenter: 37.4˚, 8.1˚. M = 5.0.

Location	Latitude	Longitude	Intensity
Silves	37.183	-8.433	VI
Portimão	37.133	-8.533	VI
Loulé	38.133	-8.017	VI
Alcantarilha	37.133	-8.35	VI
Lagoa	37.133	-8.450	VI
Ferragudo	37.117	-8.517	VI
Monchique	37.317	-8.55	V
Boliqueime	37.133	-8.15	V
Quarteira	37.067	-8.1	V
Pera	37.117	-8.333	V
Estói	37.100	-7.900	V
Armação de Pera	37.1	-8.35	V
Albufeira	37.083	-8.233	V
Faro	37.017	-7.933	V
S. Luis (Odemira)	37.667	-8.683	IV
Sabóia	37.467	-8.533	IV
Aljezur	37.317	-8.800	IV
Messines	37.25	-8.283	IV
Vila Real de S. Antonio	37.200	-7.417	IV
S. Braz de Alportel	37.15	-8.883	IV
Mexilhoeira Grande	37.167	-8.617	IV
Tavira	37.117	-7.650	IV
Lagos	37.1	-8.667	IV
Cercal do Alentejo	37.8	-8.667	III-IV
Ourique	37.65	-8.217	III-IV
Odemira	37.600	-8.633	III-IV
Lisboa	38.717	-9.133	III
Évora	38.567	-7.900	III
Setúbal	38.525	-8.893	III
Beja	38.017	-7.867	III
Sines	37.95	-8.85	III
Alvalade	38.733	-8.167	III
Castro Verde	37.7	-8.083	III
Panóias (Alentejo)	37.75	-8.3	II
Casével (Alentejo)	37.75	-8.167	II
Alte	37.233	-8.167	II
Paderne	37.167	-8.2	II
Luz de Tavira	37.083	-7.717	II

Earthquake of the 25th of November 1941 at 18:04:00. Epicenter: 37.5˚, -18.5˚. M = 8.4.

Location	Latitude	Longitude	Intensity
Souto da Branca	41.767	-8.467	V-VI
Furadouro	40.867	-8.667	V-VI
Coimbra	40.200	-8.417	V-VI
Santarém	39.236	-8.687	V-VI
Chamusca	39.356	-8.480	V-VI
Lisboa	38.717	-9.133	V-VI
Aguda	41.033	-8.684	V
Leiria	39.750	-8.800	V
Peniche	39.357	-9.374	V
Bombarral	39.266	-9.153	V
Almeirim	39.213	-8.627	V
Alenquer	39.055	-9.011	V
Ribaldeira	39.033	-9.200	V
Benavente	38.983	-8.800	V
Gradil	38.980	-9.279	V
Alverca	38.891	-9.034	V
Póvoa de S. Iria	38.850	-9.067	V
Almargem do Bispo	38.833	-9.267	V
Loures	38.830	-9.167	V
Assafora	38.9	-9.4	V
Mercês	38.713	-9.143	V
Paiã	38.767	-9.2	V
Linda-a-velha	38.7	-9.233	V
Cascais	38.683	-9.417	V
Vila do Conde	41.333	-8.683	IV-V
Penafiel	41.2	-8.283	IV-V
Espinho	41	-8.633	IV-V
Tabua	40.350	-8.033	IV-V
Gois	40.083	-8.05	IV-V
Caldas da Rainha	39.404	-9.136	IV-V
Rego da Murta	39.817	-8.367	IV-V
Estoril	38.7	-9.383	IV-V
Sousel	38.950	-7.667	IV-V
Freamunde	41.283	-8.35	IV
Porto	41.150	-8.617	IV
Costa de Valado	40.583	-8.6	IV
Forte da Barra	40.633	-8.717	IV
Manteigas	40.400	-7.533	IV
Campo Maior	39.017	-7.067	IV
Elvas	38.883	-7.167	IV
Santiago do Cacém	38.017	-8.683	IV
Conceição de Tavira	37.133	-7.6	IV
Faro	37.017	-7.933	IV
Montalegre	41.817	-7.783	III-IV
Viana do Castelo	41.700	-8.833	III-IV

Soutelo	41.6	-8.433	III-IV
Póvoa de Lanhoso	41.583	-8.267	III-IV
Caldas da Saúde	41.367	-8.467	III-IV
Gondomar	41.150	-8.533	III-IV
Viseu	40.650	-7.917	III-IV
Penhas Douradas	40.4	-7.55	III-IV
Castelo Branco	39.817	-7.500	III-IV
Pedras Salgadas	41.533	-7.6	III
Vila Real	41.300	-7.750	III
Quinta do Anjo	38.667	-8.967	III
Bragança	41.75	-6.733	II-III
Moncorvo	41.167	-7.050	II-III
Guarda	40.533	-7.267	II-III
Paredes do Guardão	40.567	-8.167	II-III
Lagos da Beira	40.367	-7.817	II-III
Abrunhosa	40.567	-7.633	II

Earthquake of the 27th of December 1941 at 20:35:00. Epicenter: 38.5˚, -9.9˚. M = 5.1

Location	Latitude	Longitude	Intensity
Santiago do Cacém	38.014	-8.698	IV
Praia da Rocha	37.117	-8.533	IV
Faro	37.017	-7.933	IV
Lisboa	38.717	-9.133	III
Lagos	37.100	-8.667	III
S. Pedro de Muel	39.750	-9.000	II
Obidos	39.362	-9.157	II
Santarém	39.236	-8.687	II
Torres Verdas	39.088	-9.260	II
Sapataria	38.950	-9.200	II
Samouco	38.717	-8.983	II
Beja	38.017	-7.867	II
Évora	38.567	-7.900	II
Almodovar	37.512	-8.060	II
Castro Marim	37.217	-7.450	II
Portimão	37.133	-8.533	II

Earthquake of the 2nd of October 1947 at at 20:35:00. Epicenter: 38.5˚, -9.9˚. M = 5.1

Location	Latitude	Longitude	Intensity
Azenhas do Mar	38.833	-9.6	IV-V
Praia das Maças	38.817	-9.467	IV-V
Sintra	38.783	-9.417	IV-V
Lisboa	38.717	-9.133	IV-V
Oeiras	38.6974	-9.3084	IV-V
Cascais	38.683	-9.417	IV-V
Montijo	38.683	-8.9	IV-V
Barreiro	38.658	-9.067	IV-V
Almada	38.680	-9.159	IV-V
Caparica	38.650	-9.183	IV-V
Atouguia da Baleia	39.333	-9.317	IV
Bombarral	39.266	-9.153	IV
Cartaxo	39.162	-8.786	IV
Benavente	38.983	-8.800	IV
Villa Franca de Xira	38.956	-8.990	IV
Mafra	38.933	-9.317	IV
S. João das Lampas	38.867	-9.383	IV
Queluz	38.755	-9.253	IV
Caldas da Rainha	39.404	-9.136	III-IV
Peniche	39.35	-9.367	III-IV
Azambuja	39.067	-8.867	III-IV
Arruda dos Vinhos	38.999	-9.068	III-IV
Castanheira do Ribatejo	38.983	-8.967	III-IV
Sapataria	38.95	-9.2	III-IV
Negrais	38.867	-9.267	III-IV
Estremoz	38.900	-7.317	III-IV
Moscavide	38.767	-9.1	III-IV
Canha	38.769	-8.626	III-IV
Leiria	39.750	-8.800	III
Tomar	39.604	-8.413	III
Porto de Mos	39.6025	-8.8185	III
Constancia	39.467	-8.333	III
Vila Nova da Barquinha	39.45	-8.433	III
Chamusca	39.356	-8.480	III
Ponte de Sor	39.248	-8.010	III
Vimeiro	38.817	-7.833	III
Samora Correira	38.933	-8.867	III
Malveira	38.9292	-9.26	III
Póvoa da Santa Iria	38.850	-9.067	III
Alandroal	38.700	-7.400	III
Figueira da Foz	40.1508	-8.8512	II-III
Braga	41.550	-8.433	II
Vila Real	37.200	-7.417	II
Porto de Mos	39.6025	-8.8185	II
Viseu	40.650	-7.917	II
Guarda	40.533	-7.267	II
Coimbra	40.200	-8.417	II

Earthquake of the 12th of August 1948 at 23:04:00. Epicenter: 40.1˚, -8.6˚. M = 5.2

Location	Latitude	Longitude	Intensity
Condeixa	40.117	-8.500	V-VI
Luso	40.383	-8.383	IV-V
Mealhada	40.533	-6.917	IV-V
Coimbra	40.200	-8.417	IV-V
Cantanhede	40.346	-8.594	IV
Montemor-o-velho	40.167	-8.683	IV
Alpedrinha	40.083	-7.450	IV
Alvares	40.033	-8.083	IV
Porto	41.150	-8.617	III-IV
Lamego	41.083	-7.867	III-IV
Pinhel	40.776	-7.063	III-IV
S. Pedro do Sul	40.750	-8.067	III-IV
Curia	40.417	-8.450	III-IV
Manteigas	40.400	-7.533	III-IV
Figueiro dos Vinhos	39.907	-8.289	III-IV
Fiães	41.900	-8.650	III
Vieira do Minho	41.634	-8.142	III
Antas	40.650	-7.550	III
Braga	41.550	-8.433	III
Barcelos	41.533	-8.617	III
Mondim de Basto	41.417	-7.950	III
Vila do Conde	41.333	-8.683	III
Ermesinde	41.217	-8.533	III
S. Mamede de Infesta	41.183	-8.617	III
Aveiro	40.633	-8.650	III
Caramulo	40.567	-8.167	III
Mortagua	40.400	-8.233	III
Loriga	40.317	-7.683	III
Covilhã	40.283	-7.500	III
Arganil	40.217	-8.050	III
Figueira da Foz	40.151	-8.851	III
Alfarelos	40.151	-8.653	III
Pombal	39.917	-8.633	III
Rego da Murta	39.817	-8.367	II

Earthquake of the 5th of December 1960 at 21:23:00. Epicenter: 35.6˚, -7.2˚. M = 5.0

Location	Latitude	Longitude	Intensity
Olhão	37.033	-7.833	IV
Tavira	37.117	-7.650	III-IV
Albufeira	37.083	-8.233	III
Lagos	37.1	-8.667	III
Loulé	38.133	-8.017	III
Silves	37.183	-8.433	III
Évora	38.567	-7.900	II-III

Earthquake of the 10th of February 1961 at 18:52:00. Epicenter: 41.51˚, -6.02˚. M = 5.2

Location	Latitude	Longitude	Intensity
Silva	41.5	-6.65	V-VI
Palaçoulo	41.45	-6.433	V-VI
Ifanes	41.567	-6.25	IV-V
Miranda do Douro	41.5	-6.267	IV-V
Bragança	41.8	-6.75	III-IV
Parada	41.667	-6.683	III-IV
Paradela	41.567	-6.2	III-IV
Melhadas	41.533	-6.317	III-IV
Duas Igrejas	41.467	-6.35	III-IV
Bemposta	41.3	-6.5	III-IV
Sendim	41.383	-6.417	III
Tó	41.317	-6.55	III
Picote	41.4	-6.367	II-III
Carviçais	41.167	-6.883	I-II

Earthquake of the 15th of March 1964 at 22:31:10. Epicenter: 36.09˚, -7.86˚. M = 6.2

Location	Latitude	Longitude	Intensity
Alcoutim	37.467	-7.467	VII
Tavira	37.117	-7.650	VII
Montemor-o-novo	38.650	-8.217	V-VI
Alcacer do Sal	38.371	-8.520	V-VI
S. Domingo	37.667	-7.483	V-VI
Quarteira	37.067	-8.1	V-VI
Tomar	39.604	-8.413	V
Castelo de vide	39.417	-7.45	V
Chamusca	39.356	-8.480	V
Portalegre	39.283	-7.433	V
Lavre	38.800	-8.517	V
Beja	38.017	-7.867	V
Serpa	37.933	-7.600	V
Mertola	37.633	-7.667	V
Vila do Bispo	37.0831	-8.9088	V
Albufeira	37.083	-8.233	V
Guarda	40.533	-7.267	IV-V
Sabugal	40.35	-7.083	IV-V
Belmonte	40.367	-7.35	IV-V
Penamacor	40.167	-7.167	IV-V
Fundão	40.133	-7.5	IV-V
Monte redondo	39.9	-8.817	IV-V
Leiria	39.750	-8.800	IV-V
Porto de Mós	39.6025	-8.8185	IV-V
Torres Novas	39.480	-8.541	IV-V
Alcobertas	39.417	-8.9	IV-V
Coruche	38.950	-8.517	IV-V
Redondo	38.633	-7.533	IV-V
Setubal	38.525	-8.893	IV-V
Portel	38.300	-7.700	IV-V
Vale Formoso	40.367	-7.367	IV-V
Sagres	37	-8.933	IV-V
Vila Pouca de Aguiar	41.5	-7.633	IV
Senhora da Hora	41.183	-8.65	IV
Castro daire	40.9	-7.933	IV
Penalva do Castelo	40.667	-7.683	IV
Penhas douradas	40.4	-7.55	IV
Cantanhede	40.346	-8.594	IV
Góis	40.083	-8.05	IV
Lousã	40.117	-8.25	IV
Pedrogão Grande	39.917	-8.133	IV
Oleiros	39.917	-7.917	IV
Pombal	39.917	-8.633	IV
Castelo Branco	39.817	-7.500	IV
Vila de Rei	39.667	-8.133	IV
Bemposta	41.3	-6.5	IV
Ponte de Sôr	39.248	-8.010	IV

Alenquer	39.055	-9.011	IV
Vila Franca de Xira	38.956	-8.990	IV
Mafra	38.933	-9.317	IV
Elvas	38.883	-7.167	IV
Sintra	38.783	-9.417	IV
Cacém	38.767	-9.3	IV
Arraiolos	38.717	-7.983	IV
Montijo	38.683	-8.9	IV
Odemira	37.600	-8.633	IV
S. Maria de Emeres	41.533	-7.367	III-IV
Pedras Salgadas	41.533	-7.6	III-IV
Amarante	41.267	-8.067	III-IV
Paços de Ferreira	41.283	-8.383	III-IV
Caramulo	40.567	-8.167	III-IV
Gouveia	40.5	-7.6	III-IV
Tondela	40.517	-8.083	III-IV
Oliveira do Bairro	40.517	-8.5	III-IV
Tocha	40.3	-8.75	III-IV
Soure	40.05	-8.617	III-IV
Gavião	39.267	-8.300	III-IV
Marvão	39.400	-7.383	III-IV
Gafete	39.4	-7.667	III-IV
Cabo carvoeiro	39.35	-9.4	III-IV
Cadaval	39.25	-9.1	III-IV
Lourinhã	36.25	-9.317	III-IV
Évora	38.567	-7.900	III-IV
Viana do Castelo	41.700	-8.833	III
Vieira do Minho	41.634	-8.142	III
Macedo de Cavaleiros	41.533	-6.95	III
Vila de Conde	41.333	-8.683	III
Arouca	40.933	-8.25	III
Braga	41.550	-8.433	II-III
Espinho	41	-8.633	II
Poiares	40.217	-8.267	II

Earthquake of the 28th of February 1969 at 02:41:20. Epicenter: 35.94˚, -10.85˚. M = 8.0

Location	Latitude	Longitude	Intensity
Paderne	37.167	-8.200	VIII
Bensafrim	37.150	-8.733	VIII
Vila do Bispo	37.083	-8.909	VIII
Sagres	37.000	-8.933	VIII
Ameixial	37.350	-7.950	VII-VIII
Aljezur	37.315	-8.805	VII-VIII
Castro Marim	37.217	-7.450	VII-VIII
Lagoa	37.133	-8.450	VII-VIII
Portimão	37.133	-8.533	VII-VIII
Armação de Pêra	37.100	-8.350	VII-VIII
Lagos	37.100	-8.667	VII-VIII
Quarteira	37.067	-8.100	VII-VIII
Estarreja	40.750	-8.567	VII
Alfeizerão	39.501	-9.103	VII
Tornada	39.448	-9.129	VII
Foz de Arelho	39.431	-9.226	VII
Marvão	39.400	-7.383	VII
Peniche	39.357	-9.382	VII
Chamusca	39.356	-8.480	VII
Rio Maior	39.337	-8.936	VII
S. Pedro da Cadeira	39.067	-9.367	VII
Salvaterra de Magos	39.017	-8.783	VII
Mora	38.944	-8.166	VII
Cabrela	38.583	-8.450	VII
S. Manços	38.459	-7.753	VII
Alcaçovas	38.400	-8.167	VII
Vidigueira	38.210	-7.800	VII
Grandola	38.176	-8.568	VII
Beja	38.016	-7.865	VII
Abela	37.998	-8.557	VII
Cercal do Alentejo	37.800	-8.667	VII
Reliquias	37.700	-8.483	VII
Odemira	37.600	-8.633	VII
Almodovar	37.512	-8.060	VII
S. Teotonio	37.512	-8.708	VII
S. Marcos da Serra	37.350	-8.367	VII
Foia	37.300	-8.583	VII
Monchique	37.317	-8.550	VII
Vila Real de S. Antonio	37.200	-7.417	VII
Silves	37.183	-8.433	VII
Loulé	38.133	-8.017	VII
Albufeira	37.083	-8.233	VII
Faro	37.017	-7.933	VII
Alcobaça	39.550	-8.983	VI-VII
Alcanena	39.467	-8.667	VI-VII
Caldas da Rainha	39.404	-9.136	VI-VII
Bombarral	39.266	-9.153	VI-VII
Lourinhã	39.250	-9.317	VI-VII
Santarém	39.236	-8.687	VI-VII

Cartaxo	39.162	-8.786	VI-VII
Ericeira	38.967	-9.417	VI-VII
Aguas de Moura	38.567	-8.683	VI-VII
Mourão	38.383	-7.333	VI-VII
Alcacer do Sal	38.371	-8.520	VI-VII
Portel	38.300	-7.700	VI-VII
Cuba	38.137	-7.883	VI-VII
Melides	38.147	-8.729	VI-VII
Santiago do Cacem	38.014	-8.698	VI-VII
Pias	39.917	-8.333	VI-VII
Sines	37.950	-8.850	VI-VII
Vila Verde de Ficalho	37.933	-7.283	VI-VII
Aljustrel	37.874	-8.166	VI-VII
Vila Nova de Milfontes	37.728	-8.785	VI-VII
S. Luis	37.667	-8.667	VI-VII
Alcoutim	37.467	-7.467	VI-VII
Odeceixe	37.417	-8.767	VI-VII
Ourique	37.650	-8.217	VI-VII
Odeleite	37.333	-7.483	VI-VII
Tunes	37.167	-8.250	VI-VII
Tavira	37.117	-7.650	VI-VII
Fuzeta	37.050	-7.750	VI-VII
Caminha	41.867	-8.833	VI
Terras de Bouro	41.717	-8.317	VI
Viana do Castelo	41.700	-8.833	VI
Esposende	41.533	-8.783	VI
Póvoa do Verzim	41.417	-8.767	VI
Penafiel	41.200	-8.283	VI
Feira	40.917	-8.550	VI
Arouca	40.933	-8.250	VI
Ovar	40.867	-8.633	VI
Vale de Cambra	40.844	-8.399	VI
Albergaria a velha	40.694	-8.481	VI
Mira	40.428	-8.735	VI
Oliveira do hospital	40.360	-7.862	VI
Mealhada	40.533	-6.917	VI
Coimbra	40.200	-8.417	VI
Montemor-o-velho	38.645	-8.215	VI
Alfarelos	40.150	-8.650	VI
Lavos	40.091	-8.838	VI
Louriçal	40.033	-7.500	VI
Pombal	39.917	-8.633	VI
Monte Redondo	39.900	-8.817	VI
Leiria	39.750	-8.800	VI
Ponte de Mos	39.603	-8.819	VI
Abrantes	39.467	-8.200	VI
Alpiarça	39.267	-8.583	VI
Azoia de Cima	39.333	-8.733	VI
Ponte de Sôr	39.248	-8.010	VI
Vimeiro	38.817	-7.833	VI
Montargil	39.079	-8.171	VI

Aviz	39.057	-7.891	VI
Benavente	38.983	-8.800	VI
Coruche	38.950	-8.517	VI
V. Franca de Xira	38.956	-8.990	VI
Estremoz	38.900	-7.317	VI
Vendas Novas	38.677	-8.455	VI
Arraiolos	38.717	-7.983	VI
Lisboa	38.707	-9.136	VI
Carcavelos	38.688	-9.334	VI
Casa Branca	38.947	-7.807	VI
Azeitão	38.517	-9.000	VI
Palmela	38.572	-8.903	VI
Évora	38.567	-7.900	VI
Sesimbra	38.445	-9.102	VI
Reguengos	38.417	-7.533	VI
Ferreira do Alentejo	38.050	-8.033	VI
Alvalade	38.733	-8.167	VI
Messejana	37.833	-8.250	VI
S. Braz de Alportel	37.150	-8.883	VI
Olhão	37.033	-7.833	VI
Monção	42.067	-8.467	V-VI
Arcos de Valdevez	41.833	-8.417	V-VI
Braga	41.550	-8.433	V-VI
Barcelos	41.533	-8.617	V-VI
Amarante	41.267	-8.067	V-VI
Oleiros	39.917	-7.917	V-VI
Castelo de Paiva	41.042	-8.263	V-VI
Aveiro	40.633	-8.650	V-VI
Celorico da Beira	40.628	-7.399	V-VI
Covilhã	40.283	-7.500	V-VI
Figueira da Foz	40.151	-8.851	V-VI
Penamacor	40.167	-7.167	V-VI
Pedrogão pequeno	39.900	-8.117	V-VI
Ferreira do Zêzere	38.683	-8.292	V-VI
Bouça	41.633	-7.200	V-VI
Mação	39.550	-8.000	V-VI
Nisa	39.520	-7.654	V-VI
Atalaia	39.233	-9.317	V-VI
Alpalhão	39.417	-7.617	V-VI
Portalegre	39.283	-7.433	V-VI
Crato	39.283	-7.650	V-VI
Azambuja	39.067	-8.867	V-VI
Fronteira	39.056	-7.650	V-VI
Campo Maior	39.017	-7.067	V-VI
Elvas	38.883	-7.167	V-VI
Parede	38.687	-9.356	V-VI
Aldeia Nova	39.100	-9.233	V-VI
Castro verde	37.700	-8.083	V-VI
Minas de S. Domingo	37.667	-7.483	V-VI
Mertola	37.633	-7.667	V-VI
Montalegre	41.817	-7.783	V
Ferral	41.683	-7.983	V
Chaves	41.750	-7.533	V
Boticas	41.683	-7.667	V
Amares	41.617	-8.350	V
Vieira do Minho	41.634	-8.142	V
Vila Pouca de Aguiar	41.500	-7.633	V

Campanhã	41.150	-8.567	V
Carrazeda de Ansiães	41.250	-7.300	V
S. Maria de Sardoura	41.050	-8.283	V
Moimenta	40.950	-8.633	V
Figueira do Castelo Rodrigo	40.900	-6.967	V
S. Pedro do Sul	40.750	-8.067	V
Almeida	40.726	-6.907	V
Viseu	38.831	-7.840	V
Caramulo	40.567	-8.167	V
Guarda	40.655	-7.179	V
S. Comba Dão	40.400	-8.133	V
Belmonte	40.367	-7.350	V
Sabugal	40.350	-7.083	V
Buarcos	40.165	-8.878	V
Fundão	40.133	-7.500	V
Pampilhosa da Serra	40.050	-7.950	V
Pedrogão	39.917	-8.133	V
Castelo Branco	39.817	-7.500	V
Proença a nova	39.750	-7.917	V
Fatima	39.633	-8.667	V
Tomar	39.604	-8.413	V
Vinhais	41.817	-7.000	IV-V
Montalegre	41.817	-7.783	IV-V
Bragança	41.800	-6.750	IV-V
Monfortinho	40.003	-6.915	IV-V
Barrancos	38.129	-6.976	IV-V
Vimioso	41.567	-6.517	IV-V
Miranda do Douro	41.500	-6.267	IV-V
Picote	41.400	-6.367	IV-V
Bemposta	41.300	-6.500	IV-V
Meda	40.963	-7.263	IV-V
Penhas douradas	40.400	-7.550	IV-V

Earthquake of the 24 of December 1969 at 05:06:00. Epicenter: 36.0˚, -10.0˚. M = 5.0

Location	Latitude	Longitude	Intensity
Cercal do Alentejo	37.8	-8.667	IV
Sines	37.95	-8.85	III-IV
V. Nova de Milfontes	37.7277	-8.7853	III-IV
Odeceixe	37.417	-8.767	III-IV
Sagres	37	-8.933	III-IV
Aljezur	37.3147	-8.8045	III
Alvalade (Santiago de Cacer)	38.733	-8.167	I-II

Earthquake of the 14th of June 1972 at 21:58:15. Epicenter: 36.7˚, -8.4˚. M = 5.2

Location	Latitude	Longitude	Intensity
Albufeira	37.083	-8.233	IV-V
Praia da Rocha	37.117	-8.533	IV
Rogil	37.367	-8.8	III-IV
Monchique	37.317	-8.55	III-IV
S. Bartolomeu deMessines	37.25	-8.283	III-IV
Bensafrim	37.15	-8.733	III-IV
Boliqueime	37.133	-8.15	III-IV
Alcanharilha	37.117	-8.333	III-IV
S. Luis	37.667	-8.683	II-III
Odeceixe	37.417	-8.767	II-III
Bordeira	37.183	-8.85	II-III
Paderne	37.167	-8.2	II-III
Tavira	37.117	-7.650	II-III
Sagres	37	-8.933	II-III
Cercal	37.8023	-8.6731	II-III
Vila do Bispo	37.0831	-8.9088	II
Fuzeta	37.05	-7.75	II
Linda a velha	38.717	-9.233	I-II
Melides	38.1472	-8.7293	I-II
Odemira	37.600	-8.633	I-II

Earthquake of the 4th of april 1982 at 23:03:38. Epicenter: 39.0˚, -10.3˚. M = 5.2

Location	Latitude	Longitude	Intensity
Nazaré	39.599	-9.064	III-IV
Peniche	39.35	-9.367	III
S. Martinho do Porto	39.5122	-9.1348	II-III
Ericeira	38.967	-9.417	II
Dois Portos	39.033	-9.167	II
Lourinhâ	39.25	-9.317	II
Sintra	38.783	-9.417	II
Mem Martins	38.7941	-9.3451	II
Venda Nova (Amadora)	38.75	-9.2	II
Amadora	38.733	-9.233	II
Parede	38.6874	-9.356	II
Lisboa	38.717	-9.133	II
Queluz	38.755	-9.253	II
Sobral	39.0184	-9.1519	II
Torres verdas	39.088	-9.260	II
Obidos	39.362	-9.157	II

Earthquake of the 10th of August 1986 at 15:11:54. Epicenter: 41.03˚, -7.16˚. M = 4.3

Location	Latitude	Longitude	Intensity
Horta	41.067	-7.3	V
Sebadelhe	41.05	-7.267	V
Touça	41.033	-7.233	V
Murça do Douro	41.4	-7.45	V
Freixo de Numão	41.067	-7.217	V
Numão	41.083	-7.283	V
Villa nova de Foz Coa	41.0829	-7.1351	V
Pocinho	41.117	-7.117	V
Carrazeda de Ansiães	41.25	-7.3	IV
Tua	41.2	-7.417	IV
São Mamede de Ribatua	41.25	-7.417	IV
Felgar	41.2	-6.95	IV
Maçores	41.117	-7	IV
Paramos	40.967	-8.633	IV
S. João da Pesqueira	41.15	-7.4	IV
Ervedosa do Douro	41.167	-7.483	IV
Sousa	41.35	-8.233	IV
Moncorvo	41.2	-7.133	IV
Almendra	41	-7.05	III
longroiva	40.95	-7.2	III
Meda	40.967	-7.267	III
Pinhão	41.183	-7.533	III
Folgosa	41.15	-7.667	III
Peso de Regua	41.167	-7.783	III
Celorico da Beira	40.633	-7.383	III
Carva;ho de Ega	41.267	-7.183	III
Marialva	40.9	-7.233	III
Vila flor	41.3	-7.15	III
Sanfins do Douro	41.283	-7.517	II-III
Mirandela	41.483	-7.183	II
Pinhel	40.776	-7.063	II
Gouveia	40.5	-7.6	II
Rio Torto	40.5	-7.65	II
Viseu	40.650	-7.917	II
Grijó	41.483	-6.967	II
Trancoso	40.783	-7.35	II
Torrozelo	40.383	-7.75	II
Chamusca da Beira	39.356	-8.480	II
Rio Tinto	41.183	-8.567	II
Gondomar	41.150	-8.533	II
Matosinhos	41.183	-8.7	II

Marco de Canaveses	41.183	-8.15	III-IV
Moncorvo	41.2	-7.133	III-IV
Penalva do Castelo	40.667	-7.683	III-IV
Mangualde	40.6057	-7.766	III-IV
Nelas	40.53	-7.8553	III-IV
Tondela	40.5164	-8.0808	III-IV
Miranda do Douro	41.5	-6.267	III
Paredes	41.2	-8.317	III
Porto	41.150	-8.617	III
Vila Nova de Foz Côa	41.0829	-7.1351	III
Castelo de Paiva	41.0417	-8.2631	III
Arouca	40.933	-8.25	III
Pinhel	40.776	-7.063	III
Aveiro	40.633	-8.650	III
Agueda	40.567	-8.45	III
Felgueiras	41.367	-8.183	III
Guarda	40.6549	-7.179	III
Seia	40.4204	-7.7032	III
Belmonte	40.367	-7.35	III
Coimbra	40.2115	-8.4292	III
Torres Novas	39.480	-8.541	III
Castelo de vide	39.4147	-7.4566	III
Lisboa	38.7069	-9.1356	II

Earthquake of the 21th of May 1997 at 23:50:47. Epicenter: 42.43˚, -7.17˚. M = 5.4

Location	Latitude	Longitude	Intensity
França	41.9	-6.733	V
Pitões	41.833	-7.95	V
Montalegre	41.817	-7.783	V
Vinhais	41.817	-7	V
Gralhos	41.783	-7.733	V
Paradela	41.567	-6.2	V
Gerês	41.717	-8.15	V
Sudro	41.667	-8.1	V
Cabril	41.717	-8.017	V
Terras do Bouro	41.717	-8.317	V
Chaves	41.75	-7.533	V
Fafiães	41.133	-8.2	V
Carvalhelhos	41.683	-7.717	V
Boticas	41.683	-7.667	V
Castanheira	38.990	-8.972	V
Faiões	41.75	-7.417	V
Vidago	41.633	-7.567	V
Piso˜es	41.733	-7.867	V
Velpaços	41.6	-7.317	V
Rio Tarto	41.55	-7.267	V
Eixos	40.633	-8.567	V
Pedras Salgadas	41.533	-7.6	V
Póvoa de Lanhoso	41.583	-8.267	V
Vila Real	41.300	-7.750	V
Melgaço	42.117	-8.267	IV-V
Bragança	41.8	-6.75	IV-V
Amares	41.633	-8.350	IV-V
Braga	41.550	-8.433	IV-V
Macedo de Cavaleiros	41.533	-6.95	IV-V
Carvalhais	41.5	-7.167	IV-V
Mirandela	41.483	-7.183	IV-V
Guimarães	41.450	-8.300	IV-V
Monção	42.067	-8.467	IV
Valença	42.032	-8.637	IV
Arcos de Valdevez	41.833	-8.417	IV
Rabal	41.867	-6.75	IV
Ponte de Lima	41.75	-8.567	IV
Barcelos	41.533	-8.617	IV
Amarante	41.267	-8.067	IV
Vila Meã	41.967	-8.667	IV
S. Marinha	41.7	-8.35	IV
Penafiel	41.2	-8.283	IV
Regua	41.15	-7.783	IV
Meda	40.963	-7.2631	IV
Vizela	41.367	-8.267	IV
Castro Daire	40.9	-7.933	IV
Viseu	40.650	-7.917	IV
Caminha	41.867	-8.833	III-IV
Viana do Castelo	41.700	-8.833	III-IV

Bibliography

Agostinelli C. and Rotondi, R. (2001). Using Bayesian belief networks to analyse the stochastic dependence between interevent time and size of earthquakes. *J. Seismol.*, **7**: 281-299.

Aki, K. (1966). Generation and Propagation of G waves from the Nigata earthquake of June 14, 1964. Part 2. Estimation of earthquake moment, released energy and stress-strain drop from G wave spectrum. *Bulletin of the Earthquake Research Institute* **44**: 73–88.

Algermissen, S.T., and Perkins, D.M. (1976). A probabilistic estimate of maximum acceleration in rock in the contiguous United States, *U.S. Geological Survey Open-File Report*.

Ambraseys, N., K. Simpson, and J. Bommer (1996). Prediction of horizontal response spectra in Europe, *Earthquake Eng. Struct. Dyn*. **25,** 371– 400.

Ammon, C. J., Lay, T., Kanamori, H. and Cleveland M. (2011). A rupture model of the 2011 off the Pacific coast of Tohoku Earthquake, *Earth Planets Space*, **63**, 693-696. doi:10.5047/eps.2011.05.015.

Aochi, H. and Ide, S. (2011). Conceptual multi-scale dynamic rupture model for the 2011 Off-the-Pacific-Coast-of-Tohoku earthquake, E*arth Planets Space*, **63**, 761-765. doi 2011:10.5047/eps.2011.05.008.

Argus, D., Gordon, R., Demets, C., Stein, S., (1989), Closure of the Africa-Eurasia- North America Plate Motion Circuit and Tectonics of the Gloria Fault, *J. Geophys. Res.*, vol.**94**, n. B5, pp.5585-5602.

Atkinson, G., and Boore D. (1997). Some comparisons between recent ground motion relations, *Seismological Research Letters* **68,** 24–40.

Atkinson, G., and Sonley E. (2000). Empirical relationships between Modified Mercalli intensity and response spectra, *Bull. Seism. Soc. Am.* **90,** 537–544.

Atkinson G. (2013). Empirical evaluation of aleatory and epistemic uncertainty in eastern ground motions. *Seismological Research Letters* **84**: 130-138.

Bakun, W. H., and Wentworth, C. M. (1997). Estimating Earthquake Location and Magnitude from Seismic Intensity Data, *Bull. Seism. Soc. Am.* **87**, 1502-1521.

Beauval, C. (2003). Analyse des incertitudes dans une estimation probabiliste de l'aléa sismique, exemple de la France. *PhD thesis University of Joseph Fourier* – Grenoble I, France.

Beauval, C., and Scotti, O. (2003a). Mapping b-values in France using two different magnitude ranges: possible non power-law behavior. *Geophys. Res. Lett.,* **30**(17), 1892, doi: 10.1029/2003GL017576.

Beauval, C., and Scotti, O. (2003b). Variabilité dans la modélisation de la récurrence des séismes et impact sur l'évaluation de l'aléa sismique en France, *6ème colloque national AFPS*, 1-3 juillet, Ecole Polytechnique, Palaiseau.

Bender, B. (1986). Modelling source zone boundary uncertainty in seismic hazard analysis. *Bull. Seism. Soc. Am.* **76** 329-341.

Bensaude A. (1910). Le Tremblement de Terre de la Vallée du Tage du 23 Avril 1909 (Note préliminaire). *Bull Soc Port Sci Nat* IV:89–129.

Bernreuteur, D.L., Savy, J.B., Mensing, R.W., and Chen, J.C. (1989). Seismic hazard characteristization of 69 nuclear power plant sites East of the Rocky Mountains, *U.S. Nuclear Regulatory Commission*. NUREG/CR-5250.

Bezzeghoud M., Borges J.F. and Caldeira, B. (2012). Fontes sísmicas ao longo da fronteira de placas tectónicas entre os Açores e a Argélia: um modelo sismotectónico. In: R. Dias, A. Araújo, P. Terrinha, J.C. Kullberg (Eds), Geologia de Portugal, Escolar Editora, **vol. 2**, 747-790, ISBN: 978-972-592-364-1, p. 747-790.

Bezzeghoud M., (2011). Fontes sísmicas da zona ocidental do limite entre as placas EurásiaNúbia. Contribuição Sismotectónica e Geodinâmica. Lição de agregação *(lesson on Seismic sources of the western boundary between the EurasiaNubia plates. Seismotectonics and Geodynamics Contribution)*, February 2011, University of Évora, **11** p. 13 / 40.

Bezzeghoud M., J.F. Borges and B. Caldeira, (2011). Ground Motion Simulations of the SW Iberia Margin: Rupture Directivity and Earth Structure Effects. Natural Hazard, **69**, 2, 1229-1245, DOI 10.1007/s11069-011-9925-2

Bezzeghoud M. and Borges, J.F (2003). Mecanismos focais dos sismos em Portugal continental e margem adjacente. Física de la Tierra, Sismicidade de la Península Ibérica, Eds: E. Buforn y A. Udias, **15**, 229-245.

Bezzeghoud, M., Fitas, A., Borges, J. F., Carrilho, F. and Senos, M. L., (2000). Seismicity, focal mechanisms and source parameters in south Portugal. *2a assembleia Luso-Espanhola de Geodesia e Geofísica*, Lagos, Portugal, 129-130.

Biasi, G. P. and Weldon, R. (2008). San Andreas fault rupture scenarios from multiple paleoseismic records: Stringing pearls: in Working Group on California Earthquake Probabilities, Version 2 (UCERF2) U.S.G.S., *Appendix E: Open-File Report 2007-1437 and California Geological Survey Special Report 203.*

Bishop, C. (2006). Pattern recognition and machine learning. Springer.

Borges, J.F., (2003). Fonte Sísmica em Portugal- Algumas Implicações na Geodinâmica da Região Açores-Gibraltar, *PhD thesis*, Univ.Évora.

Borges, J. F., Fitas, A. J. S., Bezzeghoud, M. and Teves-Costa, P., (2001). Seismotectonics of Portugal and its adjacent Atlantic area. *Tectonophysics*, **337**, 373-387.

Borges, J. F., (1991). Métodos automáticos na determinação de mecanismos focais. *Relatório de Licenciatura, Faculdade de Ciências da Universidade de Lisboa*. pp. 93.

Borges, J. F., (1996). Mecanismos focais de sismos de Portugal continental e região Atlântica adjacente, *Dissertação de mestrado apresentada à Universidade de Lisboa para a obtenção do grau de mestre em Ciências Geofísicas, especialidade Geofísica Interna.*

Buforn, E., Udias, A., and Colombas, A., (1988a). Seismicity, source mechanisms and tectonics of the Azores-Gibraltar Plate boundary. *Tectonophysics* **152**, 89-118.

Buforn, E., Mézcua, J., and Udias, A., (1988b). Mecanismo focal del terramoto del Cabo San Vicente de 20 de Octubre de 1986. *Rev. Geofís* 44, 109-112.

Buforn, E., C. Sanz de Galdeano, and A. Udias (1995). Seismotectonics of the Ibero-Maghrebian region, *Tectonophysics* **248,** 247–261.

Buforn E., M. Bezzeghoud, A. Udias and C. Pro, (2004). Seismic source in the Iberian-African plate boundary. *Pageoph*, **161**, 3, 623 – 646.

Cabral, J., Moniz, C., Batlló, J., Figueiredo, P., Carvalho, J., Matias, L., Teves-Costa, P., Dias, R. and Simão, N. (2012). The 1909 Benavente (Portugal) earthquake: search for the source. *Nat Hazards*. DOI 10.1007/s11069-011-0062-8.

Cabral J, Moniz C, Terrinha P, Matias L, Ribeiro P (2000). Analysis of seismic reflection profiles in the neotectonic characterization of the Lower Tagus Valley area. *In: XXVII Gen Ass Europ Seismol Com., Lisbon (Portugal)*, 10–15 September, SSC1-07-P, 72.

Cabral J, Ribeiro P, Figueiredo P, Pimentel N, and Martins A (2004) The Azambuja fault: an active structure located in an intraplate basin with significant seismicity (Lower Tagus Valley, Portugal). *J Seismol* **8**: 347–362.

Cabral J. (1993). Neotectónica de Portugal continental, *PhD. thesis, Universidade de Lisboa.*

Cabral, J. and Ribeiro, A., (1988). Carta neotectónica de Portugal continental, escala 1:1,000,000. *Dept. de Geol., Fac. Ciências, Univ. de Lisboa, Serv. Geol. de Portugal, GPSN.*

Caldeira, B., Bezzeghoud, M. , Borges, J. F., Dorbath, C., Matias, L., Rocha, J. P., Madureira, G., Araújo, A., Corela, C. and Carrilho, F., (2007). Seismic Tomography of the Algarve Crust: Previous studies, *Campaign and first data, actas do 5o Simpósio de Meteorologia e Geofísica da APMG*, 5-8 Fevereiro de 2007, Peninche-Portugal, 76-80.

Carrilho, F., (2005). Estudo da sismicidade da zona sudoeste de Portugal continental, *Tese de Mestrado, Faculdade de Ciências da Universidade de Lisboa*, 160 p.

Carrilho, F., Teves-Costa, P., Morais, I., Pagarete, J. and Dias, R., (2004). Geoalgar Project – first results on seismicity and fault-plane solutions. *Pure and Applied Geophys.*, **161**, 3, 589-606.

Choffat P, and Bensaude A (1912). Estudos sobre o sismo do Ribatejo de 23 de Abril de 1909. *Com Serv Geol Port, Lisbon*, p 146.

Choi, Y., Stewart, J.P, and Graves R.W. (2005). Empirical Model for Basin Effects Accounts for Basin Depth and Source Location. *Bull. seism. Soc. Am.*, Vol. **95**, No. 4, pp. 1412–1427, August 2005, doi: 10.1785/0120040208.

Console, R. (2001). Testing earthquake forecast hypotheses, *Tectonophysics*, **338**, 261-268.
Coppersmith, K. J., and R. R. Youngs (1986). Capturing uncertainty in probabilistic seismic hazard assessments within intraplate tectonic environments, *in Proceedings of the Third U.S. National Conference on Earthquake Engineering*, Vol. **1**, 301–312.

Cornell, C.A. (1968). Engineering seismic risk analysis. *Bull. seism. Soc. Am.*, **58**(1): 1583-1606.

Dominique, P. (1999). Evaluation de l'aléa sismique: état de l'art. *Rapport BRGM R 39010*

Douglas, J. (2004a). Ground motion estimation equations 1964–2003: Reissue of ESEE Report No. 01-1: 'A comprehensive worldwide summary of strong-motion attenuation relationships for peak ground acceleration and spectral ordinates (1969 to 2000)' with corrections and additions. *Tech. rept. 04-001-SM. Department of Civil and Environmental Engineering; Imperial College of Science, Technology and Medicine*; London; U.K.

Douglas, J. (2006). Errata of and additions to 'Ground motion estimation equations 1964– 2003'. *Intermediary report RP-54603-FR. BRGM*, Orléans, France.

Douglas, J. (2008). Further errata of and additions to 'Ground motion estimation equations 1964–2003'. *Final report RP-56187-FR. BRGM*, Orléans, France.

Dineva, S., J. Batllo, D. Mihaylov, and T. Van Eck (2002). Source parameters of four strong earthquakes in Bulgaria and Portugal at the beginning of the 20th century, *J. Seism*. **6,** 99–123.

Duarte, J.C, Rosas, F.M, Terrinha, P, Schellart, P.W., Boutelier, D., Gutscher, M.-A. and Ribeiro A (2013).Are subduction zones invading the Atlantic? Evidence from the southwest Iberia margin. *Geology published* online 6 June 2013; doi: 10.1130/G34100.1.

Ellsworth, W., and Survey, G. (2008) A Physically Based Earthquake Recurrence Model for Estimation of Long-term Earthquake Probabilities. (*US Dept. of the Interior, US Geological Survey, 1999*).

EPRI (1986). Seismic hazard methodology for the central and eastern United States, *EPRI report NP-4726*, *Electric Power Research Institute*, Palo Alto.

Esmer, O. (2006). Information theoric framework for the earthquake recurrence models: Methodica Firma Per Terra Non-Firma.

Field, E. H., T. E. Dawson, K. R. Felzer, A. D. Frankel, V. Gupta, T. H. Jordan, T. Parsons, M. D. Petersen, R. S. Stein, R. J. Weldon II and C. J. Wills (2009). Uniform California Earthquake Rupture Forecast, Version 2 (UCERF 2), *Bull. seism. Soc. Am.*, **99**, 2053-2107, doi:10.1785/0120080049.

Fitzenz D.D., Ferry M.A. and Jalabeanu A. (2010). Long-term slip history discriminates among occurrence models for seismic hazard assessment, *Geophys. Res. Lett.*, 37, L20307, doi: 10.1029/2010GL044071.

Fitzenz, D. D., A. Jalobeanu, and S. H. Hickman, (2007). Integrating laboratory creep compaction data with numerical fault models: A Bayesian framework, *J. Geophys. Res.*, **112** B08410, doi:10.1029/2006JB004792 .

Fonseca, J. and Long, R., (1991). Seismotectonics of Ibéria: a distributed Plate Margin, Seismotectonic and seismic risk of the Ibério. Magrebian Region. *Publ. IGN*, Madrid, 8.

Grandin, R., Borges, J. F., Bezzeghoud, M., Caldeira, B. and Carrilho, F., (2007a). Simulations of strong ground motion in SW Iberia for the 1969 February 28 (MS = 8.0) and the 1755 November 1 (M ~ 8.5) earthquakes– I. Velocity model. *Geophys. J. Int.*, **171**, 3, 1144-1161.

Grandin, R., Borges, J. F., Bezzeghoud, M., Caldeira, B. e Carrilho, F., (2007b). Simulations of strong ground motion in SW Iberia for the 1969 February 28 (MS = 8.0) and the 1755 November 1 (M ~ 8.5) earthquakes – II. Strong ground motion simulations, *Geophys. J. Int.*, **171**, 2, 807-822.

Gutenberg B., Richter C. (1944) - Frequency of earthquakes in California. *Bull. seism. Soc. Am.*, **34**.

Gutscher, M.A., Malod, J., Renault, J.P., Contrucci, I., Klingelhoefer, F., Mendes- Victor, L., and Spakman, W., (2002). Evidence for Active Subduction Beneath Gibraltar, *Geology*, **30**, no.12, 1071-1074.

Helmstetter, A., Kagan, Y. Y., and Jackson D. D. (2007). High-resolution time-independent grid-based forecast for M ≥ 5 earthquakes in California, *Seismol. Res. Lett.* **78**, no. 1, 78–86, doi 10.1785/ gssrl.78.1.78.

Johnston, A., (1996). Seismic moment assessment of earthquakes in stable continental regions – III. New Madrid 1811-1812, Charleston 1886 and Lisbon 1755, *Geophys. J. Int.* **126**, 314-344.

Kagan, Y. Y., and D. D. Jackson, (1996). Statistical tests of VAN earthquake predictions: Comments and reflections, *Geophysical Research Letters*, **23**(11), 1433-1436.

Kárník V (1969). Seismicity of the European area, part 1. Reidel, Dordrecht.

Kijko A., Sellevoll M. A . (1992) - Estimation o f earthquake hazard parameters from incomplete data files-Part II:Incorporation of magnitude heterogeneity. *Bull. seism. Soc. Am.,* **vol. 82**, n° 1.

Klügel J-U (2008). Seismic Hazard Analysis - Quo vadis?, *Earth-Science Reviews*, **88** 1-32, doi: 10.1016/j.earscirev.2008.01.003.

Kuehn N.M., Hainzl S. and Scherbaum F. (2008), Non-Poissonian earthquake occurrence in coupled stress release models and its effect on seismic hazard, *Geophys. J. Int.* , **174** 649-658, doi:10.1111/j.1365-246X.2008.03835.x.

Kuehn, N.M., Riggelsen C. and Scherbaum, F. (2011). Modeling the Joint Probability of Earthquake, Site, and Ground-Motion Parameters Using Bayesian Networks, *Bull. seism. Soc. Am.*, **101**(1), 235-249; DOI: 10.1785/0120100080.

Kulkarni, R.B., Youngs, R.R. and Coppersmith, K.J. (1984). "Assessment of Confidence Intervals for Results of Seismic Hazard Analysis", *Proceedings of the Eighth World Conference on Earthquake Engineering*, San Francisco, U.S.A., **Vol. 1**, pp. 263–270.

Le Goff B., Bertil D., Lemoine A . and Terrier M. (2009). Systemes de failles de Serenne et de la Haute-Durance (Hautes-Alpes) : évaluation de l aléa sismique. *Rapport BRGM RP-57659-FR.*

Le Goff B., Fitzenz D., and Beauval C., 2010, Towards a bayesian seismotectonic zoning for use in Probabilistic Seismic Hazard Assessment (PSHA), *AIP Conf. Proc.* 1305, pp. 242-249; doi:http://dx.doi.org/10.1063/1.3573623.

Lonergan, L., and White, N., (1997), The Origin of the Betic Rif Mountain Chains, *Tectonics*, **16**, 504-522.

López Casado, C., J. Delgado, J. A. Peláez, M. A. Peinado, and J. Chacón (1992). Site effects during Andalusian earthquake (12/25/1884), *Proc. 10th World Conference on Earthquake* Engineering*.*, ***Vol. 2***, Madrid, A. A. Balkema, Rotterdam, 1085–1089.

López Casado, C., S. Molina Palacios, J. Delgado, and J. Peláez (2000). Attenuation of intensity with epicentral distance in the Iberian Peninsula, *Bull. seism. Soc. Am.* **90**, 34–47.

Luen, B. and Stark, P.B. (2008). *IMS Collections Probability and Statistics*: Essays in Honor of David A. Freedman Vol. 2 (2008) 302–315 2008 DOI: 10.1214/193940307000000509.

Matthews, M., Ellsworth, W., and Reasenberg, P. (2002).A Brownian model for recurrent earthquakes. *Bull. seism. Soc. Am.* 92(6):2233-2250, doi: rm10.1785/0120010267.

Martín, A. J. (1984). Riesgo Sísmico en la Península Ibérica, PhD thesis*, Talleres del Instituto Geográfico Nacional,* Vol. I and II (in Spanish).

Mezcua, J. and Rueda, J., (1997). Seismological evidence for delamination process in the lithosphere under the Alboran Sea. *Geophys. J. Int.*, 1-8.

Mezcua J (1982) Catalogo general de isosistas de la Península Ibérica. *IGN, Publ 202*, Madrid. http://www.fomento.es/NR/rdonlyres/9CA55404-0CAC-43DC-A9E3 E6366CE5EE42/38054/CatalogoGeneralIsosistas.pdf.

McGuire, R.K. (1976). Fortran computer program for seismic risk analysis, *U.S. Geological Survey Open-File Report 76-67.*

Moreira V. S. (1985), Seismotectonics of Portugal and its adjacent area in the Atlantic, *Tectonophysics* **11,** 85-96.

Moreira V. S., (1991). Historical Seismicity and seismotectonics of the area situated between the Iberian Penin- sula, Marrocco, Selvagens and Azores Islands. In: Seismicity, Seismotectonic and Seismic Risk of the Ibero-Magrebian Region, *Pub. I.G.N.*, Madrid, **8**, 213-225.

Mosca I., Console R., and D'Addezio G. (2012). Renewal models of seismic recurrence applied to paleoseismological and historical observations. *Tectonophysics*. doi: 10.1016/j.tecto.2012.06.028.

Musson R.M.W, (2004). Objective validation of seismic hazard source models, *13th world conference on earthquake engineering*, Vancouver, B.C, Canada,, Paper No.2492.

Muñoz, D. (1974). Curvas medias de variación de la intensidad sísmica con la distancia epicentral, *Tesis Licenc. Fac. Cien. Físicas, Univ. Complutense*, Madrid, (in Spanish).

Nocquet, J.M. and Calais, E., (2004), Geodetic Measurements of Crustal Deformation in the Western Mediterranean and Europe, *Pure and Applied Geophysics*, 161.

Ordaz M., Aguilar A., Arboleda J. (2003) - Program for computing seismic hazard, CRISIS 2003 Ver.3.02. UNAM University.

Page, Morgan T., David Alderson, and John Doyle (2011). The Magnitude Distribution of Earthquakes near Southern California Faults, *J. Geophys. Res.* - Solid Earth. **116**, B12309. doi:10.1029/2010JB007933.

Paolucci, R., and Morstabilini, L. (2006). Non-dimensional site amplification functions for basin edge effects on seismic ground motion. *Third International Symposium on the Effects of Surface Geology on Seismic Motion Grenoble*, France, 30 August - 1 September 2006 Paper Number: 41.

Parsons T. and Geist E.L. (2009), Is there a basis for preferring characteristic earthquakes over a Gutenberg-Richter distribution in Probabilistic earthquake forecasting?, *Bull. seism. Soc. Am.*, **99**, 2012-2019, doi: 10.1785/0120080069.

Perreira, N., Carneiro, J.F., Araújo, A., Bezzeghoud, M. and Borges, J.F. (2013). Seismic and structural geology constraints to the selection of CO_2 storage sites – the case of the onshore Lusitanian basin, Portugal, *Journal of Applied Geophysics* (in press).

Pro C, Buforn E., Bezzeghoud M., Udias A., 2012. The earthquakes of 29 July 2003, 12 February 2007, and 17 December 2009 in the region of Cape Saint Vincent (SW Iberia) and their relation with the 1755 Lisbon earthquake. *Tectonophysics*, **583**, 16-27, http://dx.doi.org/10.1016/j.tecto.2012.10.010 .

QIS5: European Commission publishes instructions for fifth Quantitative Impact Study. http://www.munichre.com/touch/ publications/de/list/default .aspx?category=22.

Ribeiro, A. R., Cabral, J., Baptista, R. and Matias, L., (1996). Tectonic stress pattern in Portugal Mainland and the adjacent Atlantic Region, *Tectonics*, **15**, 641-659.

Rocha, J. P., Bezzeghoud, M., Caldeira, B., Borges, J., Dias, N., Matias, L. and Dorbath, C., (2009). A sismicidade Algarvia para o período de Janeiro - Junho 2006. *IV Encontro de Pós-graduação em Ciências Físicas e da Terra da Universidade de Évora*, Universidade de Évora, Évora (18-19 de Setembro de 2009), 17-18.

Roque, C., Terrinha, P., Lourenço, N., and Pinto de Abreu, M., (2009). Morphostructure of the Tore Seamount and evidences of recent tectonic activity (West Iberia Margin). *6o Simposio sobre el Margen Ibérico Atlántico* MIA09, 1-5 de deciembre de 2009, Oviedo, 33-36.

Senos, L. and Carrilho, F., (2003). Sismicidade de Portugal Continental. Física de la Tierra, Sismicidade de la Península Ibérica, Eds: E. Buforn y A. Udias, **vol. 15**, 93-110.

Senos L., Ramalhete D., and Taquelim M.J. (1994) Estudo dos principais sismos que atingiram o território de Portugal Continental. *Inst Meteo*, Lisbon, Mon 46.

Solvency II directive.
http://ec.europa.eu/internal_market/insurance/solvency/index_en.htm#november2009.
Sousa, M. L., and C. S. Oliveira (1997). Hazard mapping based on macro- seismic data considering the influence of geological conditions, *Nat. Hazards* **14**, 207–225.
Sousa, M. L., Martins, A. and Oliveira, C. S., (1992), Compilação de catálogos sísmicos da região Ibérica. Relatório 36/92, NDA, *Laboratório Nacional de Engenharia Civil*, Lisboa.

Stepp, J., I. Wong, J. Whitney, R. Quittemeyer, N. Abrahamson, G. Toro, R. Youngs, K. Coppersmith, J. Savy, and T. Sullivan (2001). Probabilistic seismic hazard analyses for ground motions and fault displacements at Yucca Mountain, Nevada, *Earthq. Spectra* **17**, 113–151.

Stich, D., J. Batllo, R. Macia, P. Teves-Costa, and J. Morales (2005). Moment tensor inversion with single-component historical seismograms: The 1909 Benavente (Portugal) and Lambesc (France) earthquakes, *Geophys. J. Int.* **162**, 850–858.

Stich, D., Ammon, C. J. and Morales, J., (2003). Moment tensor solutions for small and moderate ear- thquakes in the Ibero-Maghreb region. *J. Geophys. Res.* 108, 2148.

Terrinha, P., Pinheiro, L. M., Henriet, J.-P., Matias, L., Ivanov, M. K., Monteiro, J. H., Akhmet-zhanov, A., Volkonskaya, A., Cunha, T., Shaskin, P. and Rovere, M., (2003), Tsunamigenic-seis-mogenic structures, neotectonics, sedimentary processes and slope instability on the southwest Portuguese Margin, *Mar. Geol.* **195**, 55-73.

Terrinha, P. A. G., (1998). Structural geology and tectonic evolution of the Algarve basin, South Portugal. *PhD thesis, Royal School of Mines, Imperial College*. London, 423 p.

Teves-Costa, P., and Batlló, J. (2010). The 23 April 1909 Benavente earthquake (Portugal): macroseismic field revison, *J. Seismol*, doi 10.1007/s10950-010-9207-6.

Teves-Costa P, Batlló J, Rio I, and Macià R (2005) O sismo de Benavente de 23 de Abril de 1909—Estado da arte. *In: Proc. 4◦ Simpósio de Meteorologia e Geofísica da APMG, Sesimbra*, 14–17 Fev, p 44–49.

Teves-Costa P., Borges J.F., Rio I, Ribeiro R., and Marreiros C. (1999) Source parameters of old earthquakes: semi-automatic digitization of analog records and seismic moment assessment. *Nat Hazards* **19**:205–220.

Toro, G. R., Abrahamson N. A., and Schneider J. F. (1997). Model of strong ground motion from earthquakes in central and eastern North America: best estimates and uncertainties, *Seismological Research Letters* **68,** no. 1, 41– 57.

Working Group on California Earthquake Probabilities (WGCEP), (2012). Uniform California Earthquake Rupture Forecast version 3 (UCERF3) Framework. *Technical report #8.*

Vilanova, S. P., and Fonseca, J. F. B. D. (2007). Probabilistic Seismic-Hazard Assessment for Portugal, *Bull. Seism. Soc. Am.*, **97**, 1702-1717.

Waldhauser, F., and Ellsworth W. L. (2000). A double-difference earthquake location algorithm: Method and application to the northern Hayward , California, *Bull. Seism. Soc. Am.*, **90**, 1353–1368.

Weatherill, G. and Burton, P.W. (2009). Delineation of shallow seismic source zones using K-means cluster analysis, with application to the Aegean region. *Geophys. J. Int.*, **176** 565-588.v .

Weichert D.H. (1980) - Estimation of the earthquake recurrence parameters for unequal observational periods for different magnitudes. *Bull. Seism. Soc. Am.*, **70**, p. 1337-1346.

Wells, D.L. and Coppersmith, K.J., (1994). New empirical relationships among magnitude, rupture length, rupture width, rupture area, and surface displacement. *Bull. Seism. Soc.Am.*, **84**: 974-1002.

Wesson, R. L., Bakun, W. H., and Perkins, D. M. (2003). Association of Earthquakes and Faults in the San Francisco Bay Area Using Bayesian Inference. *Bull. Seism. Soc. Am.* **93(3)** 1306-1332. doi: 10.1785/01200200855.

Woo, G. (1996). Kernal estimation methods for seismic Hazard area source modelling. *Bull. Seism. Soc. Am.*, **86** 353-362.

Zitellini, N., Chierici, F., Sartori, R. and Torelli, I., (1999). The tectonic source of the 1755 Lisbon earthquake and tsunami, *Annali di Geofisica*, **42**, 1, 49-55.

Zitellini, N., Mendes, L. A., Cordoba, D., Danobeitia, J., Nicolich, R., Pellis, G., Ribeiro, A., Sartori, R., Torelli, L., Bartolomé, R., Bortoluzzi, G., Calafato, A., Carrilho, F., Casoni, L., Chierici, F., Corela, C., Correggiari, A., Della Vedova, B., Gràcia, E., Jornet, P., Landuzzi, M., Ligi, M., Magagnoli, A., Marozzi, G., Matias, L., Penitenti, D., Rodri- guez, P., Rovere, M., Terrinha, P., Vigliotti, L. and Zahinos Ruiz, A., (2001). Source of 1755 Lisbon Earthquake and Tsunami Investigated. Eos Trans. *AGU*, 82, (26), **285**, 290-291.

Zöller G. , Ben-Zion Y., Holschneider M., Hainzl S. (2007). Estimating recurrence times and seismic hazard of large earthquakes on an individual fault, *Geophys. J. Int.*, **170**, 1300-1310, doi: 10.1111/j.1365-246X.2007.03480.x.